High-K Isomers in ^{180}Os

A thesis submitted to the University of Manchester for the degree of
Doctor of Philosophy
in the Faculty of Engineering and Physical Sciences

2010

Nicola M. Lumley

School of Physics and Astronomy

Contents

List of Figures

List of Tables

Abstract

The high-spin states of ^{180}Os were populated in the ^{150}Nd(^{36}S,6n) fusion-evaporation reaction at Argonne National Laboratory. The 177 MeV ^{36}S beam was supplied by the ATLAS tandem and linear accelerators and the subsequent γ-ray transitions were detected in the Gammasphere array. The ^{150}Nd target was backed with 8 mg/cm^2 of ^{197}Au to stop the recoils in the centre of the Gammasphere array allowing prompt-delayed coincidence analysis across isomeric states.

This work was carried out to investigate the competition between rotational and vibrational excitations at high-spin in the mass A $\approx$ 180 region of the nuclear chart where high-K isomers are prevalent. It is proposed that there is a small pocket of nuclei for which γ vibrations compete with rotations as the favoured mode of excitation above high-K intrinsic states.

Two high-K isomeric states were established in ^{180}Os with ($K^\pi = 22^+$) and $K > 24$ with half lives of 0.8 $\pm$ 0.4 μs and 72 $\pm$ 6 ns, respectively. Prompt-delayed coincidence analysis was used to identify prompt level-schemes for these isomers and levels have been extracted up to spins of $I > 30\ \hbar$. Five bands were identified above the ($K^\pi = 22^+$) isomer and two additional bands were established above the $K > 24$ isomer. The possible multi-quasiparticle configurations for the isomers and intrinsic states are considered in terms of g-factors, excitation energies and BCS calculations. The rotational and vibrational characteristics for the prompt structures are discussed in terms of the aligned angular momentum, i_x, and SCTAC calculations. The lifetime for the decay of the ($K^\pi = 22^+$) isomer is discussed in terms of the reduced hindrance, f_v, and the validity of the K quantum number.

Declaration

No portion of the work referred to in this thesis has been submitted in support of an application for another degree or qualification of this or any other university or institute of learning.

Copyright Statement

(i) The author of this thesis (including any appendices and/or schedules to this thesis) owns certain copyright or related rights in it (the "Copyright") and s/he has given The University of Manchester certain rights to use such Copyright, including for administrative purposes.

(ii) Copies of this thesis, either in full or in extracts and whether in hard or electronic copy, may be made only in accordance with the Copyright, Designs and Patents Act 1988 (as amended) and regulations issued under it or, where appropriate, in accordance with licensing agreements which the University has from time to time. This page must form part of any such copies made.

(iii) The ownership of certain Copyright, patents, designs, trade marks and other intellectual property (the "Intellectual Property") and any reproductions of copyright works in the thesis, for example graphs and tables (Reproductions), which may be described in this thesis, may not be owned by the author and may be owned by third parties. Such Intellectual Property and Reproductions cannot and must not be made available for use without the prior written permission of the owner(s) of the relevant Intellectual Property and/or Reproductions.

(iv) Further information on the conditions under which disclosure, publication and commercialisation of this thesis, the Copyright and any Intellectual Property and/or Reproductions described in it may take place is available in the University IP Policy (see http://www.campus.manchester.ac.uk/medialibrary/policies/intellectual- property.pdf), in

Acknowledgments

I would to start by thanking my supervisor Dr. Dave Cullen for all of his advice and encouragement throughout my Ph.D. and for giving me the opportunity to work in such an interesting area of research. This thesis would not have been possible without the dedication and ingenuity of the incredible team of physicists at Argonne National Laboratory and the collaboration of Prof. Phil Walker, Ian Cullen, Shezad Khan, Pete Mason, Shaofei Zhu, Mike Carpenter and Robert Janssons who made the experiment a success. I also would like to thank Prof. Phil Walker again for the BCS calculations and Dr. John Smith for the TRS and CSM calculations. I also gratefully acknowledge EPSRC for the financial support of my PhD.

I also owe a huge thank you to Pete Mason, Alick Deacon, Ben Kay and Mark Procter for their tireless proof reading and advice on writing this thesis. I must also single out Pete Mason again for all his guidance throughout my PhD, even after he left the group. I also have to thank my Uncle Chris for his keen eye for typos!

I would like to thank the entire Nuclear Physics Group, past and present, for making my PhD such an enjoyable experience. I want to individually mention Prof. Sean Freeman for all his advice and friendship, Joseph Dare for "The Ring of Words", Alan Howard, Pete Mason, AJ "Birthday Suit Up" Mitchell and Dave Steppenbeck for the countless trips to the pub and Mark "Awesome" Procter, David Sharp and Jeffry Thomas for our shared appreciation of crosswords and Jabez. I also want to thank Ben Kay for Chicago, chicken wings and everything else.

Finally, I would not have been able to complete this thesis without the unwavering support of my parents. I could not have finished this thesis without their advice and encouragement. I really can not thank them enough.

Nicola Lumley
May 2010

Chapter 1

Introduction

In this thesis the spectroscopic study of the high-spin states of ^{180}Os will be presented. In the mass $A \approx 180$ region of the nuclear chart, prolate deformations and collective rotations dominate the nuclear structure. However, it is proposed that ^{180}Os lies in a small pocket of nuclei where multiphonon vibrations compete with rotations as the favoured mode of excitation above high-K isomers which are also prevalent in this region. This thesis aims to investigate the high-K isomers in ^{180}Os and the nuclear structure based upon them.

For prolate nuclei in the mass $A \approx 180$ region, many of the individual nucleon orbitals close to the Fermi surface have large projections of angular momentum on to the symmetry axis, Ω. The resulting multi-quasiparticle configurations can therefore have large total projections of angular momentum on to the symmetry axis, K. The decays from these configurations require a large change in the K quantum number leading to an abundance of high-K isomers in the region. The Bohr-Mottelson collective model [1] shows that the addition of angular momentum by rotation requires more energy in

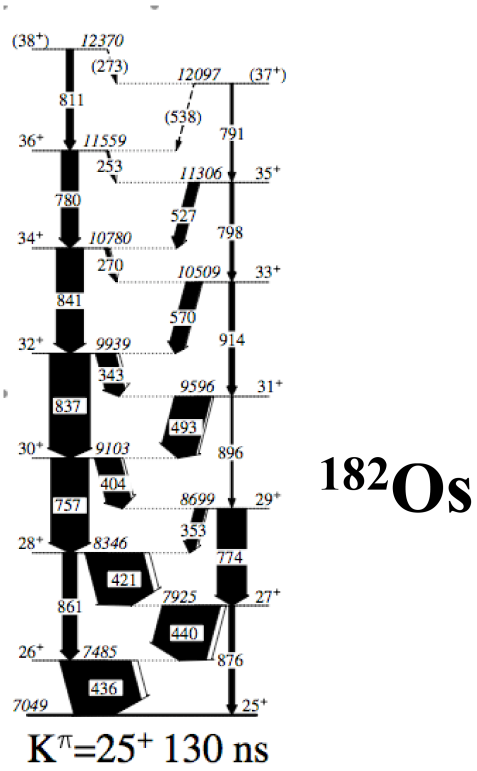

Figure 1.1: A partial level scheme for ^{182}Os showing the transitions above the $K^{\pi}= 25^{+}$ isomeric state.

the presence of a high-K vector. Although the structure above K isomers in the mass $A \approx 180$ region tends to be predicted by the rotational model of the collective nucleus, there has been evidence to suggest that rotation becomes hindered to the point that multiphonon vibrations are observed above high-K isomers in certain nuclei.

A study of ^{182}Os provided the first evidence of multiphonon vibrations competing with rotation as the favoured mode of excitation at high spin [2, 3]. Figure 1.1 shows the band structure above the $K^{\pi}= 25^{+}$, 7049-keV isomeric state with a half-life of 130 ns, which provided this evidence. The irregular sequence and small range of γ-ray energies and the stronger intensity of the even-spin band support high-spin excitation driven by nuclear vibrations.

Similar irregular sequences, which could not be predicted by a rotational model alone, were observed above the $K^{\pi}= 37/2^{+}$ isomeric state in ^{181}Os [4] and above the $K^{\pi}= 43/2^{+}$ isomeric state in ^{183}Os [5] providing further evidence of competing vibrational modes at high spins in this region. ^{180}Os is an ideal candidate to investigate this further since the excitation energy in its γ band is lower than that of ^{182}Os implying that ^{180}Os is more susceptible to γ vibrations.

The high-spin states of ^{180}Os were populated in a heavy-ion fusion evaporation reaction using a beam produced by the ATLAS accelerator at Argonne National Laboratory (ANL). The γ-ray transitions were detected by the Gammasphere array and prompt-delayed coincidence analysis was performed to identify isomeric states and the structure based upon them. The work presented in this thesis will provide a complete spectroscopic analysis of ^{180}Os with a particular focus on two high-K isomeric states with excitation energies of 5848 keV and 7592 keV with $K^{\pi}=22^{+}$ and $K \geq 24$, respectively. The half-lives of the isomeric states were measured and are discussed in terms of K forbideness. Possible multi-quasiparticle configurations for these isomeric states are also discussed. The structure identified above the two high-K isomeric states is presented and is discussed in terms of the underlying mode of excitation.

Chapter 2

Nuclear structure and γ decay

In the mid-shell region of the nuclear chart nuclear deformations are prevalent and collective excitations dominate the nuclear structure. The collective model of nuclear excitations was first proposed by J. Rainwater to include all nucleons as opposed to the valence nucleons alone [6]. This chapter will introduce the Nilsson model and the collective rotational and vibrational models for deformed nuclei. The calculations used to predict the properties of rotating deformed nuclei and the excitation energy of multi-quasiparticle configurations will also be presented. Finally, the probability of γ decays between nuclear states will be discussed.

2.1 Nuclear states in deformed nuclei

2.1.1 Nuclear deformation

The radius of a deformed nucleus, R, as a function of the spherical coordinates θ and ϕ is given by

$$R(\theta,\phi) = R_0 \left[1 + \sum_{\lambda=2}^{\infty} \sum_{\mu=-\lambda}^{\lambda} \alpha_{\lambda\mu} Y_{\lambda\mu}(\theta,\phi) \right], \tag{2.1}$$

where R_0 is the radius of a spherical nucleus with the same volume, $\alpha_{\lambda\mu}$ are deformation parameters and $Y_{\lambda\mu}(\theta,\phi)$ are the spherical harmonics. The parameter λ defines the mode of deformation, with λ=0 and λ=1 referring to the monopole and dipole deformations, respectively. The former simply describes a spherical shape and the latter a displacement of the center of mass of the nucleus which is generally neglected at low energies. The expansion converges rapidly for $\lambda \geq$3 making quadruple deformations the predominantly observed form of deformation. Although deformations do exist with λ=3 (octupole) and λ=4 (hexadecapole), their contribution is generally minimal.

The expansion coefficients for quadrupole deformations are generally expressed as

$$\alpha_{20} = \beta_2 \cos\gamma \quad \text{and} \quad \alpha_{22} = \alpha_{2-2} = \frac{1}{\sqrt{2}} \beta_2 \sin\gamma, \tag{2.2}$$

where β_2 is the magnitude of the quadrupole deformation and γ is the deviation from axial symmetry. The nuclear axes are chosen such that α_{21}=0. The Lund convention utilises the parameters β_2 and γ to give a graphical interpretation of the differing shapes of the quadrupole deformed nucleus, shown in Fig. 2.1. In this polar plot β_2 is depicted by the radial distance and γ as the polar angle. Axially-symmetric nuclei at γ=0° and γ=-120°

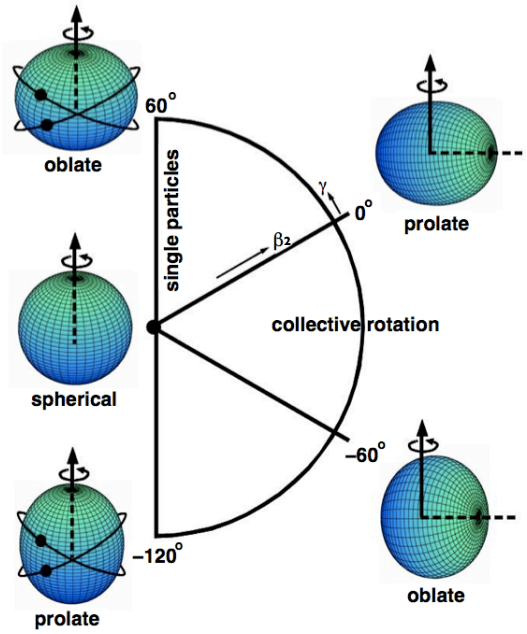

Figure 2.1: [Colour] The Lund convention showing the deformation parameters β_2 and γ for oblate and prolate deformations [7].

are known as *prolate* nuclei and the semi-major axis lies along the symmetry axis. Nuclei at γ=60° and γ=-60° are known as *oblate* nuclei for which the semi-major axis and symmetry axis are perpendicular. Non-axially symmetric (*triaxial*) nuclei have values of γ between those for prolate and oblate nuclei. For axially symmetric nuclei it is conventional to assign $\beta_2 > 0$ for prolate deformations and $\beta_2 < 0$ for oblate deformations.

Experimentally observed properties of nuclei can be described by time dependent deformations R(θ,ϕ,t) and $\alpha_{\lambda\mu}(t)$. The parameter λ now describes the mode of excitation, with λ= 0, 1, 2 and 3 referring to monopole, dipole, quadrupole and octopole excitations, respectively. The collective vibration and rotation of nuclei are discussed in Sections 2.1.3 and 2.1.4, respectively.

2.1.2 Nilsson model

The Nilsson model was developed to describe the single-particle orbits of all the nucleons in an axially-symmetric nucleus, within a deformed potential. Using a deformed harmonic-oscillator potential the Nilsson hamiltonian is given by

$$\hat{H}_{Nil} = -\frac{\hbar}{2m}\boldsymbol{\nabla}^2 + \frac{m}{2}\left(\omega_x^2 x^2 + \omega_y^2 y^2 + \omega_z^2 z^2\right) + C\,\boldsymbol{l}\cdot\boldsymbol{s} - D\,l^2. \tag{2.3}$$

The $\boldsymbol{l}\cdot\boldsymbol{s}$ term represents the coupling of the orbital and intrinsic angular momenta, $\boldsymbol{l}$ and $\boldsymbol{s}$, respectively. The term l^2 lifts the l degeneracy of the harmonic potential to emulate the more accurate Woods-Saxon potential by flattening the potential well at the center of the nucleus. The constants C and D are fitted empirically for each mass area of the nuclear chart. The one-dimensional oscillator frequencies, $\omega_{x,y,z}$ are related to the deformation parameter, ε by

$$\omega_x^2 = \omega_y^2 = \omega_0^2\left(1 + \frac{2}{3}\varepsilon\right) \quad \text{and} \quad \omega_z^2 = \omega_0^2\left(1 + \frac{4}{3}\varepsilon\right), \tag{2.4}$$

where ω_0 is the oscillator frequency in a spherical potential and is determined empirically. The deformation parameters ε and β_2 (see section 2.1.1) are related by

$$\beta_2 = \left(\frac{4\pi}{5}\right)^{\frac{1}{2}}\varepsilon. \tag{2.5}$$

The orbitals resulting from the Nilsson Hamiltonian are described by the asymptotic quantum numbers $\Omega[Nn_z\Lambda]$, where Λ and n_z are the projections of the orbital angular momentum, **l**, and the principle quantum number, N onto the symmetry axis, respectively. Ω is the projection of the total angular momentum **j** onto symmetry axis. The Nilsson quantum numbers

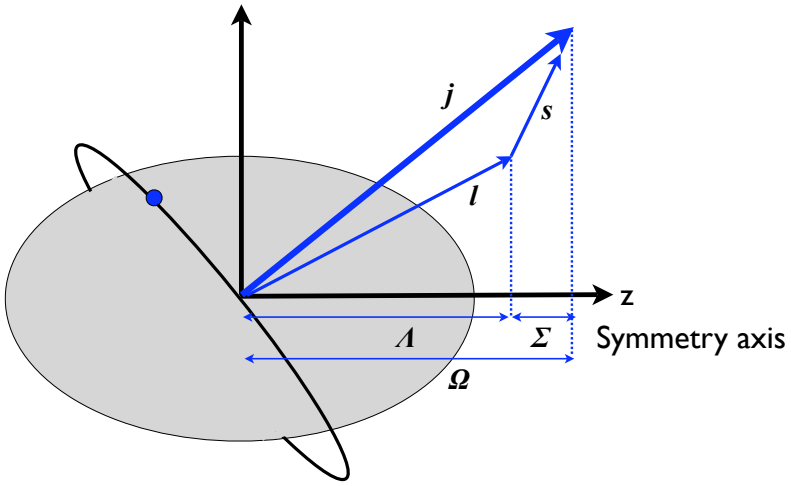

Figure 2.2: [Colour] A systematic diagram of the Nilsson quantum numbers Ω and Λ for a single-particle orbiting an axially-symmetric deformed core.

are illustrated in Fig. 2.2 which shows a single valence nucleon orbiting an axially-symmetric deformed core.

Nilsson diagrams are commonly used to illustrate the Nilsson orbitals, where the single particle energies are plotted against deformation. Figure 2.3 shows an example of a Nilsson diagram for neutrons in the range $82 \leq N \leq 126$. The Nilsson orbitals near the Fermi surface for ^{180}Os have been highlighted. The Nilsson diagram illustrates that the m_j substate degeneracy of each individual j orbital is lifted by deformation. The $i_{1/3}$ orbital for example, splits into 7 orbitals with Ω= 1/2, 3/2, 5/2, 7/2, 9/2, 11/2 and 13/2. For a prolate nucleus (β_2>0) the orbital with the lowest projection of angular momentum onto the symmetry axis is energetically favoured, *i.e* Ω=1/2, due to these orbitals having the largest overlap with the nuclear core. Similarly, for an oblate nucleus (β_2< 0) the orbitals with the largest projections of angular momentum onto the symmetry axis are favoured (Ω=13/2).

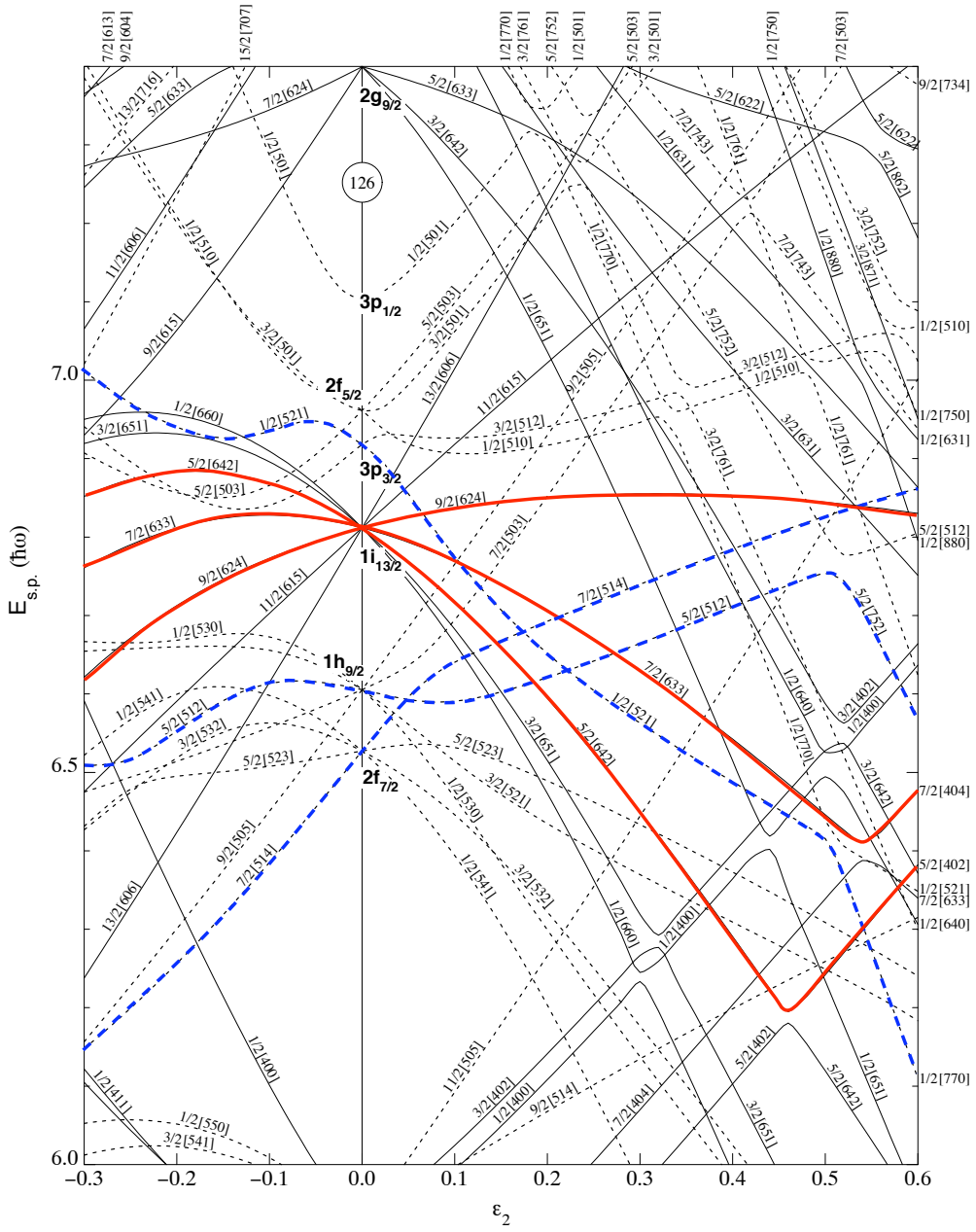

Figure 2.3: [Colour] A Nilsson diagram for $82 < N < 126$ neutons, showing single-particle energies, $E_{s.p}$ as a function of the deformation parameter, ϵ_2, where ϵ_2 is approximately $0.95\beta_2$. The orbials are labelled by the Nilsson quantum numbers, $\Omega[Nn_z\Lambda]$. Negative parity states are shown by dashed lines and positive parity states by solid lines. The $1i_{13/2}$ orbitals relevant to this thesis are highlighted in red and the negative parity orbitals relevant to this work are highlighted in blue.

The configuration of the nucleus is defined only by the unpaired nucleons. The ground state of an even-even nucleus will have all nucleons paired. This will result in zero angular momentum. For an odd-A nucleus the angular momentum of the ground state will be defined by which Nilsson orbital the unpaired nucleon is in. For an odd-odd nucleus with two unpaired nucleons, the ground-state configuration will be determined from the coupling of the unpaired nucleons. For excited states produced by the breaking of nucleon pairs, the configurations are based on the coupling of all the unpaired nucleons. The angular momentum of these multi-quasiparticle states is given by the sum of the individual nucleon angular momenta $\mathbf{J}=\sum_i \mathbf{j_i}$, and the total projection onto the symmetry axis is described by the quantum number K, where $K = \sum_i \Omega_i$.

2.1.3 Rotation

For deformed nuclei it is possible to generate excitation and angular momentum through rotations, unlike for spherical nuclei where rotation is not quantum mechanically valid. The rotational Hamiltonian is given by

$$\hat{H}_{rot} = \frac{\hbar^2}{2\Im}\mathbf{R^2}, \tag{2.6}$$

where $\Im$ is the moment of inertia of the nucleus and $\mathbf{R}$ is the angular momentum due to rotation, about an axis perpendicular to the symmetry axis. The total angular momentum of the nucleus, I will be due to the coupling of the rotational angular momentum and the intrinsic angular momentum, $\mathbf{J}$ of the valence nucleons, $\mathbf{I} = \mathbf{J} + \mathbf{R}$. The energy due to rotation is given by

$$E_{rot} = \frac{\hbar^2}{2\Im}[I(I+1) - K^2]. \tag{2.7}$$

Due to the axial symmetry of a nucleus the value for R is restricted to even-values, subsequently each rotational excitation results in the addition of two units of angular momentum, I. The energy states produced from a sequence of these rotations are known as rotational bands. The ratio of the energy of the 4^+ to the energy of the 2^+ for an even-even nucleus can be measured experimentally and compared to the predicted value, $E(4^+)/E(2^+) = 0.33$, to identify collective rotations.

Nuclear moment of inertia

If the nucleus is considered to be a rigid ellipsoid, in which all the nucleons are tightly bound and rotate collectively, the moment of inertia is given by

$$\Im_{rigid} = \frac{2}{5} M R_{av}^2 (1 + 0.31\beta_2), \tag{2.8}$$

where M is the mass of the nucleus and R_{av} is average radius of the ellipsoid. This model underestimates the moment of inertia when compared to empirical data. A model of a fluid nucleus where the nucleons are only weakly bound predicts a moment of inertia given by

$$\Im_{fluid} = \frac{9}{8\pi} M R_{av}^2 \beta_2. \tag{2.9}$$

This model is the other extreme to the rigid model and tends to underestimate the moment of inertia for a nucleus. It can be concluded that the structure of the nucleus is between that of tightly bound and fluid systems and is generally considered to be made of a rigid core surrounded by valence nucleons.

The moment of inertia for a nucleus containing unpaired nucleons will be larger than that for a nucleus built on a completely paired configuration.

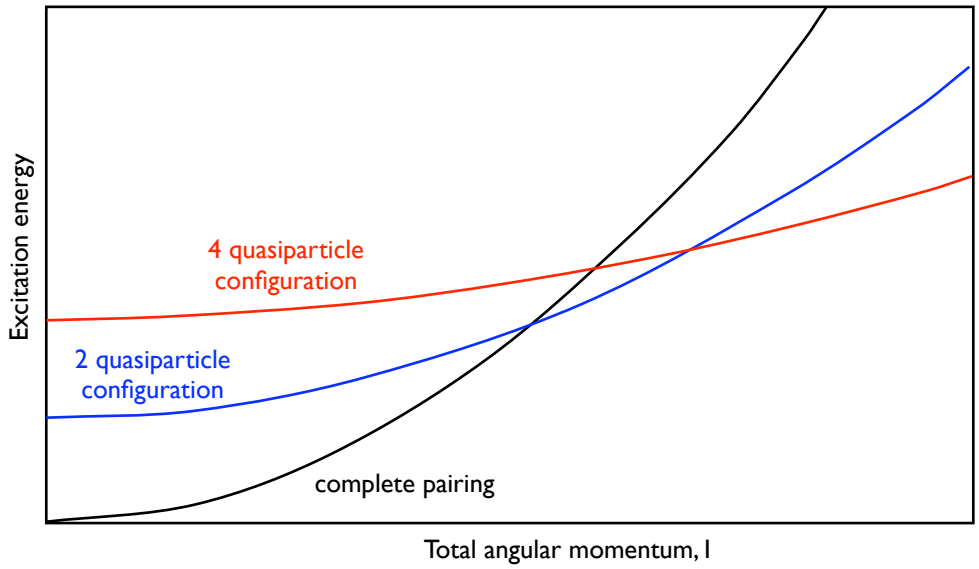

Figure 2.4: [Colour] A schematic plot showing the yrast configuration for a rotating nucleus. The excitation energies for a completely paired system (black), 2-quasiparticle system (blue) and 4-quasiparticle system (red) are shown.

Consequently, as the angular momentum increases due to rotation for both these configurations, the unpaired system becomes energetically favorable and *yrast* at high spin. This is illustrated in Fig. 2.4 where the excitation energies of completely paired, 2-quasiparticle and 4-quasiparticle configurations are shown. The excitation energy of the unpaired system is larger at low angular momentum, due to the energy required to break the pair. At higher angular momentum the larger value of $\Im$ for the 2-quasiparticle system results in a lower rotational energy than that for the paired state and is therefore yrast. It follows that the 4-quasiparticle configuration becomes yrast at even higher angular momentum.

Aligned angular momentum

The projection of the total angular momentum on to the rotation axis, I_x is given by

$$I_x = \sqrt{\left(I + \frac{1}{2}\right)^2 - K^2}. \tag{2.10}$$

For a nucleus with all its nucleons existing in time-reversed orbits the sum of the projection of angular momentum onto the rotation axis cancel to zero. Figure 2.5(a) illustrates a time reversed pair of nucleons. As the nucleus rotates the Coriolis force acts on the nucleons causing a gradual increase in the aligned angular momentum, known as centrifugal stretching. As the rotational frequency, $\hbar\omega$ increases, the Coriolis force increases and can become sufficiently large to overcome the attractive pairing interaction of the nucleus. At this rotational frequency the pair is broken and the nucleons realign their angular-momentum vectors in the same direction with respect to the rotation axis, shown in Fig. 2.5(b) This results in an increase in the angular momentum generated by the individual nucleon configuration. To conserve angular momentum for the system the rotational frequency of the nucleus must be reduced.

The effect of breaking a pair of nucleons is best observed in a plot of the aligned angular momentum (alignment) of the valence nucleons, i_x against rotational frequency. The alignment is calculated using

$$i_x(\omega) = I_x(\omega) - I_{ref}(\omega), \tag{2.11}$$

where I_{ref} is the aligned angular momentum of a reference rotor, given by

$$I_{ref} = (\Im_0 + \Im_1\omega^2)\omega. \tag{2.12}$$

The constants $\Im_0$ and $\Im_1$ are Harris parameters chosen to best represent the core of the nucleus [8]. When the pair is broken, the rotational frequency is

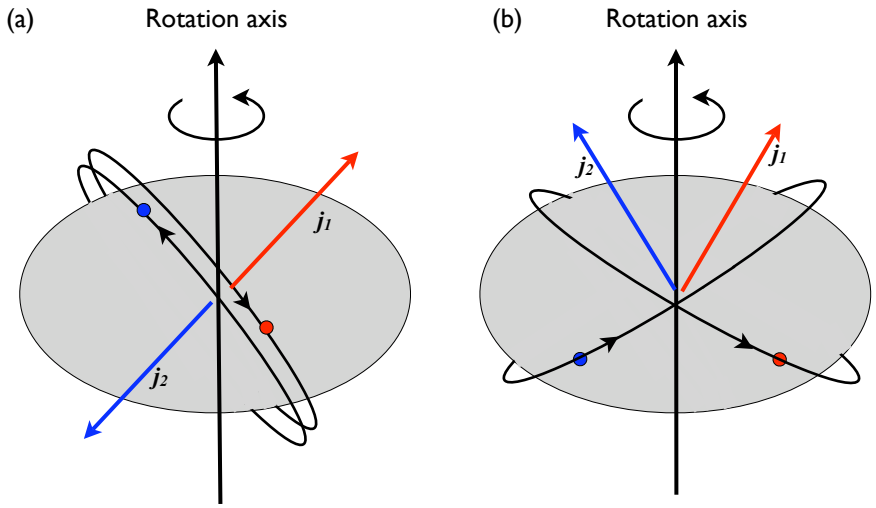

Figure 2.5: [Colour] The Coriolis effect on a rotating nucleus. (a) Paired nucleons where spins j_1 and j_2 are anti aligned and result in zero total projection of intrinsic angular momentum onto the rotation axis. (b) The unpaired nucleons align onto to the rotation axis to give a large total projection of intrinsic angular momentum onto the rotation axis.

reduced; however, the alignment will increase, which results in a *backbend* in the alignment plot. These backbends are also known as band crossings as the unpaired band crosses with a band built on a 2-quasiparticle configuration.

For odd nuclei, certain band crossings will be blocked if the interacting states are already occupied by a valence nucleon. Similarly in even-even nuclei where the rotational band is based on a quasiparticle configuration, the unpaired nucleons will block certain expected band crossings for that nucleus. Examining the rotational frequency at which band crossings are observed, or when they are blocked, provides information on the quasiparticles on which the bands are based.

2.1.4 Vibration

A nucleus can oscillate in numerous modes, the basis of which are described by the deformation in Equation 2.1. Dipole deformations (λ=1) are the displacement of the center of mass of the nucleus and cannot result from internal nuclear forces. Quadrupole vibrations (λ=2) add two units of angular momentum and even parity. There are two possible modes of quadrupole vibration defined by the direction in which they are aligned. β vibrations are aligned along the symmetry axis and cause fluctuations on the β deformation parameter, as described by the Lund convention.γ vibrations correspond to oscillations of the γ deformation parameter and cause the axial symmetry to be instantaneously broken. Octoplole vibtrations (λ=3) carry three units of angular momentum and negative parity.

Vibrations are quantised in units of phonons with the excitation energy for the n^{th} phonon of a vibration with frequency ω given by

$$E_n = \hbar\omega\big(n + \frac{N}{2}\big), \tag{2.13}$$

where N is the number of dimensions in the harmonic oscillator for the vibrational mode. For a quadrupole vibration there are three spatial dimensions and two possible vibrational modes (β and γ) giving $N = 5$.

2.2 Total-Routhian-Surface calculations

The total energy of a nucleus as a function of the deformation parameter, $\hat{\beta}$=(β_2, β_4, γ) is known as the total Routhian and is obtained by the Strutinsky method [9]. In this method the total Routhian is given by

$$E(N, Z, \hat{\beta}) = E_{LD}(N, Z, \hat{\beta}) + \delta E_{shell}(N, Z, \hat{\beta}) + \delta E_{pair}(N, Z, \hat{\beta}), \quad (2.14)$$

where E_{shell} and E_{pair} are the single-particle shell and pairing corrections to the energy of the nucleus calculated in the liquid drop model, E_{LD}, respectively [10].

The solutions for the total Routhians are plotted as potential energy surfaces, known as Total Routhian Surfaces (TRS), as a function of deformation. The axes used in the TRS plots are,

$$X = \beta_2 \cos(\gamma + 30^\circ) \quad (2.15)$$

and

$$Y = \beta_2 \sin(\gamma + 30^\circ), \quad (2.16)$$

as in the Lund convention. The minimum in these plots provide a theoretical prediction to the energetically favoured deformation of the nucleus. The contour of the plots are also used to predict any $softness$ in the deformation parameters.

2.3 CSM calculations

The effect of rotation on the single-particle orbitals is theoretically predicted using Cranked Shell Model (CSM) calculatitions [11, 12]. For a nucleus rotating at a frequency ω the single-particle cranking Hamiltonian is given by

$$\hat{H}' = \hat{H}_0 - \hbar\omega \hat{J}_x, \quad (2.17)$$

where $\hat{J}_x$ is the total angular momentum operator for the projection about the rotation axis and $\hat{H}_0$ is the Hamiltonian for a non rotating nucleus. The energy eigenvalues resulting from this Hamiltonian are the theoretical single-particle Routhians based on the Nilsson orbitals at $\omega = 0$. As the rotational frequency increases the Nilsson quantum numbers are no longer valid and the orbitals are described by signature, α, and parity, π. This only remains valid when rotation is about an axis perpendicular to the symmetry axis, known as a principle axis cranking (PAC).

To interpret the properties of rotational bands the experimental single-particle Routhians are compared to those predicted by the CSM calculations. The experimental single-particle Routhians, $e^{'}$ are calculated as the total nucleus Routhian, $E^{'}$, minus the contribution of the nuclear core,

$$e^{'} = E^{'} - E_{Ref}, \tag{2.18}$$

where the total Routhian is calculated using

$$E^{'} = \frac{1}{2}[E(I+1) + E(I-1)] - \omega(I)I_x(I). \tag{2.19}$$

The contribution of the nuclear core is given by the reference rotor,

$$E_{Ref} = \frac{\hbar^2}{8\Im_0} - \frac{\omega^2}{2}\Im_0 - \frac{\omega^4}{4}\Im_1, \tag{2.20}$$

where $\Im_0$ and $\Im_1$ are Harris parameters [8]. The backbends in the aligned angular momentum and the subsequent gain in aligned angular momentum, described in Section 2.1.3, are predicted by the theoretical Routhians through the relationship

$$i_x = -\frac{de^{'}}{d\omega}. \tag{2.21}$$

The comparison to the experimentally observed band crossings provides an insight into the underlying quasiparticle structure of the rotating nucleus.

2.3.1 SCTAC calculations

In the CSM only solutions to PAC are considered; however, rotation may also occur at an axis tilted with respect to a principle axis. Tilted Axis Cranking (TAC) must be considered in multi-quasiparticle systems where the total angular momentum may be orientated to both the symmetry and rotation axes [13]. Signature is no longer a valid quantum number in TAC and bands are described by their parity alone.

Shell Corrected Tilted Axis Cranking (SCTAC) calculations produce good results for nuclei with large deformations [14]. This method of calculation includes a shell modification based on the Strutinsky correction to the total Routhian [9] as given in Equation 2.14.

2.4 Blocked BCS calculations

The Bardeen-Cooper-Schrieffer (BCS) method was originally developed to describe the pairing interaction of electrons in superconductors [15]. This method has also been successful in describing the pairing of quasiparticles near the Fermi surface in nuclei [16]. The method is based on the Nilsson hamiltonian given in Equation 2.3, with protons and neutrons being considered separately and the residual spin interaction being added as a perturbation.

The excitation energy of a quasi particle in a state with energy ϵ_k is given by

$$E_k = \sqrt{(\epsilon_k - \epsilon)^2 + \Delta^2}, \tag{2.22}$$

where ϵ is the Fermi energy and Δ is the pairing energy, given by

$$\Delta = G \sum_{k>0} u_k v_k. \tag{2.23}$$

G is the monople pairing strength and is calculated for neutrons and protons to reproduce the lowest 2-quasineutron and 2-quasiproton states, respectively. The terms v_k and u_k are the probabilities that an orbital is occupied or unoccupied and are given by

$$v_k^2 = \frac{1}{2}\left(1 - \frac{\epsilon_k - \epsilon}{E_k}\right), \tag{2.24}$$

and

$$u_k^2 = \frac{1}{2}\left(1 + \frac{\epsilon_k - \epsilon}{E_k}\right). \tag{2.25}$$

Soloviev proposed that the presence of unpaired particles in the nucleus effected the superfluid properties of the system [17]. When a particle is in an orbital, k_j, pairs of particles can no longer scatter into it; this orbital is effectively blocked and as such is excluded form the calculations [18]. It follows that equation 2.23 becomes

$$\Delta = G \sum_{k \neq k_j} u_k v_k, \tag{2.26}$$

forming the basis of the Blocked BCS method.

The residual interaction is calculated based on the Gallagher-Moszkowki coupling rules described in Ref. [19]. The residuals for 2-quasiparticle interactions are derived from experimental data and the sum of all possible 2-quasiparticle configurations within a multi-quasiparticle state gives the total residual energy.

2.5 Transition rates

The probability of a γ-ray transition occurring between two states is governed by the difference in the wave functions of the initial and final states. The transition probability is calculated by Fermi's golden rule,

$$\lambda = \frac{2\pi}{\hbar}|V_{fi}^{'}|^2\rho(E_f), \tag{2.27}$$

where $\rho(E_f)$ is the density of final states. The nuclear matrix element, $V_{fi}^{'}$ defined as the overlap integral of the initial and final states, is given by

$$V_{fi}^{'} = \langle\Psi_f(r)|\hat{V}^{'}|\Psi_i(r)\rangle. \tag{2.28}$$

The operator $\hat{V}^{'}$ represents a perturbation to the nuclear potential and allows transitions to proceed between the initial and final states, $|\Psi_f(r)\rangle$ and $|\Psi_i(r)\rangle$, respectively.

Weisskopf estimates provide theoretical decay rates, based on the assumption that the transition is due to a single proton changing from one shell-model state to another [20]. The Weisskopf estimates for the four lowest multipole orders are defined in Table 2.1. Experimental decay rates are generally expressed in units of the Weisskopf estimates and large deviations from these single particle estimates are indicative of collective nuclear motion.

2.5.1 Isomeric states

The half-life of a state is related to the transition probability by

$$T_{1/2} = \frac{\ln 2}{\lambda}. \tag{2.29}$$

States which have substantially longer half-lives than the other excited states in a particular nucleus are known as isomers. The slower transition rate for

Multipolarity	Transition Rate
$E1$	$\lambda(\mathrm{E1}) = 1.0 \times 10^{14}\ A^{2/3}\ E^3$
$E2$	$\lambda(\mathrm{E2}) = 7.3 \times 10^{7}\ A^{4/3}\ E^5$
$E3$	$\lambda(\mathrm{E3}) = 34\ A^2\ E^7$
$E4$	$\lambda(\mathrm{E4}) = 1.1 \times 10^{-5}\ A^{8/3}\ E^9$
$M1$	$\lambda(\mathrm{M1}) = 5.6 \times 10^{13}\ E^3$
$M2$	$\lambda(\mathrm{M2}) = 3.5 \times 10^{7}\ A^{2/3}\ E^5$
$M3$	$\lambda(\mathrm{M3}) = 16\ A^{4/3}\ E^7$
$M4$	$\lambda(\mathrm{M4}) = 4.5 \times 10^{-6}\ A^2\ E^9$

Table 2.1: Weisskopf single-particle estimates of transition rates.

an isomeric state is attributed to significant differences between the initial state and the available final states. These differences can be of various forms such as the shape of the nuclear core and the spin of the nucleus, forming shape and spin-trap isomers, respectively. The focus of this report is K-trap isomers which occur when the difference in K between the initial and final states is greater than the multipolarity of the transition between them ($\lambda \geq \Delta K$) [21]. Löbner found that the transition rate is reduced by a factor of $\sim$100 per degree of K forbiddeness [22]. The degree of K forbiddeness is defined as $\nu = \Delta K - \lambda$, and the associated reduced hindrance given by

$$f_\nu = \left(\frac{T^\gamma_{1/2}}{T^W_{1/2}} \right)^{1/\nu}, \tag{2.30}$$

where $T^\gamma_{1/2}$ is the measured half-life and $T^W_{1/2}$ is the Weisskopf estimate.

Chapter 3

Experimental techniques

The selection of experimental conditions and techniques is fundamental to the success of an experiment. The experiment discussed in this work was designed to populate states of the nucleus of interest, ^{180}Os, with sufficient spin and energy to allow high-K isomers and the nuclear states based upon them to be identified. A high-resolution and high-fold γ-ray data set was also required to facilitate meaningful analysis.

The experiment was performed using the Argonne Tandem Linear Accelerator System (ATLAS) at Argonne National Laboratory (ANL) in Illinois, USA. The γ-ray transitions were detected in the Gammasphere spectrometer. This chapter discusses the details of the reaction, the experimental set up and the detector system.

3.1 Population of nuclei

3.1.1 Heavy-ion fusion-evaporation reactions

To access the mass region required in this experiment, heavy-ion fusion-evaporation reactions are the most effective way of populating high-spin states with large production cross-sections. Fusion-evaporation reactions occur when a beam of ions is accelerated onto a stationary target to produce energetically excited compound nuclei with large angular momenta. The compound nuclei in turn de-excite via the emission of a combination of particles and γ rays.

For a nuclear-fusion reaction to occur the projectile nuclei must collide with the target nuclei with sufficient energy to overcome the fusion barrier and come into the range of the nuclear force. The fusion barrier can be approximated to the Coulomb barrier, the energy required for the incident nuclei to overcome their mutual electrostatic repulsion. Figure 3.1 shows the effective potential resulting from the repulsive Coulomb potential and attractive Wood-Saxon potential for nucleons. In sufficiently heavy systems the combination of nuclear and Coulomb forces is still repulsive within the range of the nuclear force and additional energy is required for fusion to occur [23].

The nuclear-fusion reaction takes $\sim 10^{-22}$ s. This is sufficient time for the compound nucleus to lose any memory of the initial target and projectile nuclei. As stated by the Bohr assumption, the following decays will provide information about the nuclear structure of the compound nuclei which is independent of the initial nuclei [24]. Compound nuclei formed in heavy-ion fusion reactions tend to be neutron deficient as the N/Z ratio for stability

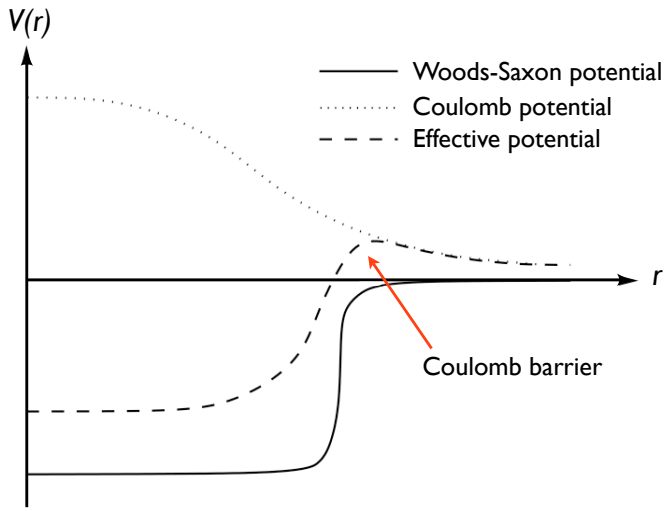

Figure 3.1: [Colour] The effective potential $V(r)$ between two nuclei separated a distance r. Also shown are the Coulomb and Woods-Saxons potentials that contribute to the effective potential.

increases with A.

The compound nuclei resulting from fusion reactions have large excitation energies, E^*, and angular momenta, $\boldsymbol{L}$, determined by the initial energy and momentum of the beam and the systematics of the reactions. The angular momentum of a compound nucleus is given by

$$\boldsymbol{L} = \boldsymbol{r} \times \boldsymbol{p}, \tag{3.1}$$

where $\boldsymbol{r}$ is the distance vector between the beam and target nuclear and $\boldsymbol{p}$ is the linear momentum of the incident nuclei. Due to conservation of energy, the compound nucleus has an excitation energy given by

$$E^* = Q_{\text{fus}} + E_{\text{cm}}, \tag{3.2}$$

where Q_{fus} is the Q-value for the formation of the compound nucleus and E_{cm} is the kinetic energy of the collision in the center of mass frame. E_{cm} is depen-

dent on the masses of the beam and target nuclei, m_b and m_t, respectively, and the kinetic energy of the beam, E_b, and is expressed as

$$E_{\rm cm} = \frac{m_t}{m_t + m_b} E_b. \tag{3.3}$$

The excitation energy of the compound nucleus is reduced towards the ground state in one of two ways. If the angular momentum is sufficiently large that the centrifugal force overcomes the attraction of the nuclear force, fast fission occurs within 10^{-19} s. Alternatively, if the excitation energy of the nucleus is sufficient, the compound nucleus can lose energy rapidly via a succession of proton, neutron or α-particle evaporations. Once the nucleus reaches the particle-evaporation threshold, at an excitation energy of $\sim$ 8 MeV it can only de-excite by the emission of high-energy statistical ($E1$) γ rays until it approaches the *yrast* line. The subsequent γ-ray decays to the ground state have lower energy and carry more angular momentum away from the nucleus until the nucleus reaches the ground state. It is these γ rays that are detected and from which level schemes can be deduced. A systematic diagram of a fusion-evaporation reaction is shown in Fig. 3.2.

Particle evaporation is an extremely effective process for reducing the excitation energy of the compound nucleus while maintaining the large angular momentum produced in the initial fusion reaction. Each particle evaporation removes $\sim$ 8-10 MeV of energy. Particles with angular momentum $l > 0$ are less likely to evaporate due to a barrier dependent on l, mass m and position r, given by

$$V_l(r) = \frac{l(l+1)\hbar^2}{2mr^2}. \tag{3.4}$$

This is illustrated in Fig. 3.2 by the steep decay slope towards the yrast line.

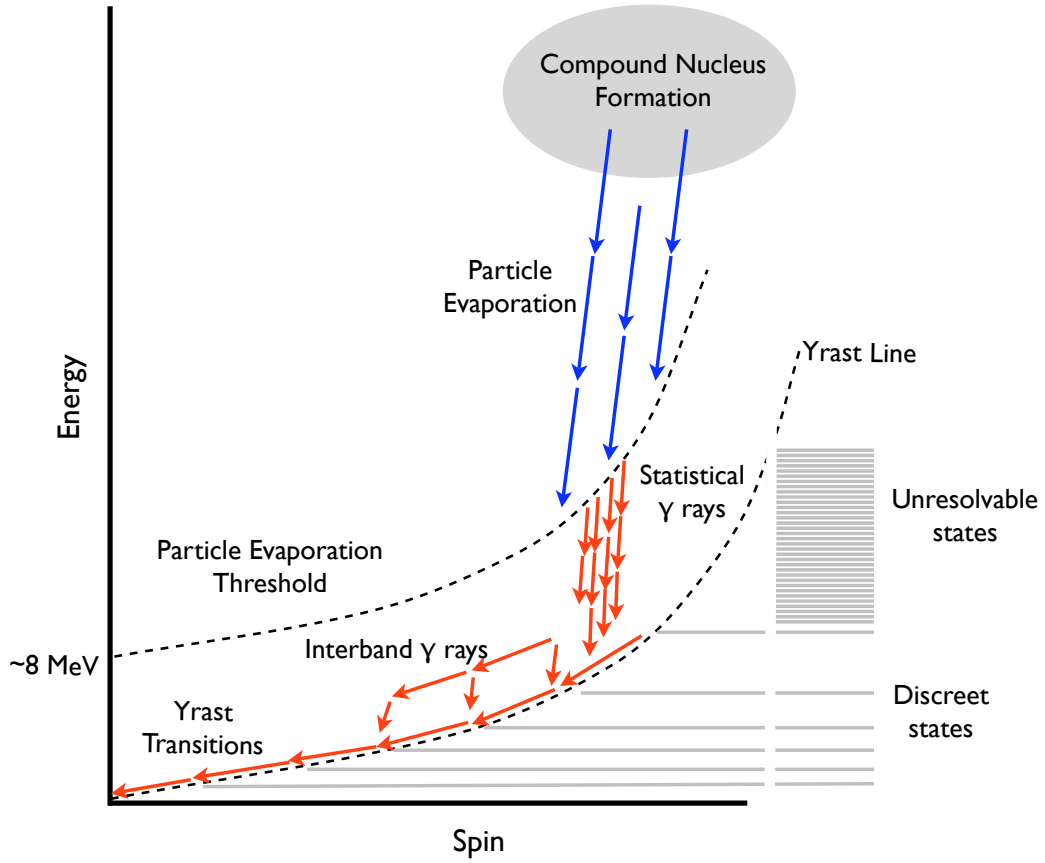

Figure 3.2: [Colour] A schematic representation of the decay to the ground state for compound nuclei produced in a fusion-evapouration reaction.

The emission of charged particles is similarly restricted by the Coulomb barrier, making neutron emission the most probable particle-evaporation channel.

The excited states of ^{180}Os were populated by the ^{150}Nd(^{36}S, 6n) fusion-evaporation reaction at ANL, where 6 neutrons are evaporated from the compound nucleus, ^{186}Os. The ^{36}S beam was produced and accelerated to 177 MeV using the ATLAS facility. The ^{150}Nd target was backed with two thicknesses of ^{197}Au, further details of the beam and targets are given in the

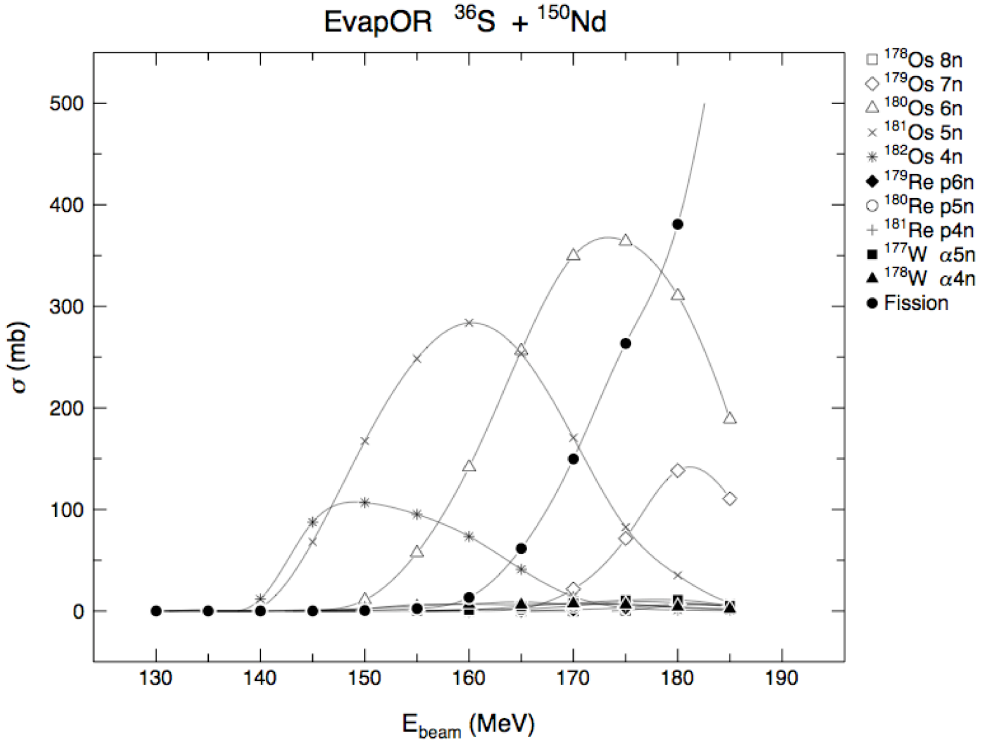

Figure 3.3: Theoretical cross sections for the ^{150}Nd(^{36}S, 6n) fusion-evaporation reaction produced by the *EvapOR* program.

following sections. The optimum beam energy for the production of ^{180}Os was calculated, using the *EvapOR* program [25], to be 174 MeV. A beam energy of 177 MeV was used to give a center-of-target energy of ∼174 MeV. The cross sections calculated by the *EvapOR* program are shown in Fig. 3.3. It can clearly be seen in this figure that the cross section for fission increases rapidly with the beam energy as expected form the increase in centrifugal force. The experimental percentage yields for the 6 neutron exit channel in the thick-target and thin-target experiments were measured to be 75% and 61%, respectively.

3.1.2 ATLAS beam

The ATLAS facility produces beams of ions with masses ranging from $A = 6$ to 238 which can be accelerated up to 15% of the speed of light [26]. For the current work, the ATLAS accelerator system produced a 177-MeV ^{36}S beam with an average beam current of 0.6 particle-nA (pnA) and beam pulses every 410 ns. A floor plan of the ATLAS system is shown in Fig. 3.4 demonstrating how the facility is composed of several complementary sections including two ion-production areas, the main ATLAS accelerator and several diverse experimental stations including the Gammasphere array housed in Target Area IV.

Ion beams can be injected to the main ATLAS accelerator by either the 9 MV electrostatic tandem Van Der Graaff injector or the Positive Ion Injector (PII). The tandem Van Der Graaff ion injector was used to produce the ^{36}S beams for the experiment discussed in this work. Negatively charged ions are produced in one of several types of sputter sources before being bunched and injected into the tandem accelerator.

The most commonly used negative-ion source is an Argonne-modified version of an inverted-sputter source [27]. Figure 3.5 shows a schematic representation of an inverted-sputter source. A $\sim$2 mA positive ion beam of alkali metal, such as caesium, is accelerated by an electrostatic potential and sputtered onto a conical target. The target is made of a material containing the isotope to be accelerated. The negative ions that are produced in the sputtering process are accelerated back through the electrostatic potential and focussed by an Einzel lens. More detailed descriptions of the negative-ion sources used with the tandem injector are given in Refs. [28–30].

The path of the negative-ion beam from the ion source through the tan-

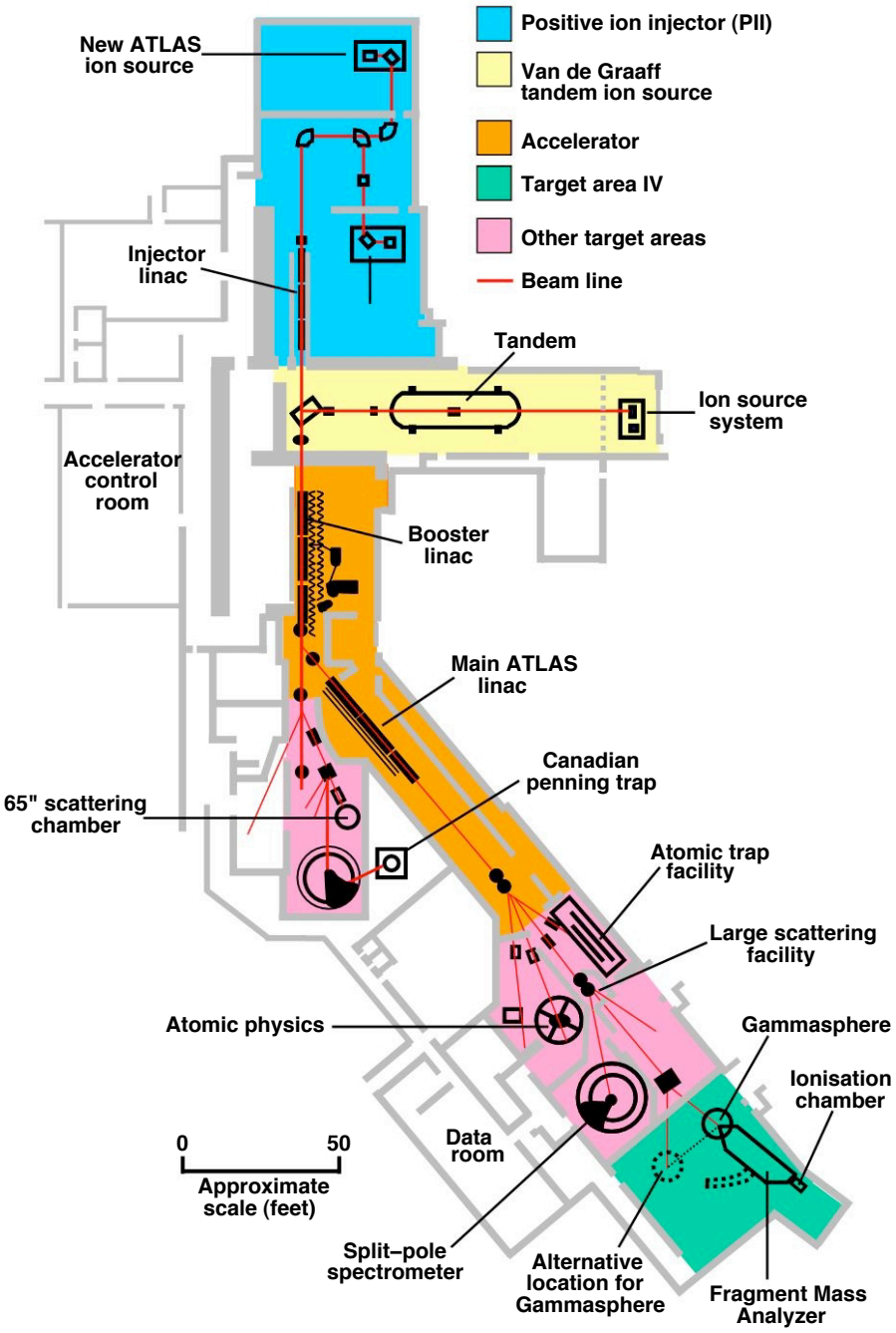

Figure 3.4: [Colour] A systematic floor plan of the ATLAS facility at ANL [7]

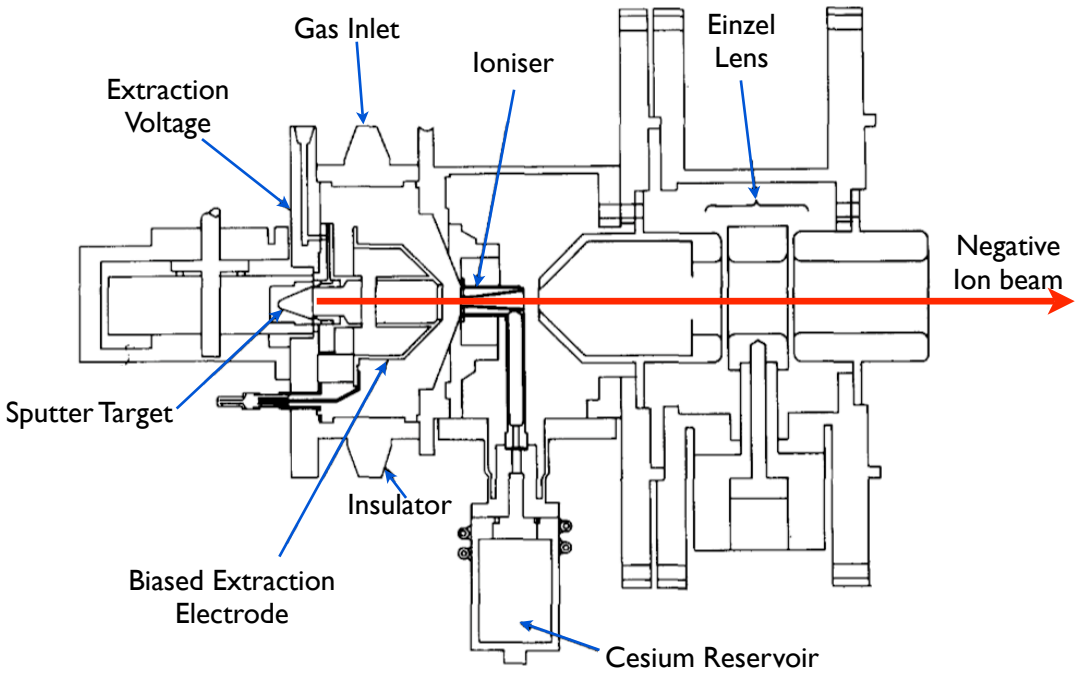

Figure 3.5: [Colour] Schematic diagram of an inverted-sputter negative-ion source adapted from Ref. [31].

dem and into the main ATLAS accelerating system is shown in Fig. 3.6. The negative DC beam from the ion source is bunched and injected into the tandem where it is accelerated towards the +9 MV terminal. The ion beam then passes through a foil stripper removing electrons and resulting in a positive beam which is accelerated back to ground potential. The beam then passes through a second stripper foil to produce higher charge states allowing for greater acceleration and a chopper removes any energy tails from the beam. The beam is then bunched, stripped and analysed prior to entering the main ATLAS accelerator linac. The beam bunchers operate at a frequency of 12.125 MHz resulting in a beam pulse every 82 ns. For this experiment an electromagnetic sweeper was utilized to retain only every fifth

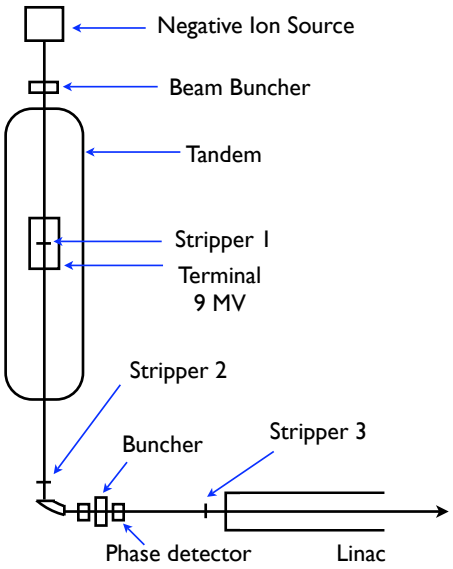

Figure 3.6: [Colour] Schematic diagram of the tandem injector at the ATLAS facility. The beam is produced in the negative-ion source, accelerated through the tandem accelerator and injected into the main ATLAS accelerator, adapted from Ref. [33].

pulse. The resulting beam collided with the target in pulses every 410 ns and allowed the observation of longer-lived states that would otherwise be obscured by more prolific prompt decays produced in each of the additional beam pulses [27, 32].

The main accelerating section of ATLAS consisted of the 20-MV Booster Linac and the 20-MV ATLAS linac where the beam undergoes the final acceleration up to velocities of 0.15 c. The Booster Linac and ATLAS linac are made up of a total of 42 superconducting split-ring resonators divided into 3 different types, each with its own optimum velocity for ion acceleration. Superconducting dipoles are situated after every two resonators and produce magnetic fields to keep the beam focussed. The resonators are toroidal shaped drift tubes constructed of pure niobium, cooled to 4.6 K by direct contact to liquid helium. Alternating current of frequency 97 MHz in the

resonators produce Radio-Frequency (RF) waves which accelerate the ions across a potential difference of up to 800 kV. The frequencies of the resonators are such that the velocities of the accelerated ions remain synchronous with the accelerating field and a wide rage of velocities can be achieved [34].

3.1.3 Targets

The target chamber is located in the center of the Gammasphere array and kept under vacuum conditions of $\sim 10^{-6}$ Torr. Two different ^{150}Nd targets, both isotopically enriched to 97%, were used in this study. Both targets were 900 μg/cm^2 thick. One target backed with 8 mg/cm^2 of ^{197}Au (henceforth referred to as *thick target*) was used to stop the recoiling nucleus in the centre of the detector array. Unhindered, the recoiling nuclei would exit the target chamber and the physical range of the Gammasphere detector array in $\sim$5 ns and the γ rays which are delayed by an isomeric state would not be detected. Stopping the nuclei in the center of the Gammasphere array allows the coincidence relationships between those γ rays emitted above and below isomeric states to be determined and the lifetimes of the isomers to be measured. Further details of the analytical techniques employed to do this are given in Section 4.2.

A drawback to reactions using the thick target is that transitions occurring between high-spin states are emitted before the recoiling nucleus has stopped in the backing material. This results in a Doppler broadening and a loss of resolution for the subsequent photopeaks. To overcome this, an alternate target with a thin, 200 μg/cm^2 ^{197}Au backing (henceforth referred to as *thin target*), was used for part of the experiment. This target allowed the recoiling nuclei to continue to pass through the array and a Doppler cor-

rection was applied to account for the shift in gamma-ray energy as a result of in-flight emission (see Section 4.1.2).

In addition to the backing material, each target had thin layer of ^{197}Au on the front. The thicknesses were 100 μg/cm^2 for both the thin and thick targets and prevented the oxidation of the ^{150}Nd targets. The thick-target experiment ran for approximately four days and the thin-target experiment for approximately one day.

3.2 γ-ray detection

The resolving power R, of a detector is a common measure of quality of the resulting spectra and is dependent on the resolution of the detector ΔE_γ, and the peak-to-total ratio P/T. Resolving power is given by

$$R = \frac{SE_\gamma}{\Delta E_\gamma} P/T, \tag{3.5}$$

where SE_γ is the average separation of the γ rays in a cascade and a property of the nucleus being studied [35]. For an n-fold γ-ray coincidence the Resolving power is given by

$$R = \left(\frac{SE_\gamma}{\Delta E_\gamma} P/T \right)^n . \tag{3.6}$$

The power n represents the increase to an n-dimensional space in which the photopeaks must not share the same volume [36]. Energy resolution is an intrinsic property of the detector and P/T can be improved by the implementation of Compton suppression shields. The Gammasphere array used in this experiment is currently considered as one of the most powerful germanium detector arrays. The properties and set-up of the Gammasphere array are discussed in the following sections.

3.3 Gammasphere

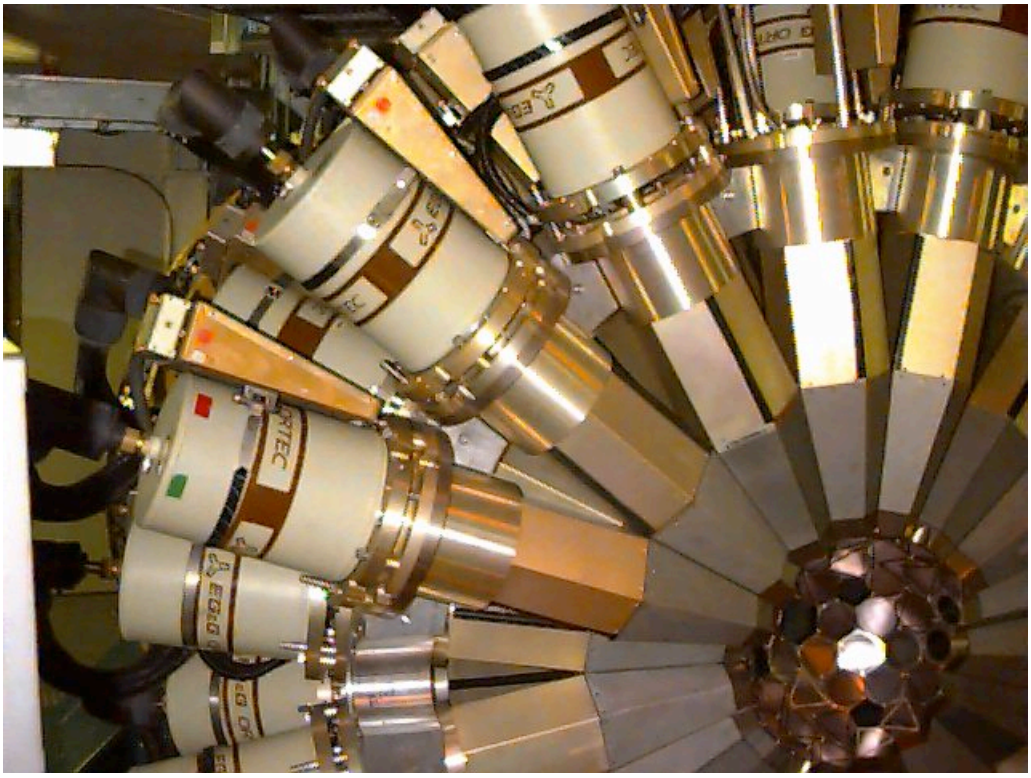

Figure 3.7: [Colour] Photograph of the Gammasphere detector array showing the interior view complete with detectors and the hollow in which the target chamber fits.

The Gammasphere detector array is stationed in Target Area IV (see Fig 3.4) of the ATLAS facility. The array is consists of 110 high-purity Germanium detectors (HPGe) surrounded by Bismuth-germanate (BGO) Compton-suppression shields, held in place in a polyhedral skeleton structure. The polyhedral skeleton is comprised of 122 elements: 110 hexagons for the detectors, 2 pentagons for the beam-line and 10 pentagons for ancillary detectors. The skeleton is in two separate pieces which can be mechanically separated to allow access to the target chamber. Figure 3.7 shows an interior view of one of the halves of the Gammasphere array complete with detectors

and the hollow which fits around the target chamber. When closed in position the front of the HPGe detectors are 25 cm from the target position and the total Gammasphere array provides a 45.98% geometrical coverage of the γ-ray source.

A schematic diagram of an individual detector modules is illustrated in Fig. 3.8. The central coaxial n-type HPGe detectors measure 71 mm in diameter and 84 mm in length. They are cooled to 77 °K by liquid nitrogen to reduce any background resulting from the thermal excitation of valence electrons across the 0.7 eV band gap [37]. At E_γ=1.3 MeV the detectors have an energy resolution of ΔE=2.2 keV, when measured with a stationary ^{60}Co source, and a total array efficiency of 9.4% [38, 39]. Six BGO Compton suppression shields are positioned in a hexagonal arrangement around each of the HPGe detector to allow close packing of the detector modules. Details of the BGO detectors and their role in Compton suppression are given in the next section.

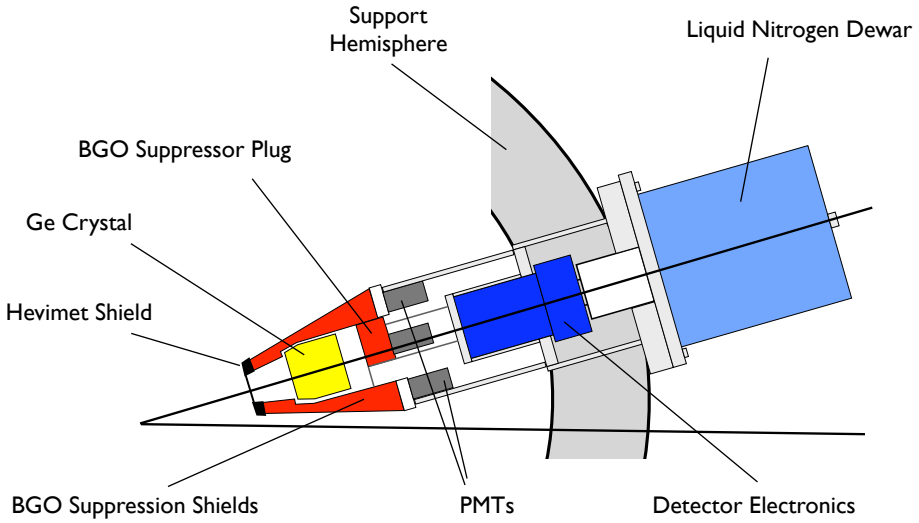

Figure 3.8: [Colour] Schematic diagram of a single Gammasphere detector module, adapted from Ref. [38].

The detectors are grouped into 17 rings with constant angle θ, with respect to the beam line. Details of θ and the number of detectors in each ring are given in Table 3.1. This information is utilised in the analysis of the angular distributions of the γ-ray radiation and was used in the measurement of DCO ratios in this work (see Section 4.4.1). The array is symmetrical about 90°, as demonstrated by the values of $\cos^2\theta$ in Table 3.1, with detectors of θ $< 90°$ and $> 90°$ called forward and backwards, respectively.

Ring	Number of Detectors	θ	$\cos^2\theta$
1	5	17.27	0.9119
2	5	31.72	0.7236
3	5	37.38	0.6314
4	10	50.07	0.4120
5	5	58.28	0.2764
6	10	69.82	0.1190
7	5	79.19	0.0352
8	5	80.71	0.0261
9	10	90.00	0.0000
10	5	99.29	0.0261
11	5	100.81	0.0352
12	10	110.18	0.1190
13	5	121.72	0.2764
14	10	129.93	0.4120
15	5	142.62	0.6314
16	5	148.28	0.7236
17	5	162.73	0.9119

Table 3.1: Detector distributions in the Gammasphere array, in terms of the angle, θ, of all the detectors in a ring relative to the beam line. The value $\cos^2\theta$ demonstrates the symmetry of the array about ring 9 at 90°.

The angle of a detector relative to the beam line was also used in the Doppler correction applied to thin-target data. The angle to the centre of

the HPGe crystal, θ, is accurate to 0.01°. However, it is not known where, within the detector, the γ ray interacts. For the 54 detectors between 50°$\leq$ θ $\leq$140°, electronic segmentation divides the detectors into two or three sections improving the accuracy of the angle used in Doppler correction. Further information of the Doppler correction process is given in Section 4.1.2.

In this experiment the entire ring of detectors at θ=17.27°, two detectors at θ=90° and one at θ=148.28° were not used.

3.3.1 Compton supression

If a γ ray Compton scatters within the HPGe crystal only a portion of its initial energy is transferred to the detector. The scattered γ ray has an energy, E'_γ, related to the angle through which it scatters, θ, given by

$$E'_\gamma = \frac{1}{1 + \frac{1}{m_e c^2}(1 - \cos\theta)} E_\gamma, \tag{3.7}$$

where E_γ is the initial energy of the γ ray. If the scattered γ ray leaves the detector without further interaction with the HPGe crystal only a fraction of its energy will be measured. This will result in a background in the γ-ray spectra at energies less than the photopeak energy. Compton suppression is implemented to reduce this Compton background by vetoing those events where the scattered γ ray is detected the surrounding suppression shield.

As described in the previous section the HPGe crystals in Gammasphere are surrounded by six bismuth-germanate (BGO) scintillator crystals. A BGO back plug is also in place to detect the scatters through small angles. Ideally only those transitions where the total energy of the γ ray is deposited in the HPGe crystal (good events) should be recorded, therefore the number of scattered γ rays that pass though the shield undetected needs to be

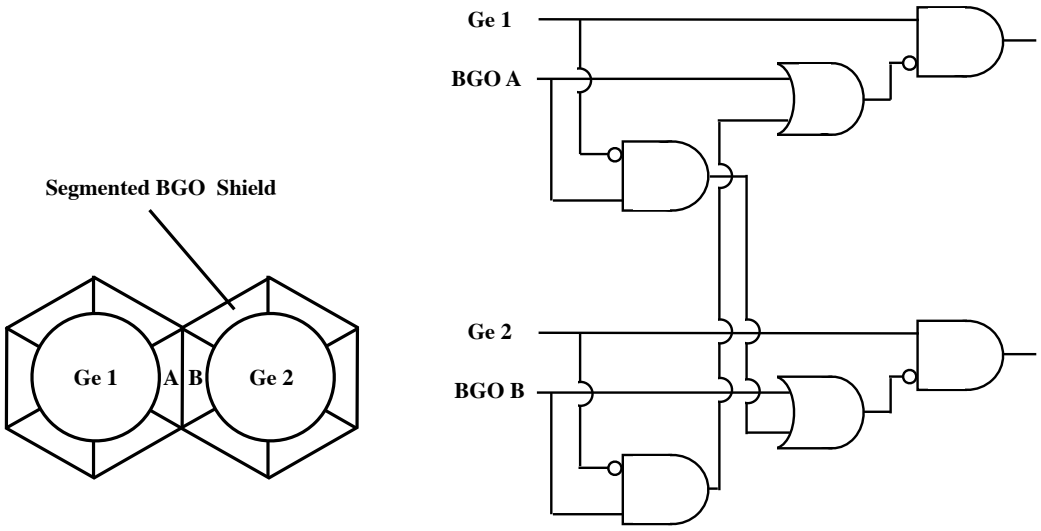

Figure 3.9: The honeycomb formation of the BGO shield for two adjacent Gammasphere detector modules. The logic system for event vetoes based on Compton suppression is also shown [41].

minimised. Although the energy resolution of a BGO detector is poor compared to an HPGe detector, the high Z of bismuth provides a high efficiency, making it the ideal choice for Compton suppression shields [40].

The six BGO shields are in an electronic-honeycomb configuration, shown in Fig. 3.9 [41]. BGO segments A and B are combined electronically so that an event in Ge1 can be vetoed by a signal in either A or B. If coincident signals are produced in both Ge1 and Ge2 then the event in Ge1 may only be suppressed by a signal from A and an event in Ge2 may only be suppressed by a signal in B. This is summarised in the logic system shown in Fig. 3.9. False vetoes may occur if a γ ray is directly incident on a BGO crystal adjacent to a HPGe detector measuring a good event. This is prevented by fitting lead collimators to the front of the BGO shield, stopping any direct interaction with the BGO shields. Figure 3.10 shows the effect of Compton suppression

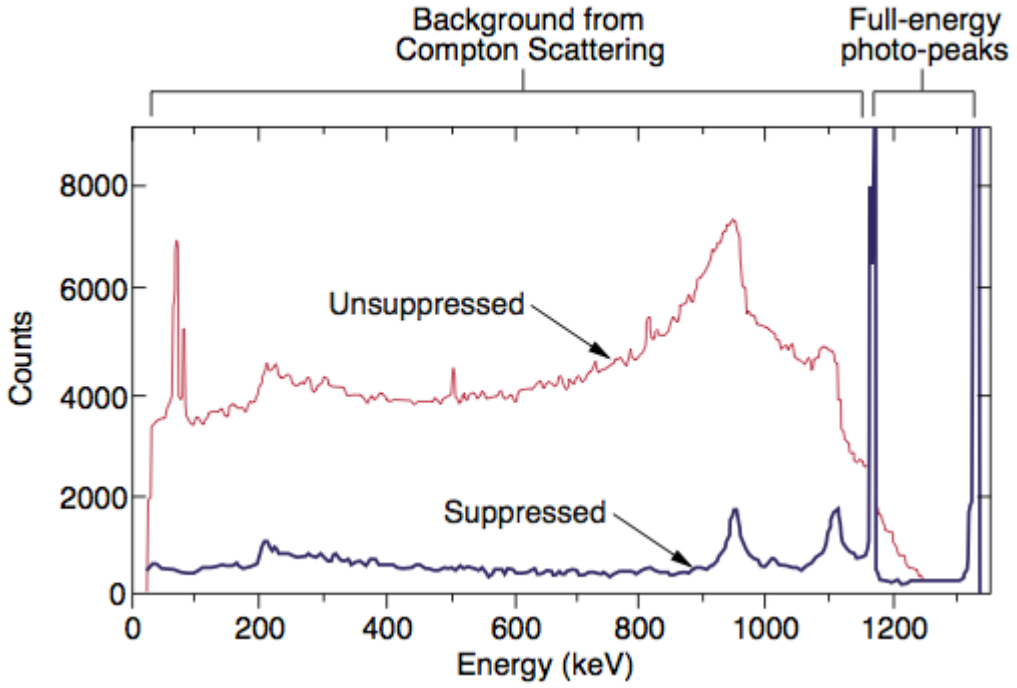

Figure 3.10: [Colour] γ-ray spectra from a ^{60}Co source in the Gammasphere array. The effect of Compton Suppression by BGO crystals is demonstrated in the suppressed (blue) spectrum and the unsuppressed (red) spectrum.

on a Ge spectrum of ^{60}Co. Although some Compton background remains with the suppression it makes a significant reduction in the background while maintaining the area in the full-energy peak. The peak-to-total (P/T) for the entire Gammasphere detector improves from $\sim$25% without Compton supression to $\sim$70% with the complete Compton suppression shield [39].

3.3.2 Gammasphere electronics and data acquisition

The Gammasphere electronics consist of a series of amplifiers, discriminators, analogue-to-digital converters (ADC) and time-to-analogue converters (TAC) housed in custom-built VXI modules. The role of the electronics is to digitise

the energy signals and create timing signals which can be processed by the data acquisition (DAQ) system. The DAQ system is responsible for defining events through a series of variable pre-set triggers and the subsequent storage of data.

Figure 3.11 shows a block diagram of the electronics used to process the HPGe and BGO signals for one detector module in the Gammasphere array. The *fast*-timing and *slow*-energy analogue signals, generated by the accumulation of charge in the HPGe detectors, first undergo pre-amplification within the detector module. The high-resolution Ge-energy signal is further amplified and then digitised in an ADC, with a total duration of $\sim$10 μs. A logic signal is produced for the Ge-timing signal by either a constant-fraction discriminator (CFD) or leading-edge discriminator. The later is implemented for $E_\gamma < 200$ keV to avoid rejection due to low-rise times. A TAC is used to measure the time of the signal with respect to the Main Trigger (MT). Further discussion on the timing signals is given in the following section. The timing signal is then digitised in an ADC and processed in the DAQ system.

The BGO detectors are each connected to photo-multiplier tubes to amplify the signals. Each signal then passes through a discriminator to provide fast-timing information and then they are added together to give the total BGO energy signal. The timing and energy signals are then processed in the same way as the HPGe signals.

Timing signals from the HPGe and BGO detectors are also fed into a logic board to provide Compton suppression as described in Section 3.3.1. The signals created in the logic boards of all 110 Gammasphere-detector modules are combined in the DAQ system to determine if the pre-set trigger conditions were met. Triggers ensure that only events with a sufficient γ-ray

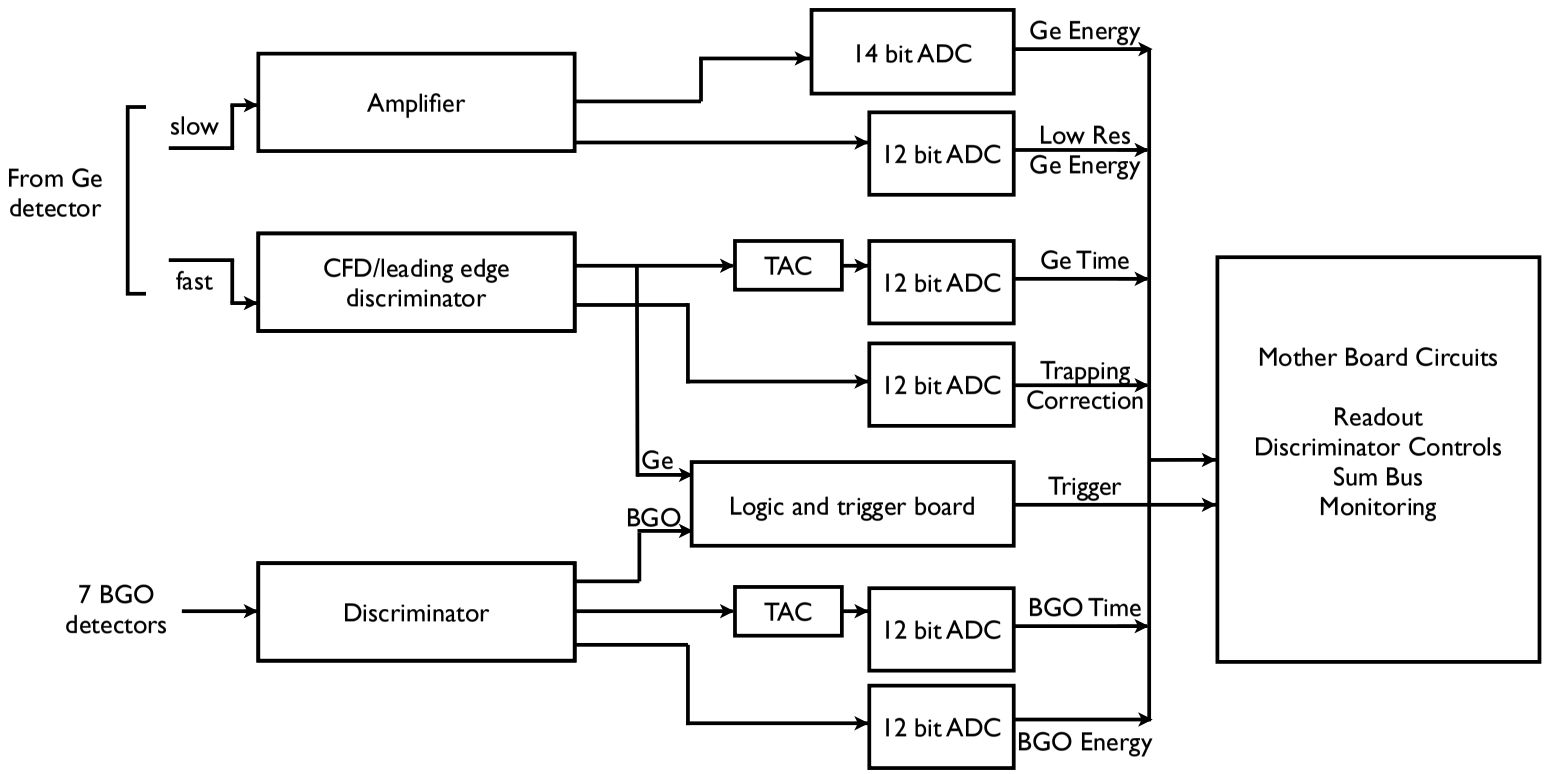

Figure 3.11: Block diagram of a single Ge-BGO detector-module electronics, adapted from Ref.[42]. The stop signal for the TACs are the timing signal from the master trigger, MT (see Section 3.3.3). Each of the functions is implemented by a daughter board that plugs into the VXI board.

multiplicity, chosen to suit the coincidence analysis to be implemented, are recorded.

The Gammasphere DAQ utilises three triggers: the pre-trigger (PT), main trigger (MT) and late trigger (LT). Each time a signal is produced in a HPGe detector a 50 mV signal is added to the sumbus in the motherboard for 2 μs. If a signal is also detected in a adjacent BGO detector the signal is cut short. Figure 3.12 (a) and (b) show the signals created for both a clean and Compton suppressed signal, respectively. The signals from all the detector modules accumulate in the sumbus and the PT is set to be satisfied when the voltage in the sumbus reaches a level equivalent to the multiplicity of γ rays required. The MT is applied 600 ns after the PT to ensure that system does not trigger on Compton-suppressed signals.

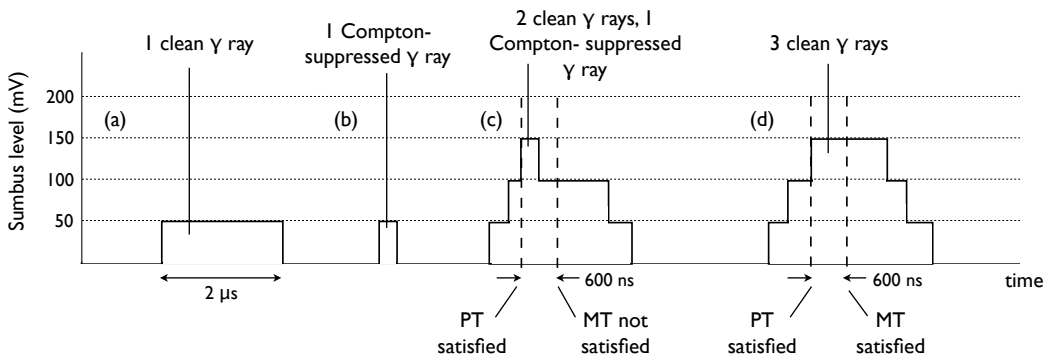

Figure 3.12: Sumbus signals for clean and Compton suppressed γ-ray events. (a) A clean γ ray. (b) A Compton suppressed γ ray. (c) An example of the PT being satisfied by 2 clean γ rays and a Compton suppressed γ rays. (d) Both the PT and MT being satisfied by 3 clean γ rays.

In this experiment both the PT and MT were set to require three coincident γ rays, ie. 150 mV. It is possible that the PT conditions can be met by two clean γ rays and a Compton suppressed signal but not satisfying the MT

conditions, as illustrated in Fig.. 3.12 (c). The DAQ will not be triggered unless the MT is also satisfied by three clean γ rays, shown in Fig. 3.12(d). The LT is applied 6 μs after the MT. The LT is generally used when ancillary detectors with slower signal processing are used. In this experiment the LT sampled the total number of γ rays recorded in a event and was set to equal the MT. On average the rates of the PT and MT in this experiment were $\sim$16 kHz and $\sim$8 kHz, respectively, showing the advantage of using the two triggers in tandem.

3.3.3 Timing

The time that each γ ray is detected with respect to the beam burst is used to determine γ-ray coincidences across isomeric states and to measure the lifetimes of states. Several TACs are used to measure the time differences between signals and are combined to give the time of the γ-ray signal with respect to the intrinsic RF of the accelerator, T_{γ}^{RF}.

A TAC is used to measure the time that each HPGe detector produces a signal from an incident γ ray with respect to a signal produced when the MT conditions have been satisfied. The HPGe signal is used as the start signal for the TAC which remains open for 2μs or until it receives a stop signal from the MT. The timing of the MT is in turn measured with respect to the RF of the accelerator by a second TAC, referred to as TAC2. The start signal for TAC2 is the MT and the following RF signal is used as the stop signal. The correct RF signal is selected by an overlap with a PT logic signal. Combining TAC and TAC2 gives the timing of the γ-ray signal with

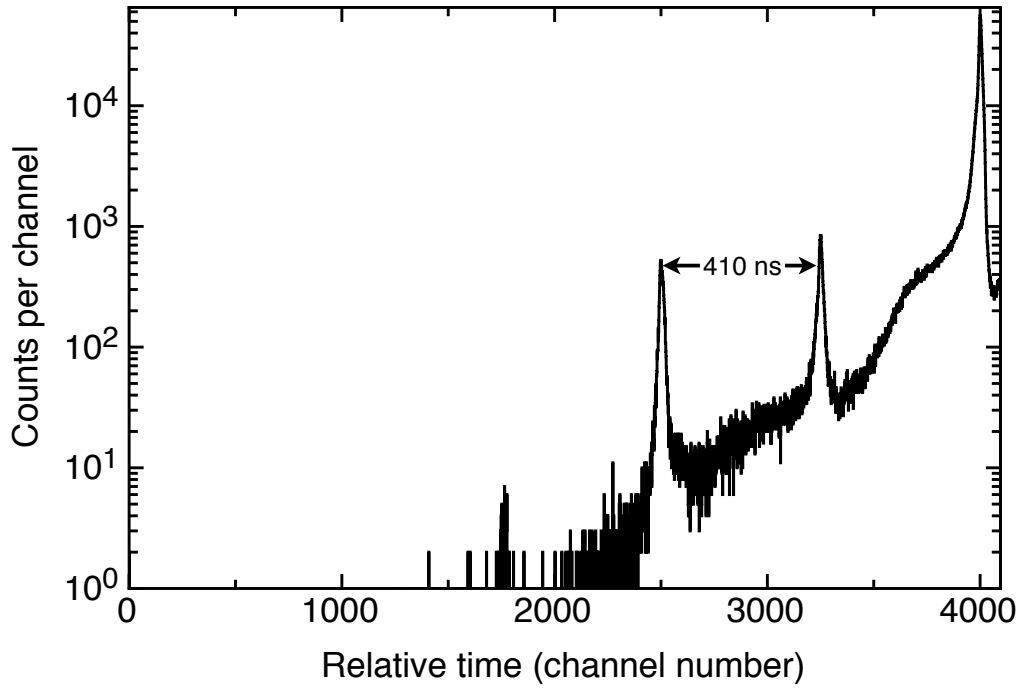

Figure 3.13: A reverse-time spectrum for a single detector produced in this experiment. The γ ray is timed with respect to the RF signal.

respect to the RF by

$$\begin{aligned} T_{\gamma}^{RF} &= TAC - TAC2 \\ &= T(\gamma - MT) - T(MT - RF) \\ &= T(\gamma - RF). \end{aligned} \tag{3.8}$$

Figure 3.13 shows an example of a time spectrum produced in this work for one HPGe detector. The large peak at 4000 channels represents the prompt γ rays associated with the reaction. Time decreases with channel number due to the HPGe signal being the start signal for the TAC. The γ rays detected first will give the largest time before the TAC is stopped by the MT creating the time-reversed spectrum. Secondary peaks can also be seen in this spectrum. These are due to the beam pulses following the initial reaction and are 410 ns apart. They are substantially lower in intensity and

are caused by reactions with relatively large cross-sections such as transfer and coulomb excitation reactions. The background caused by these peaks is removed by the application of time gates in the production of coincidence matrices. Further information on coincidence matrices are given in the next chapter.

Chapter 4

γ-ray spectroscopy techniques

The analytical techniques used to process the raw data from the Gammasphere experiment into meaningful spectra and thus interpret the nuclear structure, are described in this chapter. The techniques discussed include the initial calibrations of the data and the processes used to create multi-dimensional data histograms from which spectra are produced. The methods used to measure nuclear lifetimes are also discussed along with the analytical tools used to determine the spin and multi-quasiparticle configurations of states within a level scheme.

4.1 Preliminary sorting and calibration

A total of $\sim$ 90 GBytes of data were collected for the experiment described in the previous section. The data for each Gammasphere event are stored as binary data *words* and contain all the parameters associated with the individual γ rays detected within that event. This includes several timing and energy parameters and information from the BGO detectors. In order

to minimise processing time of this large data set, a preliminary sort code was utilised to reduce the data to contain only those calculated parameters required for further analysis. For each γ ray detected in an event, the data was rewritten to contain only the ID number of the HPGe detector firing, the gain-matched energy of the γ ray detected and the time the γ ray was calculated to be detected with respect to the RF frequency (see Section 3.3.3).

4.1.1 Gain matching

The energy and time measured for individual detectors can vary due to differences in the gain of amplifiers in the electronic system. For the Gammasphere array, the detectors are generally accurately gain matched and require little alteration in the sorting process. However, gain shifts can occur over time and must be accounted for in data analysis. Gain matching corrections for energy and time measured in each detector were applied in the preliminary sort code.

The detectors in the Gammasphere array were calibrated using ^{152}Eu and ^{182}Ta γ-ray sources. Energy spectra for the calibration sources were produced for each individual detector and the centroids of the γ-ray peaks were measured. The energy for the γ rays in the calibration sources, E_γ, were taken from published values [43] and a straight line calibration was fitted to the data for each detector. The intercepts and gradients of the calibration for each detector were used in the preliminary sort code to gain match the energy peaks. The pre-sorted data were written so that each channel represented one third of a keV in energy.

Time-dependent shifts in the energy gain of the detectors were corrected using a similar method. Energy spectra for each detector were produced at

frequent time intervals in the data. The photopeaks from transitions in ^{180}Os with the highest intensities were used recalculate the calibration parameters when gain shifts were detected.

Considering the importance of the timing measurements in this experiment, even a small difference in the position of the beam-pulse peaks need to be corrected. Spectra showing the timing of the individual γ-rays with respect to the RF were produced for each detector, for the first 2 GB of data collected. Figure 4.1 shows an example of the time spectra produced for two detectors before any corrections were made.

The centroids of each beam pulse was measured and fitted with a straight line to the positions that the beam-pulse peaks were aligned to. Since the timing spectra are reversed (see Section 3.3.3) the first beam pulse was assigned to have 4000 channels and the second and third beam pulses were aligned to 3290 and 2580 channels, respectively. The beam pulses are separated by 710 channels in the gain matched spectra. This corresponds to the 410 ns between each beam pulse. It follows that each channel in the timing spectra represent 710/410 ns. Timing spectra were also produced for each detector at frequent time intervals throughout the course of the experiment and the parameters were recalculated when further gain shifts occurred.

4.1.2 Doppler correction

The Doppler correction necessary for the data collected from the thin-target section of the experiment was also performed in the preliminary sort code. The daughter nuclei created in the thin-target fusion-evaporation reactions continue to recoil through the target chamber. A γ ray emitted from a nucleus recoiling with a velocity v, at an angle θ from the velocity vector, is

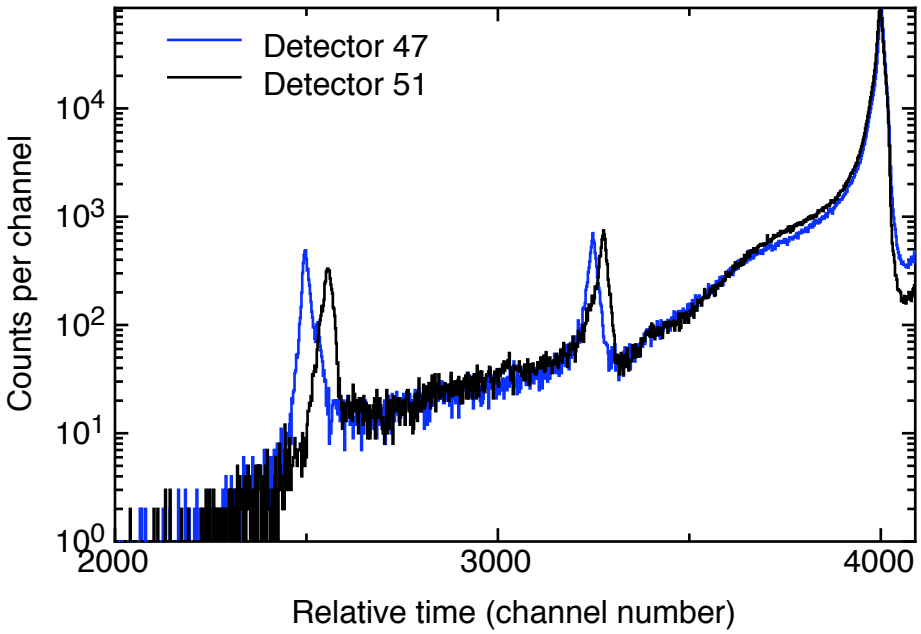

Figure 4.1: [Colour] Time spectra for detectors with ID numbers 47 (blue) and 51 (black), before gain matching.

measured to have an energy given by the relativistic Doppler equation,

$$E'_\gamma = E_0 \frac{\sqrt{1-\beta^2}}{1-\beta\ cos\ \theta}, \tag{4.1}$$

where E_0 is the true energy of the γ ray and β is the ratio of the recoil velocity to the speed of light, (v/c). For non-relativistic recoil velocities this can be simplified to

$$E'_\gamma = E_0\ (1+\beta\ cos\ \theta). \tag{4.2}$$

It was assumed that the detector angle was equal to the angle at which the γ-ray was emitted relative the velocity vector, θ. The recoil velocity will vary with the exit channel of the reaction and as such β must be measured for the specific nucleus. The Doppler-shifted energy measured for a γ-ray peak, E'_γ, in ^{180}Os was plotted as a function of detector angle. A straight line was fitted to the data and β=0.0176 was deduced from the fitted parameters. This

Doppler correction was then applied for each detector in the preliminary sort of the thin-target data.

4.1.3 Efficiency calibration

The relative efficiency of HPGe detectors vary with the energy of the γ ray being detected. In order to measure the relative intensity of γ transitions the relative effieciency for the detector array must be known. The relative efficiency for a given photopeak, ϵ_{rel}, is determined by

$$\epsilon_{rel} = \frac{N}{I_{rel}}, \tag{4.3}$$

where N is the number of counts in the photopeak and I_{rel} is the relative intensity of the γ ray. ^{152}Eu and ^{182}Ta calibration sources were used to establish the relative efficiency curve for the Gammasphere detector array. The number of counts in the photopeak in the calibration spectra were normalised and the relative intensities were taken from Ref. [43]. The *EFFIT* program [44] was used to fit the relative intensities to a pseudo-empirical function with the form

$$\epsilon_{rel} = \exp\left[(A + Bx + Cx^2)^{-G} + (D + Ey + Fy^2)^{-G}\right]^{-1/G}, \tag{4.4}$$

where x and y are given by

$$x = \log\left(\frac{\mathrm{E}_\gamma}{100\ \mathrm{MeV}}\right) \tag{4.5}$$

and

$$y = \log\left(\frac{\mathrm{E}_\gamma}{1000\ \mathrm{MeV}}\right). \tag{4.6}$$

The fitted parameters A, B and C describe the efficiency at low energy and parameters D, E and F describe the efficiency at high energy. The parameter G describes the interaction between the high and low energy regions.

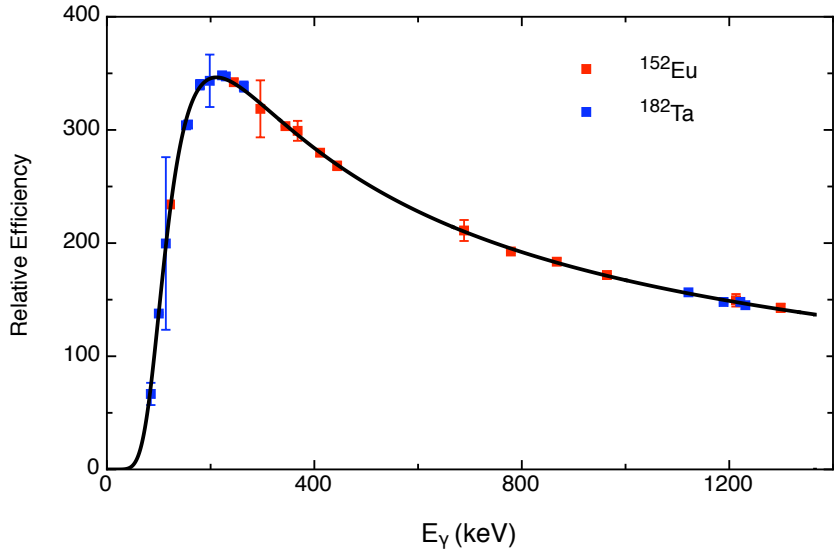

Figure 4.2: [Colour] The efficiency calibration of the entire Gammasphere array (black) normalised to ^{152}Eu (red) and ^{182}Ta (blue) source peaks.

Figure 4.2 shows the efficiency data and curve produced in this work for the entire Gammasphere array.

4.2 Histograms

4.2.1 Matrices, cubes and hypercubes

In order to establish a level scheme, the coincidence relationships between γ-ray transitions was investigated in $\gamma\gamma$ matrices, $\gamma\gamma\gamma$ cubes and $\gamma\gamma\gamma\gamma$ hypercubes. In a 2-dimensional $\gamma\gamma$ matrix, γ-ray energy, E_γ, is plotted against E_γ, and is incremented by the number of counts at the energy coordinates for coincident γ-ray pair. For example, if an event contains a coincident γ-ray pair, $E_{\gamma 1}$ and $E_{\gamma 2}$, the number of counts in the matrix will be incremented at ($E_{\gamma 1}$,$E_{\gamma 2}$) and ($E_{\gamma 2}$,$E_{\gamma 1}$). In this case, where no additional conditions have been applied in the sort code, a matrix symmetric about $E_{\gamma 1}$=$E_{\gamma 2}$ is

produced. Once the data are sorted into a matrix, coincidences are studied through the application of *gates*. A *gate* set at an energy E_γ effectively takes a *slice* of the matrix at the this energy and projects a spectrum showing the number of counts that each coincident energy was observed.

A 3-dimensional $\gamma\gamma\gamma$ cube contains an additional E_γ axis. In order for the cube to be incremented three γ rays must be detected in coincidence. Gates can be set on two axes of a cube (a double gate) to project a spectrum containing only those γ-ray transitions in coincidence with the both of the γ rays on which the gates were set. Similarly, a 4-dimensional $\gamma\gamma\gamma\gamma$ hypercube contains four E_γ axes and requires a 4-fold γ-ray coincidence in order to be incremented. Gates can be set on three γ-ray energies (a triple gate) to project a spectrum containing only those γ-ray transitions in coincidence with all three γ rays.

Additional timing conditions were applied in the sort codes for these 2-, 3- and 4-dimensional symmetric histograms. In order to look at only those transitions unhindered by isomeric states, a condition was set that only those transitions detected within 12 ns of the initial reaction were included. These transitions are referred to as prompt transitions. Any γ rays detected after the 12-ns window are considered to be hindered by an isomeric or long-lived state and are termed delayed. It is important that the second and third beam-pulse peaks be avoided when selecting the time range for delayed histograms.

The 2-dimensional matrices were analysed using the software system DAMM, part of the UPAK software suite [45]. This program was also used for the analysis of the non-symmetric matrices described in the following section. The width of the gates was generally selected to be the full width

of the peak however this was modified to accommodate any contaminating peaks. Background contamination was subtracted in one of two ways. Local background was removed by subtracting a second gate of equal channel width at an energy close to that of the γ ray being studied. However, this is not always possible when there is a high density of γ rays so a fraction of the total projection of the matrix was often subtracted instead.

The RadWare [46] software package was used for the analysis of cubes and hypercubes. This software allowed double and triple gates to be set to study higher-fold coincidences. Background was subtracted within the RadWare program using algorithms based on subtracting multiple background gates in the region of the Compton background [47].

A particularly useful function in this software was to create *gatelists*. This allowed numerous photo-peak gates to be stored as a list and used in double and triple gates. This resulted in a spectrum containing the sum of each combination of individual gates within the *gatelists*. For example, a triple gate between *gatelists* a and b, where gatelist a contains transitions a_1, a_2, and a_3, and gatelist b contains transitions b_1 and b_2, is equivalent to the sum of the triple gates a_1 and b_1, a_1 and b_2, a_2 and b_1, a_2 and b_2, a_3 and b_1 and a_3 and b_2. Many of the spectra shown in Chapter 5 represent those produced using *gatelists*. In order to keep explanation of the spectra concise a simplified notation is adopted. A *gatelist* containing all the transitions between levels I_1^π and I_2^π is simplified to $(I_1^\pi \rightarrow I_2^\pi)$. A double gate on two *gatelists* is described by the notation $(I_1^\pi \rightarrow I_2^\pi)/\ (I_3^\pi \rightarrow I_4^\pi)$ and similarly $(I_1^\pi \rightarrow I_2^\pi)/\ (I_3^\pi \rightarrow I_4^\pi)/\ (I_5^\pi \rightarrow I_6^\pi)$ describes a triple gate.

In addition to the symmetric histograms discussed above, non-symmetric $\gamma\gamma$ matrices were created to contain different sets of γ rays on either axis.

These non-symmetric matrices were produced by placing additional conditions within the sort code. Individual criteria were specified for each axis and must be met before the matrix was incremented. Non-symmetric matrices produced in this work include prompt-delayed coincidence matrices, ΔT matrices and the matrices used for R_{DCO} analysis, discussed in Section 4.4.1

4.2.2 Prompt-delayed coincidence matrices

A prompt-delayed $\gamma\gamma$ matrix has the transitions above an isomeric state (*prompt*) on one axis and those hindered by an isomeric state (*delayed*) on the other. The prompt transition must be detected a specific time before the delayed transition, ΔT, yet still be within the same Gammasphere event and therefore coincident. The range of ΔT used for each matrix was governed by the half-life, $T_{1/2}$, of each particular isomer being investigated, generally given by

$$T_{1/2} \ \leq \ \Delta \, T \ \leq \ 3 \, T_{1/2}. \tag{4.7}$$

Gating on a prompt γ ray in a prompt-delayed matrix will produce a spectrum of the transitions delayed by that specific range ΔT. It follows that a gate on the delayed γ rays will reveal the associated prompt transitions.

The ΔT technique was extended further to create symmetric matrices showing the prompt $\gamma\gamma$ coincidences above a particular isomer. These matrices were only incremented when a coincident delayed γ ray, preferably decaying directly out the isomeric state, was detected at a time ΔT after the initial promptly-coincident γ rays. Transitions were determined to be promptly coincident if they are detected within 12 ns of each other. Similarly, delayed $\gamma\gamma$ matrices were produced to show delayed coincidences below a specific isomer.

4.2.3 ΔT matrices

In order to determine the half-life of an isomeric state a time spectrum must be produced. In this work ΔT-prompt γ-ray matrices were created specifically for each isomer. A condition was applied in the sort code so that only γ rays in coincidence with a delayed γ ray decaying directly from the isomer were included in the matrix. The energy of any γ ray in prompt coincidence with these delayed transitions was placed on one axis of the matrix. The time difference ΔT between the prompt and delayed γ rays was recorded on the other axis. A gate on a prompt γ ray in this matrix will produce a ΔT spectrum which is also gated by a decay from the isomer, effectively isolating the isomeric state. This process eliminates any secondary isomeric feeding from the half-life measurement.

4.3 Lifetime measurement

The life times of the isomeric states presented in this work were determined from the ΔT spectra. For half-lives greater than $\sim$30 ns the data were fitted with an exponential decay of the form,

$$N(t) = N_0 \exp(-\lambda t) + A, \tag{4.8}$$

where N_0 and $N(t)$ are the initial number of counts and the number of counts at a time t respectively. A is a constant background and λ is the decay constant. Half-life is related to the decay constant by

$$T_{1/2} = \frac{\ln 2}{\lambda}. \tag{4.9}$$

4.3.1 Nanofit

For half-lives less than ∼30 ns the Gaussian time resolution of the system (∼10 ns) becomes comparable to the half-life and must be accounted for. A Gaussian peak convoluted with an exponential decay has the form

$$\frac{A}{\sqrt{2\pi}\sigma}\exp\left(\frac{-(t-\mu)^2}{2\sigma^2}\right)\otimes B\exp(-\lambda t) = \frac{AB}{2}\exp\left(-\lambda t-\frac{\mu^2}{2\sigma^2}+2\left(\sigma\lambda-\frac{\mu}{\sigma}\right)^2\right)\mathrm{erf}\left(\frac{t}{\sqrt{2}\sigma}-\sqrt{2}\left(\sigma\lambda-\frac{\mu}{\sigma}\right)\right), \tag{4.10}$$

where μ and σ are the mean and standard deviation of the Gaussian, A and B are scaling factors of the Gaussian and exponential components, respectively, and erf is an error function. This function was fitted to the data using the code, *nanofit* [48], based on a χ^2 minimisation.

4.4 Nuclear structure techniques

4.4.1 DCO ratios

The total angular momentum of the beam and target in a heavy-ion fusion reaction (defined by Equation 3.1) is conserved and the spin of the compound nucleus is aligned in a plane perpendicular to the beam direction. Therefore all the compound nuclei will have a zero projection of spin on to the beam axis, ie. in the $m = 0$ substate. As particles evaporate from the compound nuclei the alignment is perturbed resulting in a Gaussian distribution of the m substate population, $P(m)$ centered on $m = 0$ [49].

In the case of an orientated substate population, the probability of a γ

ray being emitted at an angle, θ relative to the beam direction is given by

$$W(\theta) = 1 + A_2 P_2(\cos\,\theta) + A_4 P_4(\cos\,\theta), \tag{4.11}$$

where $P_{2,4}$ cosθ are the Legendre polynomials and $A_{2,4}$ are known as angular distribution coefficients. The angular distribution coefficients depend on the multipolarity of the γ-ray transitions, the spins of the initial and final states and the population distribution of the magnetic substates, $P(m)$ [49]. Fitting a function of the form in Equation 4.11 to experimental data provides a method of extracting the multpolarity of a γ ray independently from all other γ rays.

In this work it was not possible to measure directly the angular distributions for γ-ray transitions due to the high density of γ-ray photopeaks detected in the Gammasphere array. In order to isolate the photopeaks of interest γ ray coincidence gates had to used. The angular distribution of the γ ray being measured is dependent on the multipolarity of the γ ray on which the coincidence gate was set. The angular correlation between the coincident γ rays must now be considered.

The angular correlation between the two coincident γ rays is best described by the directional correlation of orientated states (DCO) ratio. Figure 4.3 illustrates the decay of two coincident γ rays emitted at different angles, θ_1 and θ_2 relative to the beam direction. The angle ϕ is the angle between the planes defined by θ_1 and θ_2 and the beam axis. The DCO ratio is calculated from experimental data by

$$R_{DCO} = \frac{I^{\gamma 2}_{\theta_1}(Gate^{\gamma 1}_{\theta_2})}{I^{\gamma 2}_{\theta_2}(Gate^{\gamma 1}_{\theta_1})}, \tag{4.12}$$

where $I^{\gamma 2}_{\theta_1}(Gate^{\gamma 1}_{\theta_2})$ is the intensity of γ_2 measured at angle θ_1, when a gate

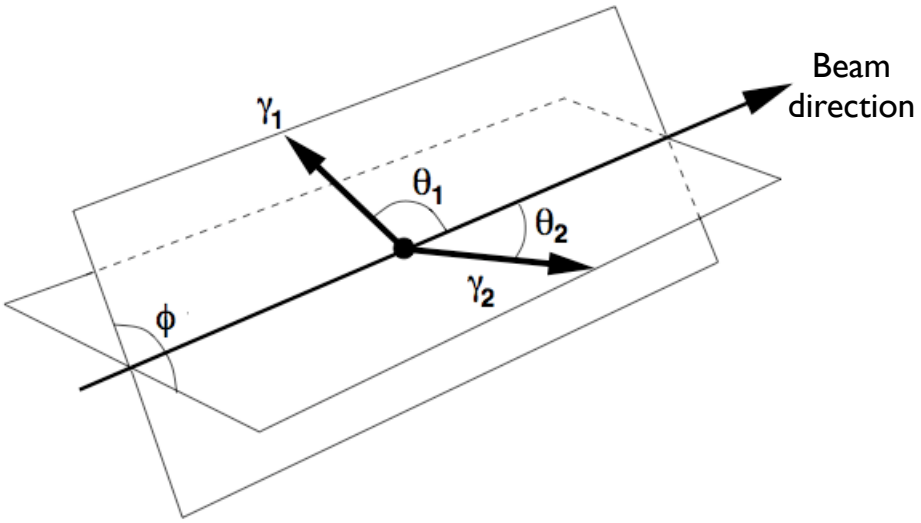

Figure 4.3: Geometry of the γ rays used in DCO ratios.

is placed in γ_1 at an angle θ_2. Similarly, $I^{\gamma 2}_{\theta_2}(Gate^{\gamma_1}_{\theta_1})$ is the intensity of γ_2 measured at angle θ_2, when a gate is placed in γ_1 at an angle θ_1. DCO ratios are discussed in detail in Refs. [50, 51].

To determine the multipolarity for a unknown transition from the DCO ratio the multipolarity must be known for the coincident γ ray. Only transitions of quadrupole and dipole nature are considered. $\Delta I = 2$ transitions are assumed to be stretched electric quadrupole, ($E2$) transitions. Magnetic quadrupole, ($M2$) transitions are not considered as they would be significantly hindered (see Section 2.5) and would produce long-lived states. $\Delta I = 1$ transitions can be electric or magnetic dipole in nature ($E1$ and $M1$, respectively) or mixed $M1/E2$. The ratio of $M1$ to $E2$ transition strength is defined by the mixing ratio, δ.

The value of the DCO ratio of two coincident γ rays is sensitive to the values of θ_1, θ_2 and ϕ. The DCO ratio between two transitions of the same multipolarity should be unity, ie. for two stretched-quadrupole or two stretched-

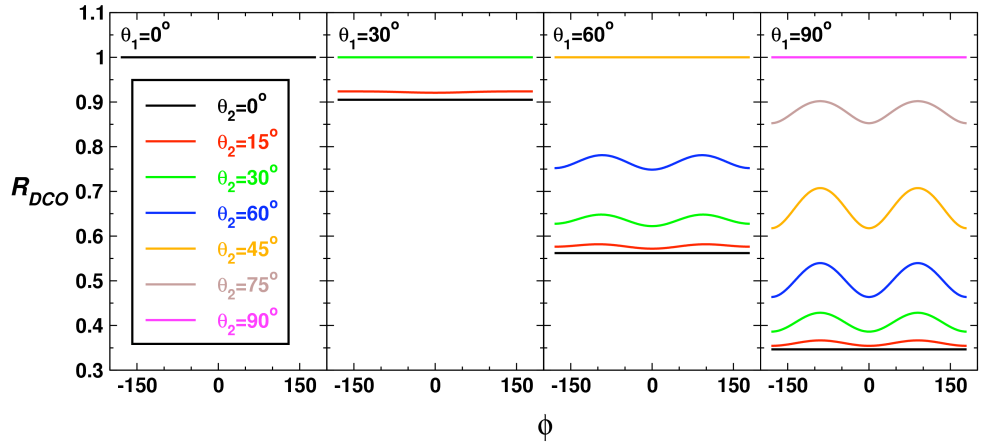

Figure 4.4: [Colour] The calculated DCO ratios for a stretched (I =10→I =8) E2 and a pure stretched (I =8→I =7) M1, for different combinations of θ_1, θ_2 and ϕ. A full alignment of angular momentum was assumed.

dipole transitions. Detectors are selected to give the DCO ratio for an $E2$ and a pure $M1$ γ rays with the largest difference to unity. The theoretical DCO ratios calculated for a stretched (I =10→I =8) $E2$ and a pure stretched (I =8→I =7) $M1$, with several combinations of θ_1, θ_2 and ϕ, are shown in Fig. 4.4. From these calculations, the ideal positions for the detectors used in DCO ratio measurements are determined to be $\theta_1 = 90°$ and $\theta_2 = 0°$, respectively, for all values of ϕ. Since the detectors used in this study were not sensitive to polarisation, detectors at 180° can also be used for θ_2.

To increase the statistics in the spectra used to calculate the DCO ratios, several rings of detectors were used. Details of the detector rings for the Gammasphere array are given in Table 3.1. The rings positioned around $\theta_1 = 90°$, with the range $79° \leq \theta_1 \leq 101°$ (ring numbers 7-11), and the rings positioned closest to $\theta_2 = 0°$ at $\theta_2 = 32°$ and 38° (ring numbers 2 and 3), and $\theta_2 = 180°$ at $\theta_2 = 148°$ and 163° (ring numbers 16 and 17), were used to calculate DCO ratios in this work. It is reasonable to assume that

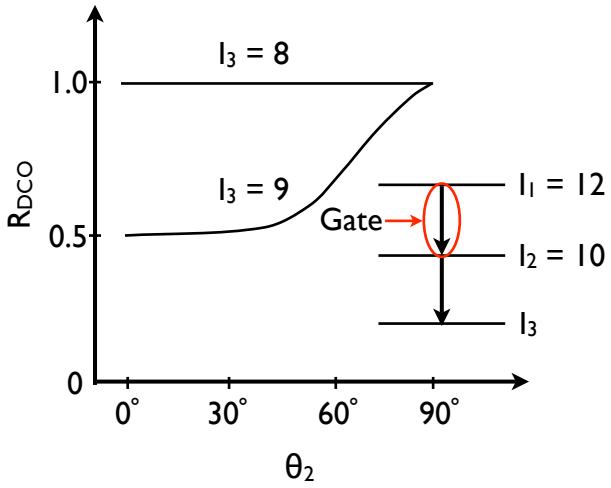

Figure 4.5: [Colour] Plot of the dependence of the R_{DCO} on the angle of θ_2 with $\theta_1 = 90°$,adapted from Ref. [50]. Pure multipole orders of $L = I_i - I_f$ have been assumed.

the range of θ between the different rings used will have have little effect on the measured DCO ratios. Figure 4.5 shows the effect on the calculated DCO ratios for pure stretched quadrupole and pure stretched dipole transitions, gated on a stretched quadrupole transition, when θ_2 is varied. A variation of 40° has little effect on the measured DCO ratio. The angle ϕ will vary depending on which detectors within the rings are used for each coincident event. The DCO ratio oscillates with the angle ϕ (see Fig. 4.4) and will average out over the total combinations of detectors.

The matrices used to measure DCO ratios were non-symmetric $\gamma\gamma$ matrices with γ rays detected in the Gammasphere rings 7-11 on one axis and coincident γ detected in the Gammasphere rings 2, 3, 16 and 17 on the other axis (see Table 3.1). Only those γ rays detected within 12 ns of the fusion reaction are included in the matrix. Those emitted after this time are considered to be fully stopped in the backing material and have lost angular momentum alignment. To measure DCO ratios for weakly populated transi-

tions an additional γ-ray coincidence condition was specified in the sort code to isolate further the photopeaks. No angular restraints were applied to the detection of this γ ray.

Typical values for DCO ratios for dipole and quadrupole transitions, when a gate is set on a quadrupole transition, are 1 and 0.5-0.6, respectively. If the gates are swapped the DCO ratio will be inverted. The degree of alignment of the angular momentum varies from experiment to experiment effecting the measured DCO ratios. The DCO ratios are calculated for pairs of transitions were the multipolarities of both γ rays are known. These measured ratios form the basis for comparison to ratios of transitions with unknown multipolarities. The mixing ratio δ will also effect the DCO ratio measured for dipole transitions, with strongly mixed transitions producing DCO ratios of 0.7-0.8.

4.4.2 Internal conversion

Internal conversion occurs when the electromagnetic multipole fields of a nucleus interact with the atomic electrons and cause the emission of one electron from the atom. This process competes with the emission of γ rays from nuclear states and the total decay probability of a state is given by

$$\lambda_T = \lambda_\gamma + \lambda_e, \tag{4.13}$$

where λ_γ is the decay probability of γ-ray emission and λ_e is the probability of internal conversion [52]. The probability of internal conversion occurring relative to γ-ray emission is defined by the internal conversion coefficient, α, where

$$\alpha = \frac{\lambda_e}{\lambda_\gamma}. \tag{4.14}$$

The internal conversion coefficient is dependent on the atomic number of the nucleus and the energy and multipolarity of the transition. For low-energy transitions the internal conversion coefficient is significantly large such that it can be measured and used as a tool to determine the multipolarity of a transition. The total intensity flowing into a state must equal that flowing out, however only the γ-ray intensity is measured from γ-ray spectra. The total intensity of a transition can be calculated by

$$I_T = I_\gamma(1 + \alpha), \tag{4.15}$$

if the multipolarity and therefore α are known. For the case that the multipolarities of all but one of the transitions decaying into or out of a state are known, the multipolarity of the unknown transition can be inferred from the internal conversion coefficient that best fits the intensity flow. This measurement is independent of nuclear alignment making it ideal for the measurement of the multipolarity of transitions decaying from isomeric states.

4.4.3 Branching ratios and g factors

The experimental in-band branching ratios can be used support the assignment of multi-quasiparticle configurations. In the rotational model, the mixing ratio of a $M1$/E2 dipole transition is given by

$$\frac{\delta^2}{1+\delta^2} = \frac{2K^2(2I-1)}{(I+1)(I-1+K)(I-1-K)} \left(\frac{E_1}{E_2}\right)^5 \frac{I_2}{I_1}, \tag{4.16}$$

where E_1 and E_2 are the dipole and quadrupole energies in MeV and I_1 and I_2 are the intensities measured for these transitions, respectively, K is the

projection of the angular momentum onto the symmetry axis and I is the spin. The magnitude of the quantity $\frac{g_K - g_R}{Q_0}$ is then given by

$$\left|\frac{g_K - g_R}{Q_0}\right| = \frac{0.93E_1}{(\sqrt{I^2-1})\delta}, \tag{4.17}$$

where Q_0 is the intrinsic quadrupole moment and g_K and g_R are the intrinsic and collective g factors, respectively. The sign of $\frac{g_K - g_R}{Q_0}$ can be determined by

$$\mathrm{sgn}(\delta) = \mathrm{sgn}\Big(\frac{g_K - g_R}{Q_0}\Big), \tag{4.18}$$

when the angular distributions coefficient, A_2 is measured and the sign of δ is inferred [53]. Since these measurements were not possible in the current work, the signs of the measured $\frac{g_K - g_R}{Q_0}$ values remain ambiguous.

The experimentally calculated values for $|\frac{g_K - g_R}{Q_0}|$ are then compared to the theoretical $|\frac{g_K - g_R}{Q_0}|$ ratios, calculated for the possible multi-quasiparticle configurations. g_k can be approximated using the expression

$$Kg_K = \sum \Omega g_\Omega = \sum \Lambda g_\Lambda + \sum \Sigma g_\Sigma, \tag{4.19}$$

where Λ and Σ are the asymptotic Nilsson quantum numbers for the orbital and intrinsic angular momenta projections on to the symmetry axis, respectively. The corresponding g factors, g_Λ and g_Σ, are given by

$$g_\Lambda = \begin{cases} 0 & \text{neutrons} \\ 1 & \text{protons} \end{cases} \tag{4.20}$$

and

$$g_\Sigma = 0.06 \begin{cases} -3.83 & \text{neutrons} \\ +5.59 & \text{protons,} \end{cases} \tag{4.21}$$

The single particle g factors, g_Σ are multiplied by a quenching factor, 0.06 to account for the fact that they exist in a nuclear medium and are not free particles [54]. For neutrons in Nilsson orbitals derived from the $i_{13/2}$ orbital

a value of g_Σ=0.08 was used. This value was taken from empirical data for similar bands in the region. Values of g_R=0.3 and Q_0=6.0 eb were used, in keeping with the systematics of the region [55].

Chapter 5

Spectroscopy of ^{180}Os

The large number of transitions investigated in this work are presented across several sections in this chapter. For clarity the level scheme for ^{180}Os has been split into several partial level schemes. The prompt spectroscopy of ^{180}Os is presented in Section 5.1 and the associated transitions are shown in Partial Level Scheme A. The prompt-delayed spectroscopy and half-life measurement of the $K^{\pi}=7^{-}$, 1929-keV isomer is presented in Section 5.2 and the γ-ray transitions are shown in Partial Level Scheme B. Finally, the prompt-delayed spectroscopy and half-life measurements for the newly discovered 5848-keV and 7592-keV isomers are presented in Section 5.3 with the corresponding delayed and prompt transitions shown in Partial Level Schemes C and D, respectively.

5.1 Prompt spectroscopy of ^{180}Os

Previous studies of the prompt structure of ^{180}Os have identified several side bands in addition to the *yrast* and *yrare* bands up to spins of $I = 30\ \hbar$ [56–62].

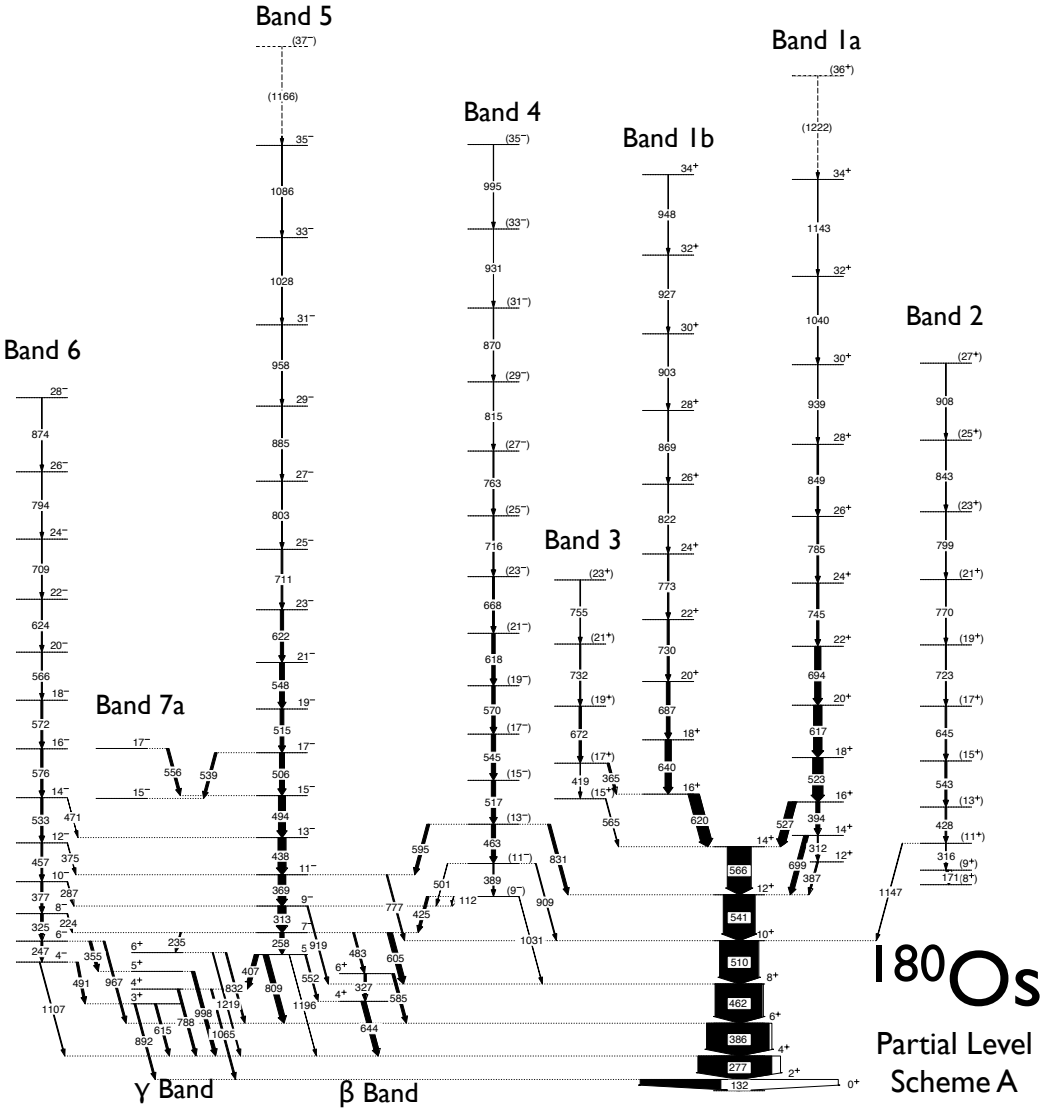

Figure 5.1: Partial Level Scheme A: Prompt transitions in ^{180}Os. Transition energies are given to the nearest keV. Intensities are proportional to the widths of the arrows and the white sections represent the calculated internal conversion. Tentative assignments are denoted with a dashed arrow and tentative spin and parity assignments are give in brackets.

The most recent study of the prompt band structure of ^{180}Os was performed by *Lieder et al.* [63]. The study used the same heavy-ion fusion-evaportaion reaction conditions described in Section 3.1.1 with the *OSIRIS* and *GASP* γ-ray spectrometers at the Hahn Meitner Institute, Berlin and the Laboratori Nazionali di Legnaro, respectively. The results presented in *Lieder et al.* [63] extended the prompt level scheme to include ten rotational bands up to spins of I= 35 $\hbar$ and will be used as the main source of comparison for the prompt level scheme produced in this thesis.

In the present work, extensive coincidence analysis of prompt $\gamma\gamma\gamma$ cubes and prompt $\gamma\gamma\gamma\gamma$ hypercubes for both the thick- and thin-target data sets produced Partial Level Scheme A for ^{180}Os, shown in Fig. 5.1. Partial Level Scheme A contains six of the ten prompt rotational bands produced in this work and the corresponding inter-band transitions. The additional four prompt rotational bands that decay via the 1929-keV, K^{π}=7^{-} isomer are shown separately in Partial Level Scheme B and discussed in Section 5.2. The relative intensities of the transitions in Partial Level Scheme A were measured in the thin-target $\gamma\gamma\gamma$ cube and are listed in Table 5.1 along with the measured energies for the transitions and measured DCO ratios, where possible. This study established a new band, labelled as Band 3 in Fig. 5.1, and extended several of the previously established rotational bands to higher spins. In the following sections coincidence spectra for each band and pertinent information will be presented.

5.1.1 DCO ratios

The spin assignments for the levels presented in this work are based on a combination of DCO ratios and the systematics of the decays observed. DCO

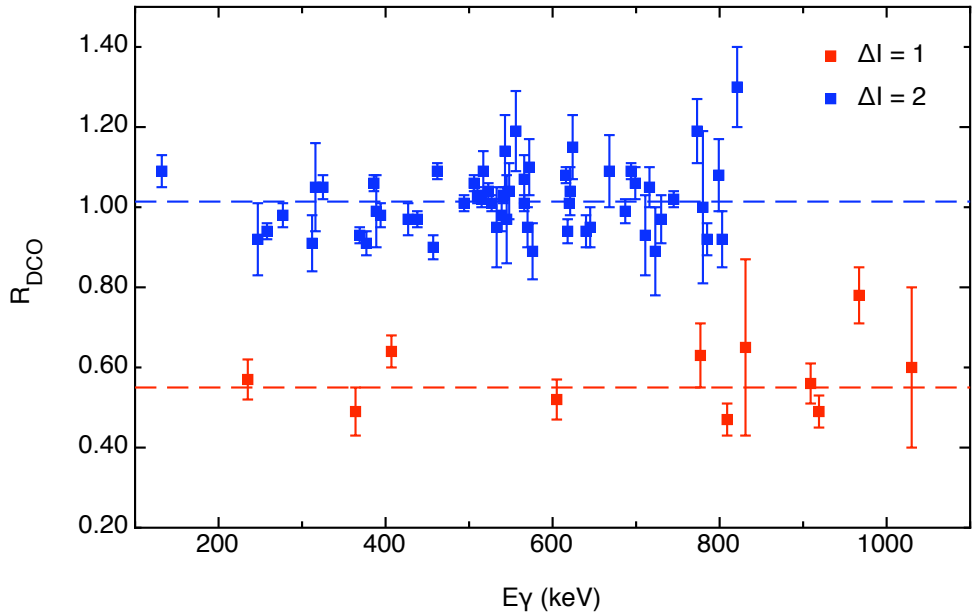

Figure 5.2: [Colour] Measured DCO ratios for ΔI=1 and ΔI=2 transitions in Partial Level Scheme A. The dashed lines at 0.55 and 1.014 represent the weighted-average values for the DCO ratios of the ΔI=1 and ΔI=2 transitions, respectively when gated on a stretched ΔI=2 transition.

ratios were measured (see Section 4.4.1) for transitions with established multipolarities and used as the basis for the assignment of multipolarities to other transitions. Figure 5.2 shows the DCO ratios measured for the established pure dipole $\Delta I = 1$ and quadrupole $\Delta I = 2$ transitions in Partial Level Scheme A, when gated on the a stretched ΔI=2 transition. The difference between $\Delta I = 1$ and $\Delta I = 2$ transitions is evident in weighted average DCO ratios of 0.55 ± 0.02 and 1.014 ± 0.004, respectively.

Table 5.1: γ-ray energies and intensities, initial and final spins and DCO ratios for transitions in Partial Level Scheme A. The intensities are normalised to the strongest transition and corrected for detector efficiency.

E_γ	$J_i^\pi \rightarrow J_f^\pi$	I_γ	R_{DCO}
Ground-State Band			
132.3(1)	$2^+ \rightarrow 0^+$	100.0(3)	1.09(4)
276.5(1)	$4^+ \rightarrow 2^+$	92.0(3)	0.98(3)
386.3(1)	$6^+ \rightarrow 4^+$	77.5(24)	1.06(2)
462.4(1)	$8^+ \rightarrow 6^+$	58.2(18)	1.09(2)
510.3(1)	$10^+ \rightarrow 8^+$	47.6(15)	1.03(2)
541.1(1)	$12^+ \rightarrow 10^+$	38.8(12)	1.03(2)
566.3(1)	$14^+ \rightarrow 12^+$	29.1(9)	1.01(2)
Band 1a			
387.5(9)	$12^+ \rightarrow 12^+$	1.7(3)	
311.9(8)	$14^+ \rightarrow 12^+$	1.2(2)	0.91(7)
699.2(1)	$14^+ \rightarrow 12^+$	5.8(2)	1.06(4)
394.3(1)	$16^+ \rightarrow 14^+$	4.8(7)	0.98(3)
527.4(1)	$16^+ \rightarrow 14^+$	9.9(3)	1.01(2)
523.4(1)	$18^+ \rightarrow 16^+$	12.5(4)	1.04(2)
616.8(1)	$20^+ \rightarrow 18^+$	10.3(4)	1.08(2)
694.1(1)	$22^+ \rightarrow 20^+$	7.7(3)	1.09(2)
745.1(5)	$24^+ \rightarrow 22^+$	2.8(2)	1.02(2)
785.4(5)	$26^+ \rightarrow 24^+$	2.2(2)	0.92(4)
849.4(8)	$28^+ \rightarrow 26^+$	1.9(2)	
939.3(8)	$30^+ \rightarrow 28^+$	0.3(1)	
1040.0(1)	$32^+ \rightarrow 30^+$	0.8(1)	
1142.7(2)	$34^+ \rightarrow 32^+$	0.1(1)	
1222.2(2)	$36^+ \rightarrow 34^+$	0.1(1)	
Band 1b			
619.1(1)	$16^+ \rightarrow 14^+$	13.5(5)	1.01(1)

Table 5.1: Continued.

E_γ	$J_i^\pi \rightarrow J_f^\pi$	I_γ	R_{DCO}
640.2(1)	$18^+ \rightarrow 16^+$	7.7(3)	0.94(4)
687.0(1)	$20^+ \rightarrow 18^+$	4.5(2)	0.99(3)
729.8(1)	$22^+ \rightarrow 20^+$	2.6(2)	0.97(6)
773.3(1)	$24^+ \rightarrow 22^+$	1.8(1)	1.19(8)
821.6(1)	$26^+ \rightarrow 24^+$	0.9(1)	1.3(1)
869.4(1)	$28^+ \rightarrow 26^+$	0.9(1)	
903.4(1)	$30^+ \rightarrow 28^+$	0.6(1)	
927.5(1)	$32^+ \rightarrow 30^+$	0.3(1)	
948.4(1)	$34^+ \rightarrow 32^+$	0.4(1)	
	Band 2		
171.0(1)	$(9^+) \rightarrow (8^+)$	3.2(3)	1.8(6)
316.4(1)	$(11^+) \rightarrow (9^+)$	0.6(1)	1.1(1)
1147.4(1)	$(11^+) \rightarrow 10^+$	0.7(1)	0.4(2)
427.6(1)	$(13^+) \rightarrow (11^+)$	2,0(2)	0.97(4)
543.1(2)	$(15^+) \rightarrow (13^+)$	2.5(2)	1.14(9)
645.0(1)	$(17^+) \rightarrow (15^+)$	2.0(2)	0.95(5)
722.8(1)	$(19^+) \rightarrow (17^+)$	1.2(1)	0.89(11)
769.8(1)	$(21^+) \rightarrow (19^+)$	0.8(1)	1.00(19)
799.3(1)	$(23^+) \rightarrow (21^+)$	0.5(1)	1.08(9)
843.5(2)	$(25^+) \rightarrow (23^+)$	0.9(1)	
907.6(2)	$(27^+) \rightarrow (25^+)$	0.2(8)	
	Band 3		
565.2(3)	$(15^+) \rightarrow (14^+)$	0.90(2)	contaminated
418.8(1)	$(17^+) \rightarrow 15^+$	0.4(2)	1.0(2)
364.5(1)	$(17^+) \rightarrow 16^+$	2.4(2)	0.49(6)
671.9(1)	$(19^+) \rightarrow (17^+)$	2.9(2)	0.88(7)
732.5(1)	$(21^+) \rightarrow (19^+)$	1.5(2)	
755.4(1)	$(23^+) \rightarrow (21^+)$	0.8(2)	

Table 5.1: Continued.

E_γ	$J_i^\pi \rightarrow J_f^\pi$	I_γ	R_{DCO}
	Band 4		
112.2(1)	$(9^-) \rightarrow 9^-$	0.6(1)	
425.4(1)	$(9^-) \rightarrow 7^-$	3.2(3)	
1030.9(3)	$(9^-) \rightarrow 8^+$	0.5(2)	0.6(2)
388.9(2)	$(11^+) \rightarrow (9^-)$	1.4(2)	0.99(9)
501.1(3)	$(11^+) \rightarrow 9^-$	0.5(1)	
909.4(2)	$(11^+) \rightarrow 10^+$	1.2(2)	0.56(5)
462.9(1)	$(13^+) \rightarrow (11^+)$	5.1(4)	contaminated
595.2(1)	$(13^+) \rightarrow 11^-$	3.6(2)	
831.3(9)	$(13^+) \rightarrow 12^+$	3.7(3)	0.65(22)
516.9(1)	$(15^-) \rightarrow (13^+)$	5.2(3)	1.09(5)
544.8(1)	$(17^-) \rightarrow (15^-)$	5.2(2)	0.97(11)
570.4(1)	$(19^-) \rightarrow (17^-)$	4.1(2)	0.95(5)
617.6(1)	$(21^-) \rightarrow (19^-)$	4.2(2)	0.94(3)
668.2(1)	$(23^-) \rightarrow (21^-)$	2.3(1)	1.09(9)
716.4(1)	$(25^-) \rightarrow (23^-)$	1.5(1)	1.05(5)
763.4(1)	$(27^-) \rightarrow (25^-)$	1.3(1)	
815.4(11)	$(29^-) \rightarrow (27^-)$	0.6(1)	
870.1(1)	$(31^-) \rightarrow (29^-)$	0.6(1)	
931.4(2)	$(33^-) \rightarrow (31^-)$	0.2(1)	
995.4(1)	$(35^-) \rightarrow (33^-)$	0.4(1)	
	Band 5		
407.3(1)	$5^- \rightarrow 4^+$	5.5(3)	0.64(4)
551.7(2)	$5^- \rightarrow 4^+$	1.7(2)	
809.5(1)	$5^- \rightarrow 6^+$	6.5(4)	0.47(4)
1195.7(9)	$5^- \rightarrow 4^+$	0.4(1)	
235.4(10)	$7^- \rightarrow 6^+$	1.5(1)	0.57(5)
258.4(1)	$7^- \rightarrow 5^-$	4.6(2)	0.94(2)

Table 5.1: Continued.

E_γ	$J_i^\pi \rightarrow J_f^\pi$	I_γ	R_{DCO}
483.2(1)	$7^- \rightarrow 6^+$	2.6(2)	
605.5(1)	$7^- \rightarrow 8^+$	6.5(3)	0.52(5)
313.2(1)	$9^- \rightarrow 7^-$	9.4(4)	1.03(2)
918.7(1)	$9^- \rightarrow 8^+$	1.5(1)	0.49(4)
368.8(1)	$11^- \rightarrow 9^-$	9.1(3)	0.93(2)
777.2(1)	$11^- \rightarrow 10^+$	1.7(1)	0.63(8)
437.8(1)	$13^- \rightarrow 11^-$	9.6(3)	0.97(2)
494.4(1)	$15^- \rightarrow 13^-$	8.5(3)	1.01(2)
505.7(1)	$17^- \rightarrow 15^-$	6.1(2)	1.06(2)
539.0(10)	$17^- \rightarrow 15^-$	3.2(3)	0.98(4)
515.2(1)	$19^- \rightarrow 17^-$	4.5(2)	1.02(2)
548.2(1)	$21^- \rightarrow 19^-$	5.9(2)	1.04(7)
621.7(1)	$23^- \rightarrow 21^-$	4.0(2)	1.04(6)
711.4(1)	$25^- \rightarrow 23^-$	2.1(1)	0.93(10)
803.0(1)	$27^- \rightarrow 25^-$	1.2(1)	0.92(7)
885.0(1)	$29^- \rightarrow 27^-$	0.6(1)	
957.9(1)	$31^- \rightarrow 29^-$	0.5(1)	
1028.2(2)	$33^- \rightarrow 31^-$	0.1(1)	
1086.2(7)	$35^- \rightarrow 33^-$	0.1(1)	
1166.0(12)	$37^- \rightarrow 35^-$	0.1(1)	
555.6(10)	$17^- \rightarrow 15^-$	3.2(3)	1.19(10)
	Band 6		
491.5(1)	$4^- \rightarrow 3^+$	2.8(3)	
1106.7(1)	$4^- \rightarrow 4^+$	1.01(19)	
246.7(1)	$6^- \rightarrow 4^-$	2.02(11)	0.92(9)
967.1(1)	$6^- \rightarrow 6^+$	2.39(24)	0.78(7)
355.2(2)	$6^- \rightarrow 5^+$	2.56(18)	
223.9(2)	$8^- \rightarrow 7^-$	0.62(8)	

Table 5.1: Continued.

E_γ	$J_i^\pi \rightarrow J_f^\pi$	I_γ	R_{DCO}
324.7(1)	$8^- \rightarrow 6^-$	2.89(19)	1.05(3)
287.5(2)	$10^- \rightarrow 9^-$	0.61(7)	
376.8(1)	$10^- \rightarrow 8^-$	2.53(16)	0.91(3)
375.5(2)	$12^- \rightarrow 11^-$	0.51(7)	
456.9(1)	$12^- \rightarrow 10^-$	2.21(14)	0.90(3)
470.6(7)	$14^- \rightarrow 13^-$	0.10(6)	
532.9(1)	$14^- \rightarrow 12^-$	2.74(16)	0.95(10)
575.6(1)	$16^- \rightarrow 14^-$	2.78(16)	0.89(7)
572.4(1)	$18^- \rightarrow 16^-$	2.39(14)	1.10(7)
566.4(1)	$20^- \rightarrow 18^-$	1.35(14)	1.07(6)
623.6(1)	$22^- \rightarrow 20^-$	1.32(12)	1.15(8)
708.7(1)	$24^- \rightarrow 22^-$	1.00(10)	
793.5(1)	$26^- \rightarrow 24^-$	0.53(9)	
873.6(1)	$28^- \rightarrow 26^-$	0.41(9)	
	β Band		
644.0(1)	$4^+ \rightarrow 4^+$	5.9(5)	
327.0(1)	$6^+ \rightarrow 4^+$	2.6(2)	
584.7(1)	$6^+ \rightarrow 6^+$	3.2(3)	
	γ Band		
615.2(1)	$3^+ \rightarrow 4^+$	2.5(5)	
891.7(1)	$3^+ \rightarrow 2^+$	2.2(8)	
788.4(1)	$4^+ \rightarrow 4^+$	2.8(4)	
1064.9(1)	$4^+ \rightarrow 2^+$	2.0(3)	
998.3(10)	$5^+ \rightarrow 4^+$	2.0(3)	
832.5(1)	$6^+ \rightarrow 6^+$	1.9(3)	
1218.8(1)	$6^+ \rightarrow 4^+$	1.3(2)	

5.1.2 Bands 1a and 1b

The spin of Band 1a has been the focus of much speculation and is the basis of the assignment of the *yrast* and *yrare* bands between bands 1a and 1b. In Refs. [60, 62], the level decaying via the 527-keV and 394-keV transitions in Band 1a is assigned a spin of $I = 14\ \hbar$ in contrast to the spin of $I = 16\ \hbar$ assigned in Refs. [56, 63] and this study. The former was based on the observation of several inter-band transitions of 1051, 1093 and 1240 keV, which were not observed in this work. The latter assignment in Refs. [56, 63] was based on a combination of the DCO ratio, electron conversion-coefficient measurement and angular-distribution measurement of the 527-keV transition alone. The DCO ratios for the 527-, 699-, 312- and 394-keV transitions were measured in this work and are given in Table 5.1. All of these measurements firmly indicate stretched-quadrupole transitions ($\Delta I = 2$) and support the assignment of spin $I = 16\ \hbar$ for this level.

The transitions belonging to Band 1a are shown in the spectrum in panel (a) of Fig. 5.3 which was produced by the sum of triple gates, ($0^+ \rightarrow 22^+$) /($22^+ \rightarrow 32^+$)/($22^+ \rightarrow 32^+$), in the thin-target $\gamma\gamma\gamma\gamma$ hypercube. A 1143-keV transition from the 34^+ level, tentatively assigned in Ref. [63], is clearly resolvable in this spectrum and was confirmed as the extension of the band to the 34^+ level. The 1222-keV γ ray was also established as a strong candidate for the next transition in this band and was identified in the sum of double gates ($22^+ \rightarrow 34^+$)/($22^+ \rightarrow 34^+$) in the thin-target $\gamma\gamma\gamma$ cube, shown in the inset of Fig. 5.3 (a).

Figure 5.3(b) shows the spectrum containing the transitions associated with Band 1b and was produced by the sum of triple gates, ($0^+ \rightarrow 22^+$)/ ($22^+ \rightarrow 34^+$)/($22^+ \rightarrow 34^+$), in the thin-target $\gamma\gamma\gamma\gamma$ hypercube. This band was

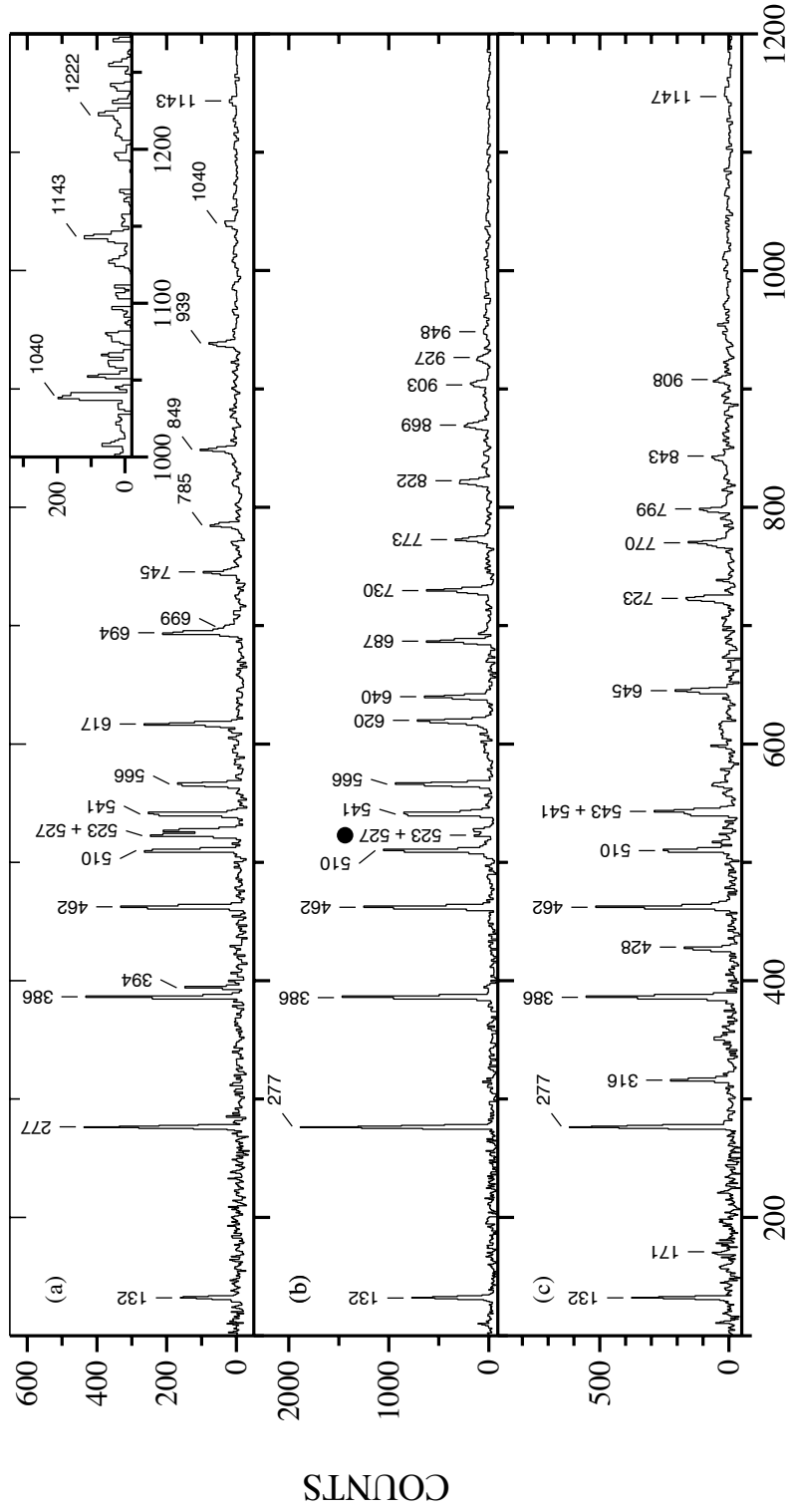

Figure 5.3: Spectra showing transitions in Partial Level Scheme A produced by a sum of triple gates in the thin-target $\gamma\gamma\gamma\gamma$ hypercube. (a) Band 1a, $(0^+ \rightarrow 22^+)/(22^+ \rightarrow 34^+)/(22^+ \rightarrow 34^+)$ (b)Band 1b, $(0^+ \rightarrow 22^+)/(22^+ \rightarrow 32^+)/(22^+ \rightarrow 32^+)$. The solid circle indicates the linking transitions to Band 1a. (c) Band 2, $(0^+ \rightarrow 13^+)/(13^+ \rightarrow 27^+)/(13^+ \rightarrow 27^+)$.

extended to the 34^+ level by a 948-keV transition established in this work. The 523- and 527-keV γ rays from Band 1a are also seen in this spectrum (labelled with a solid circle) indicating some unobserved linking transitions between the two bands.

5.1.3 Band 2

The spectrum in Panel (c) of Fig. 5.3 shows the transitions attributed to Band 2. It was produced by the sum of triple coincidence gates, $(0^+\rightarrow13^+)$/ $(13^+\rightarrow27^+)$/ $(13^+\rightarrow27^+)$, in the thin-target $\gamma\gamma\gamma\gamma$ hypercube and confirms the band structure presented in Ref. [63]. Although it was not possible to extend this band to higher spins in this study, additional information about the spin assignment for the band-head level, and subsequently for the entire band, was obtained.

The 1147-keV transition from Band 2 to the 10^+ level of the ground-state band is clearly identifiable in the spectrum and provides the basis for the spin assignment for the band head. The DCO ratio for the 1147-keV transition was measured for the first time in this work as 0.4 $\pm$ 0.2 and indicates a dipole transition ($\Delta I = 1$). The level decaying via this transition is therefore constrained to have a spin of either $I = 9$ or 11 $\hbar$. The spin $I = 11$ $\hbar$ was tentatively assigned to the level based on the absence of any transitions to the 8^+ level of the ground-state band, as may be expected if the level had spin $I = 9$ $\hbar$

The DCO ratio of the 316-keV transition from the $I^\pi = (11^+)$ level was measured to be 1.1 $\pm$ 0.1 indicating an $\Delta I = 2$ ($E2$) transition to an $I^\pi = (9^+)$ level. This experiment also provided the first measurement of the DCO ratio of the 171-keV transition from the (9^+) level. The DCO ratio

was measured as 1.8 ± 0.6 indicating an $E2$ transition ($\Delta I = 2$). However, a $\Delta I = 1$ transition cannot be ruled out and a spin of ($I^{\pi} = 8^{+}$) is tentatively assigned for the band-head level for this band, based on the configuration assigned to the band (see Section 6.4.3).

The parity of Band 2 could not be measured directly within the confines of this experiment but is tentatively assigned as positive, solely due to the decay into the positive parity ground-state band. Band 2 has been assigned a $\nu(i_{13/2})^2$ configuration which would result in a positive parity band.

5.1.4 Band 3

Band 3 was newly identified in this study, perhaps being overlooked in previous studies due to the similarity in energies of the 565-keV transition connecting Band 3 to the 14^{+} level of the ground-state band, and the 566-keV transition decaying from this level within the ground-state band. The spectrum containing the transitions associated with Band 3 is shown in panel (a) of Fig. 5.4. This spectrum is a result of the sum of double gates of all transitions in Band 3 ($15^{+} \rightarrow 23^{+}$) and the 566-keV γ ray in the ground-state band, within the thick-target $\gamma\gamma\gamma$ cube. A 565-keV γ ray remains visible in this spectrum despite the gate on the 566-keV γ ray, indicating the presence of a 565-keV transition in relation to this band. This was confirmed in the coincidence spectrum produced by the double gate on the 566-keV and 565-keV γ rays, shown in Fig. 5.4 (b). The 419- 672- and 732-keV transitions assigned to Band 3 are clearly seen in this spectrum. A transition is also seen at 755 keV and was tentatively assigned as an extension to this band.

The spin assignment of Band 3 is based on the DCO ratio for the 365-keV γ ray connecting Band 3 to the 16^{+} level of Band 1a. The DCO ratio was

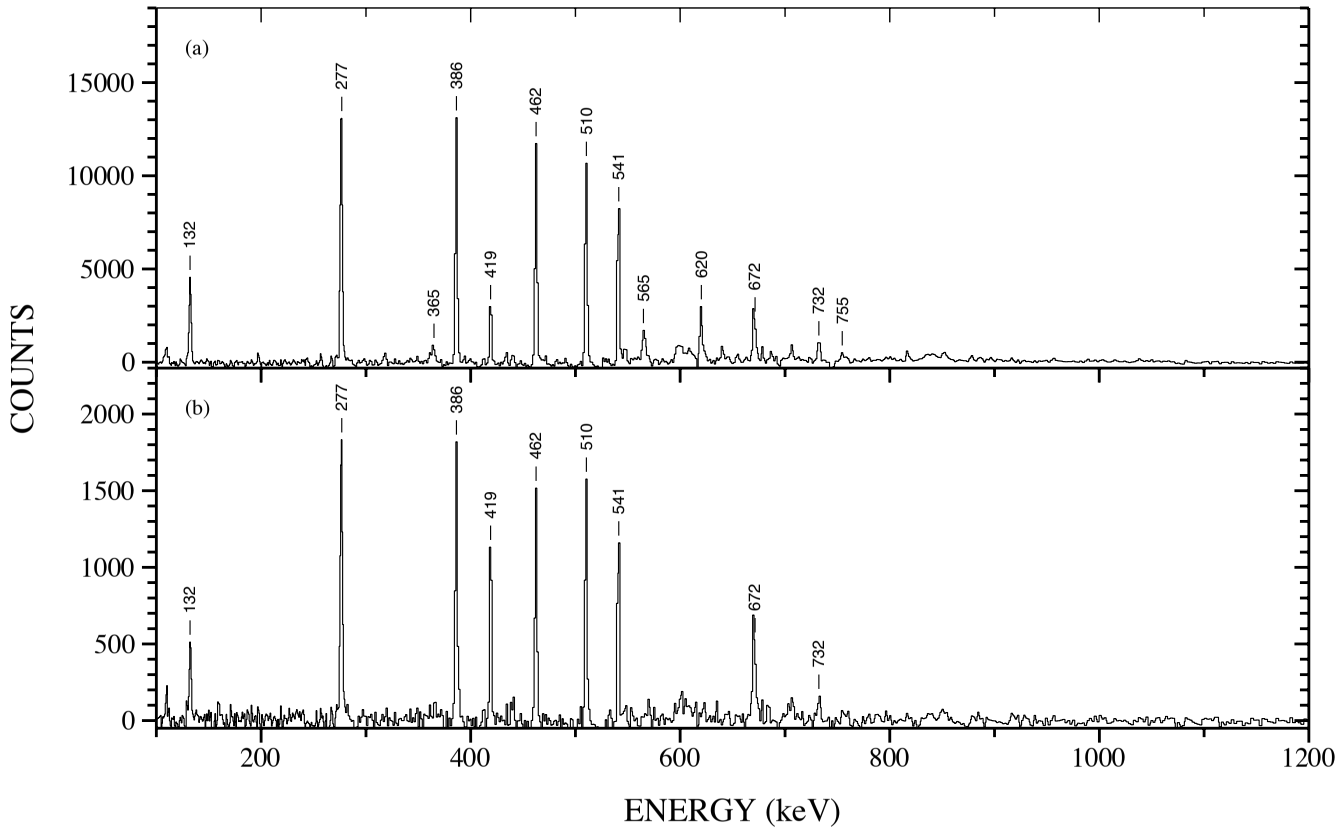

Figure 5.4: Spectra showing the γ-ray transitions associated with Band 3. (a) A spectrum produced by the sum of double gates (566-keV)/($15^- \rightarrow 23^-$) in the thick-target $\gamma\gamma\gamma$ cube. (b) A spectrum produced by the double gate (566-keV)/(565-keV) in the thick-target $\gamma\gamma\gamma$ cube.

measured as 0.49 ± 0.06 strongly suggesting a dipole transition ($\Delta I = 1$). The ordering of the 565-keV and the 419-keV transitions is ambiguous and has been tentatively assigned to have the 419-keV transition decaying from the 17^+ level to the 15^+ band head of Band 3. This was based on the intensities and the DCO ratio for the 419-keV transition, which was measured as 1.0 ± 0.2, suggesting an electric quadrupole transition ($\Delta I = 2$) and therefore a likely extension of the rotational band to lower spin. It was not possible to confirm a dipole nature for the 565-keV γ ray, as would be expected from this level scheme, due to contamination from the strong 566-keV ground-state band transition.

The parity of this band was tentatively assigned as positive due to the decays to the ground-state band and the 4-quasiparticle configuration assigned to the band (see Section 6.4.4).

5.1.5 Band 4

The transitions belonging to Band 4 are shown in the γ-ray spectrum displayed in Fig. 5.5(a), along with the transitions from Band 4 to the ground-state band. This spectrum was produced by the sum of triple gates, $(0^+ \rightarrow 15^-)$/ $(0^+ \rightarrow 15^-)$/ $(15^- \rightarrow 35^-)$, in the thin-target $\gamma\gamma\gamma\gamma$ hypercube. Due to the choice of gates the transitions to Band 5 and the low-lying states of Band 5 are seen in this spectrum and are labelled by solid diamonds.

The (27^-) to (25^-) transition in Band 4 is confirmed to have an energy of 763 keV, as assigned in Ref. [63], replacing the 758-keV transition previously assigned in Ref. [62]. Additionally, the 995-keV transition, tentatively assigned in Ref. [63], was confirmed as the extension of this band to the (35^-) level. The γ ray is clearly seen in the enlarged section of the γ-ray

coincidence spectrum shown as an inset to Fig. 5.5 (a).

The methodology used to support the spin and parity assignments for Band 4 in this current work closely follows that described in Ref. [63]. The spins and parity of the levels in Band 4 presented in this work are consistent with those in Ref. [63]. The DCO ratios were measured for the 831-, 909- and 1031-keV transitions as 0.65 ± 0.22, 0.56 ± 0.05 and 0.6 ± 0.2, respectively and suggest stretched dipole transitions ($\Delta I = 1$). This leaves $I = 7$ or 9 as possibilities for the spin of the band-head. A spin of $I = 9$ was allocated to the band head state due to the lack of transitions from this state to the $I = 6$ state of the ground-state band, as would be expected for an $I = 7$ assignment.

The parity of Band 4 has been tentatively assigned as negative in agreement with Ref. [63]. If the parity of Band 4 was positive, the 501-keV and 909-keV transitions from the $I = 11$ level in Band 4 would be $M2$ and $E1$ in nature, respectively. As such the 501-keV transition would be hindered by several orders of magnitude compared with the 909-keV γ ray and would not be observed in this experiment. A negative-parity assignment for Band 4 implies that the multipolarities of the 501-keV and 909-keV transitions are $E2$ and $M1$, respectively. This is in much better agreement with the relative intensities measured for these γ rays in this experiment.

5.1.6 Band 5

The transitions assigned to Band 5 are shown in the spectrum in panel (b) of Fig. 5.5. This γ-ray spectrum was produced by the sum of triple gates ($7^- \rightarrow 23^-$)/ ($23^- \rightarrow 35^-$)/ ($23^- \rightarrow 35^-$) in the thin-target $\gamma\gamma\gamma\gamma$ hypercube. The spins and parities presented in Partial Level Scheme A for this

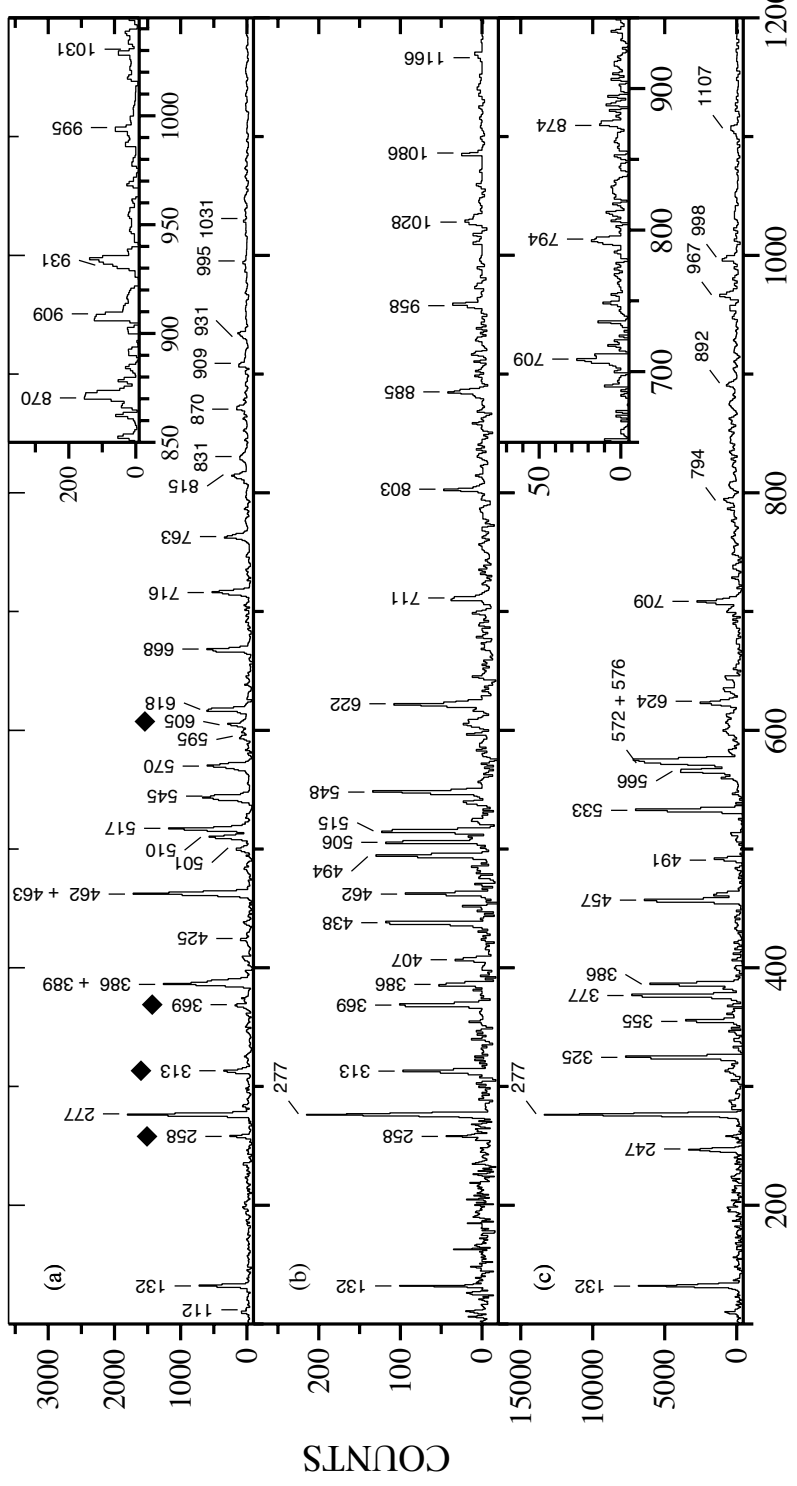

Figure 5.5: Spectra showing transitions in Partial Level Scheme A produced by a sum of triple gates in the thin-target $\gamma\gamma\gamma\gamma$ hypercube. (a) Band 4, $(0^+ \rightarrow 15^-)/\,(0^+ \rightarrow 15^-)/\,(15^- \rightarrow 35^-)$. The solid diamonds indicate the low lying transitions of Band 5. (b) Band 5, $(7^- \rightarrow 23^-)/\,(23^- \rightarrow 35^-)/\,(23^- \rightarrow 35^-)$. (c) Band 6, produced by the sum of double gates $(4^- \rightarrow 26^-)/\,(4^- \rightarrow 26^-)$, in the thin-target $\gamma\gamma\gamma$ cube.

band are taken from those assigned in Ref. [63], based on the measurement of angular-distribution coefficients and internal conversion coefficient for the 809-keV transition in Ref. [62]. The DCO ratios measured in this work, for the 235-, 809- and 605-keV transitions from Band 4 to the β vibrational band and the ground-state band, are given in Table 5.1 and confirm the spin assignment. The parity could not be confirmed in this work and the current assignment is based on that of the previous studies. A 1086-keV transition, observed in this spectrum, was established to extend the band to the I^{π}=35^{-} level. The 1166-keV transition also seen in this spectrum, was tentatively allocated as a further possible extension of this band to the $I^{\pi} = (37^{-})$ level. The transitions connecting the 17^{-} and 15^{-} levels in bands 5 and Band 7a, identified in Ref. [63], were also confirmed when examining coincidence relationships in this work. Band 7a is discussed in more detail in Section 5.2.2

The 7^{-} level at 1862 keV in this band was previously reported to be isomeric with a half-life of 17 $\pm$ 3 ns [64]. The ΔT spectra produced for this level in this work did not show any evidence of an isomeric lifetime distinguishable from the expected prompt lifetime. This supports the conclusion of Refernece [65], where the lifetime is measured to be $\leq$ 0.3 ns, and that this level is not in fact an isomer.

5.1.7 Band 6

Figure 5.5(c) shows the spectrum containing the transitions allocated to Band 6, along with the transitions from the low-lying states of Band 6 to the γ-vibrational and ground-state bands. This spectrum was produced from the sum of double gates, (4^{-}→26^{-})/ (4^{-}→26^{-}), in the thin-target $\gamma\gamma\gamma$ cube.

The spins and parities presented in Partial Level Scheme A for Band 6 are based on the angular distributions presented in Ref. [62]. The inset of this figure shows the sum of double gates ($4^- \rightarrow 14^-$)/ ($14^- \rightarrow 26^-$). An 873-keV γ ray can clearly be identified in this spectrum extending the band to the 28^- level.

5.1.8 γ and β bands

The γ- and β-vibrational bands were established in Refs. [56, 62]. These bands are weakly populated by transitions from bands 4, 5 and 6 as well as being populated by the decay of the $I^\pi = 7^-$ isomer at 1929 keV. The γ rays associated with these bands, observed in the prompt spectroscopy of ^{180}Os, are listed in Table 5.1. The majority of the intensity in the γ- and β-vibrational bands is produced from the decay of the $I^\pi = 7^-$ isomer and several additional transitions were observed in the delayed spectroscopy of this isomer (see Section 5.2.1). These γ rays are shown in Partial Level Scheme B in Fig. 5.6 and are listed in Table 5.3.

The excitation energy of the γ-vibration band is indicative of the degree of γ softness in the nucleus, and will be discussed further in Section 6.7.

5.2 Spectroscopy of the 1929-keV Isomer

The existence of an isomeric state at 1929 keV and $I^\pi = 7^-$ has been well established in several previous studies [56, 58, 63–66]. This isomer was first presented in the study by Nekakis *et al.* [58] and two strongly-coupled rotational bands were identified to be built on the isomeric state (labelled 7a and 7b in this thesis). The study by Leider *et al* [63] further extended these

rotational bands to $I^{\pi} = 31^{-}$ and 32^{-} and identified two additional coupled bands (8a and 8b) which feed into the $I^{\pi} = 12^{-}$ and 11^{-} levels of bands 7a and 7b. Prior to this work bands 8a and 8b were known up to spins of $I^{\pi} = 17^{-}$ and 18^{-}. The complex decay of the isomer was presented in the study Venkova *et al.* [64] and the half-life of the isomer has been measured as ranging from 15 ± 2 ns [65] to 27 ± 5 ns [58].

The level scheme showing the prompt and delayed transitions associated with the $I^{\pi} = 7^{-}$ isomeric state, as deduced in this work, is labelled Partial Level Scheme B and is presented in Fig. 5.6. To investigate the γ rays associated with the isomeric state a prompt-delayed matrix, with the time difference 12 ns $\leq \Delta T \leq$ 50 ns, was created from the thick-target data. The level scheme above the I^{π}=7^{-} isomer, consisting of the four prompt bands, 7a, 7b, 8a and 8b, was produced from further coincidence analysis in the prompt thin- and thick-target $\gamma\gamma\gamma$ cubes and $\gamma\gamma\gamma\gamma$ hypercubes. The intensities for the prompt transitions were measured in the thin-target $\gamma\gamma\gamma$ cube and are given relative to the promptly-populated 132-keV γ ray for ease of comparison to the transitions presented in Partial Level Scheme A. The intensities and energies are listed along with the DCO ratios in Table 5.2, where possible.

The delayed γ-ray transitions associated with the 1929 keV, I^{π}=7^{-} isomer were investigated in a delayed $\gamma\gamma\gamma$ cube, created with the condition $T_{\gamma} \geq$12 ns in the thick-target data. The intensities of the transitions were measured in this matrix with respect to the intensity of the 132 keV γ ray and are listed in Table 5.3.

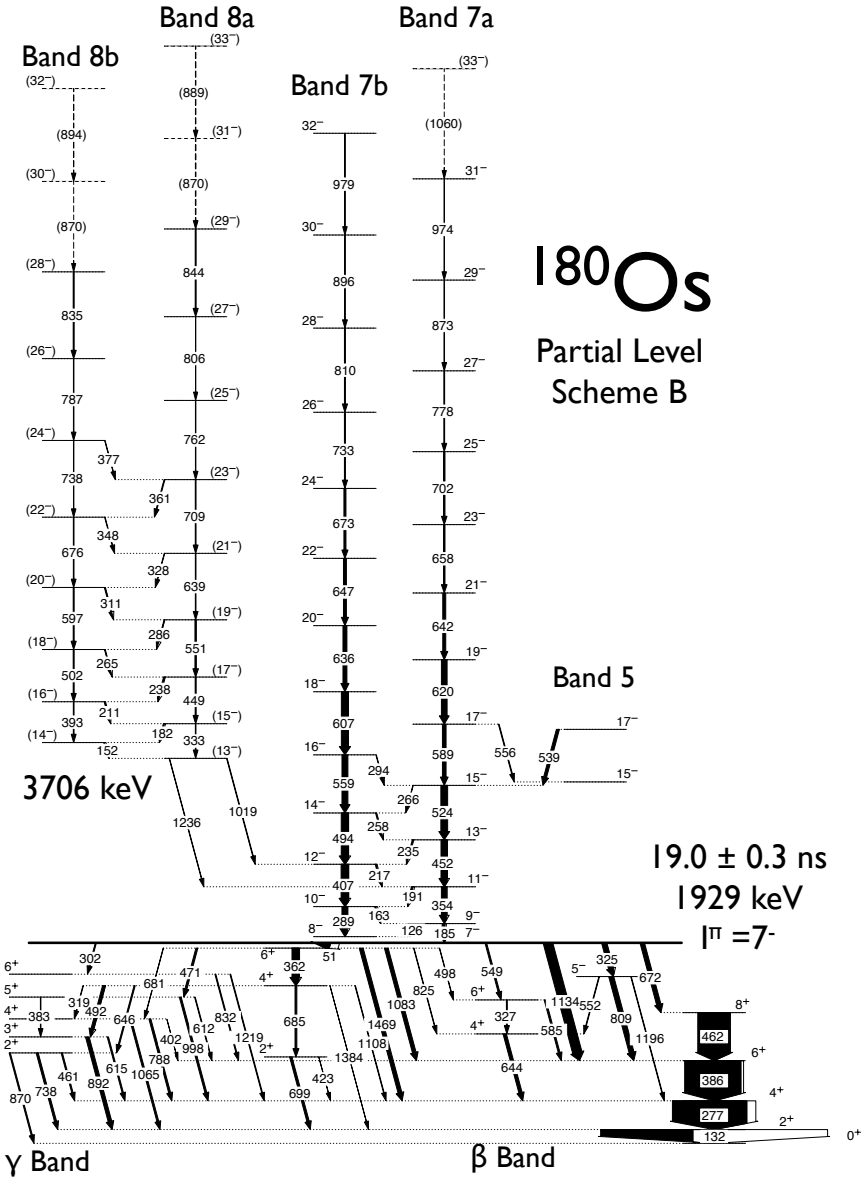

Figure 5.6: Partial Level Scheme B. A partial level scheme for ^{180}Os deduced in this work showing the prompt and delayed transitions of the 1929 keV 7^- isomer. Transition energies are given to the nearest keV. The widths of the arrows are proportional to the total intensity of the transition and the white sections represent the calculated internal conversion. Tentative transitions are denoted with a dashed arrow and tentative spins are give in brackets.

Table 5.2: Energies, intensities, initial and final spins and DCO ratios for prompt γ rays in Partial Level Scheme B. The intensities are normalised to the strongest transition in Partial Level Scheme A and corrected for detector efficiency.

E_γ	$J_i^\pi \rightarrow J_f^\pi$	I_γ	R_{DCO}
	Band 7a		
125.6(9)	$9^- \rightarrow 8^-$	2.6(3)	0.36(3)
185.1(9)	$9^- \rightarrow 7^-$	3.2(2)	1.0(1)
190.6(1)	$11^- \rightarrow 10^-$	1.7(1)	0.31(2)
354.1(1)	$11^- \rightarrow 9^-$	5.82(1)	1.01(4)
235.1(1)	$13^- \rightarrow 12^-$	1.0(1)	0.25(5)
451.8(1)	$13^- \rightarrow 11^-$	6.9(1)	0.86(4)
265.5(4)	$15^- \rightarrow 14^-$	0.3(1)	0.33(4)
523.9(1)	$15^- \rightarrow 13^-$	7.2(3)	0.99(3)
555.6(10)	$17^- \rightarrow 15^-$	0.8(2)	
588.8(1)	$17^- \rightarrow 15^-$	3.9(2)	0.94(7)
619.9(2)	$19^- \rightarrow 17^-$	6.1(3)	0.95(7)
642.4(1)	$21^- \rightarrow 19^-$	3.2(2)	1.02(8)
657.7(1)	$23^- \rightarrow 21^-$	1.6(1)	1.09(12)
702.0(1)	$25^- \rightarrow 23^-$	1.5(2)	
777.6(1)	$27^- \rightarrow 25^-$	0.8(1)	
873.1(2)	$29^- \rightarrow 27^-$	0.6(1)	
974.1(2)	$31^- \rightarrow 29^-$	0.3(1)	
1060.0(10)	$33^- \rightarrow 31^-$	0.1(1)	
	Band 7b		
163.4(1)	$10^- \rightarrow 9^-$	1.22(8)	0.19(2)
289.0(1)	$10^- \rightarrow 8^-$	5.84(7)	0.96(3)
216.7(1)	$12^- \rightarrow 11^-$	1.15(7)	0.17(9)
407.3(1)	$12^- \rightarrow 10^-$	8.0(3)	1.07(4)

Table 5.2: Continued.

E_γ	$J_i^\pi \rightarrow J_f^\pi$	I_γ	R_{DCO}
258.4(1)	$14^- \rightarrow 13^-$	0.86(8)	0.28(4)
493.5(1)	$14^- \rightarrow 12^-$	7.8(3)	0.99(3)
293.8(6)	$16^- \rightarrow 15^-$	0.39(6)	0.29(8)
559.3(1)	$16^- \rightarrow 14^-$	6.3(3)	0.92(4)
607.2(1)	$18^- \rightarrow 16^-$	7.6(3)	0.94(3)
636.0(1)	$20^- \rightarrow 18^-$	4.2(2)	0.95(4)
647.5(1)	$22^- \rightarrow 20^-$	3.1(2)	1.03(5)
672.6(1)	$24^- \rightarrow 22^-$	2.2(1)	0.90(12)
732.9(1)	$26^- \rightarrow 24^-$	1.1(1)	
809.6(1)	$28^- \rightarrow 26^-$	1.1(1)	
895.8(2)	$30^- \rightarrow 28^-$	0.7(1)	
978.9(2)	$32^- \rightarrow 30^-$	0.3(1)	
	Band 8a		
1019.1(1)	$(13^-) \rightarrow 12^-$	0.6(1)	0.41(11)
1235.8(1)	$(13^-) \rightarrow 11^-$	0.4(1)	1.28(27)
181.5(1)	$(15^-) \rightarrow (14^-)$	1.1(1)	
333.3(2)	$(15^-) \rightarrow (13^-)$	0.6(1)	
237.5(1)	$(17^-) \rightarrow (16^-)$	1.2(1)	
448.9(1)	$(17^-) \rightarrow (15^-)$	1.0(1)	
286.0(2)	$(19^-) \rightarrow (18^-)$	0.6(2)	
550.8(1)	$(19^-) \rightarrow (17^-)$	1.5(1)	
328.2(2)	$(21^-) \rightarrow (20^-)$	0.4(1)	
639.4(2)	$(21^-) \rightarrow (19^-)$	0.7(1)	
361.3(1)	$(23^-) \rightarrow (22^-)$	0.8(1)	
709.4(3)	$(23^-) \rightarrow (21^-)$	0.8(1)	
762.0(2)	$(25^-) \rightarrow (23^-)$	0.5(1)	
805.7(10)	$(27^-) \rightarrow (25^-)$	0.2(1)	
843.9(10)	$(29^-) \rightarrow (27^-)$	0.9(1)	

Table 5.2: Continued.

E_γ	$J_i^\pi \rightarrow J_f^\pi$	I_γ	R_{DCO}
870.4(10)	$(31^-) \rightarrow (29^-)$	0.6(1)	
888.9(10)	$(33^-) \rightarrow (31^-)$	0.5(1)	
	Band 8b		
151.8(1)	$(14^-) \rightarrow (13^-)$	0.9(1)	
211.3(1)	$(16^-) \rightarrow (15^-)$	0.9(1)	
392.9(1)	$(16^-) \rightarrow (14^-)$	0.7(1)	
264.9(1)	$(18^-) \rightarrow (17^-)$	0.6(1)	
502.4(1)	$(18^-) \rightarrow (16^-)$	1.0(1)	
311.1(2)	$(20^-) \rightarrow (19^-)$	0.9(1)	
597.1(1)	$(20^-) \rightarrow (18^-)$	1.0(1)	
348.1(1)	$(22^-) \rightarrow (21^-)$	0.5(1)	
676.4(1)	$(22^-) \rightarrow (20^-)$	0.7(1)	
376.9(3)	$(24^-) \rightarrow (23^-)$	0.4(1)	
738.2(2)	$(24^-) \rightarrow (22^-)$	0.4(1)	
787.3(2)	$(26^-) \rightarrow (24^-)$	0.5(1)	
834.8(10)	$(28^-) \rightarrow (26^-)$	1.0(1)	
869.9(10)	$(30^-) \rightarrow (28^-)$	0.2(1)	
893.7(10)	$(32^-) \rightarrow (30^-)$	0.3(1)	
539.0(10)	$(17^-) \rightarrow (15^-)$	3.1(5)	

Table 5.3: Energies, intensities, initial and final spins for delayed γ rays in Partial Level Scheme B. The intensities are normalised to the strongest transition and are corrected for detector efficiency.

E_γ	$J_i^\pi \rightarrow J_f^\pi$	I_γ
	GSB	
132.3(1)	$2^+ \rightarrow 0^+$	100(3)

Table 5.3: Continued.

E_γ	$J_i^\pi \rightarrow J_f^\pi$	I_γ
276.5(1)	$4^+ \rightarrow 2^+$	81(5)
386.2(1)	$6^+ \rightarrow 4^+$	61(3)
462.4(1)	$8^+ \rightarrow 6^+$	34(2)
	β Band	
644.0(1)	$4^+ \rightarrow 4^+$	3.4(5)
327.0(1)	$6^+ \rightarrow 4^+$	0.9(2)
584.7(1)	$6^+ \rightarrow 6^+$	1.7(3)
	γ Band	
461.1(2)	$2^+ \rightarrow 4^+$	1.4(2)
737.6(2)	$2^+ \rightarrow 2^+$	2.2(7)
870.0(9)	$2^+ \rightarrow 0^+$	1.2(7)
615.2(1)	$3^+ \rightarrow 4^+$	1.3(3)
891.7(1)	$3^+ \rightarrow 2^+$	3.8(8)
402.2(1)	$4^+ \rightarrow 6^+$	0.1(3)
788.4(10)	$4^+ \rightarrow 4^+$	2.0(3)
1065.0(10)	$4^+ \rightarrow 2^+$	1.9(7)
383.1(1)	$5^+ \rightarrow 3^+$	0.5(3)
612.0(10)	$5^+ \rightarrow 6^+$	0.7(3)
998.3(10)	$5^+ \rightarrow 4^+$	2.0(3)
832.5(1)	$6^+ \rightarrow 6^+$	1.0(1)
1218.8(1)	$6^+ \rightarrow 4^+$	0.8(2)
	Delayed transitions	
319.1(10)	$4^+ \rightarrow 4^+$	0.4(1)
361.8(1)	$6^+ \rightarrow 4^+$	7.8(5)
422.5(10)	$2^+ \rightarrow 4^+$	0.2(3)
471.2(1)	$6^+ \rightarrow 5^+$	1.9(2)
492.4(10)	$4^+ \rightarrow 3^+$	3.0(3)
498.5(10)	$6^+ \rightarrow 6^+$	0.4(1)
551.7(10)	$5^- \rightarrow 4^+$	0.7(1)
646.5(1)	$4^+ \rightarrow 2^+$	1.2(2)
681.0(10)	$6^+ \rightarrow 4^+$	0.3(2)
685.1(10)	$4^+ \rightarrow 2^+$	1.9(2)

Table 5.3: Continued.

E_γ	$J_i^\pi \rightarrow J_f^\pi$	I_γ
699.0(1)	$2^+ \rightarrow 2^+$	2.4(7)
809.5(1)	$5^- \rightarrow 6^+$	5.3(4)
825.4(10)	$6^+ \rightarrow 4^+$	0.5(2)
1083.2(10)	$6^+ \rightarrow 6^+$	3.9(3)
1107.6(10)	$4^+ \rightarrow 4^+$	0.6(1)
1195.7(9)	$5^- \rightarrow 4^+$	0.6(1)
1384.1(10)	$4^+ \rightarrow 2^+$	0.1(1)
1469.4(1)	$6^+ \rightarrow 4^+$	4.1(6)
50.9(8)	$7^- \rightarrow 6^+$	19(2)
301.5(8)	$7^- \rightarrow 6^+$	1.1(2)
324.6(7)	$7^- \rightarrow 5^-$	5.2(3)
549.3(5)	$7^- \rightarrow 6^+$	1.7(2)
671.6(9)	$7^- \rightarrow 8^+$	4.7(3)
1134.0(9)	$7^- \rightarrow 6^+$	10.2(6)

5.2.1 Decay of the 7^- isomer

The majority of the transitions presented in the delayed level scheme for the 1929-keV isomer in this work are consistent with those reported in Ref. [64]. Two new transitions were identified with energies of 423 and 552 keV with low relative intensities of 0.2% and 0.7% relative to the 132-keV ground-state band transition, respectively. The main evidence for these transitions was provided by the coincidence analysis of the delayed $\gamma\gamma\gamma$ cube, created with the time difference condition 12 ns $\leq \Delta T \leq$ 50 ns. The 423-keV γ ray feeds directly into the $I^\pi = 4^+$ level of the ground-state band from a level with $I^\pi = 2^+$. Figure 5.7(a) shows the spectrum produced by the double gate 362 keV/685 keV in the delayed $\gamma\gamma\gamma$ cube. As well as the showing the

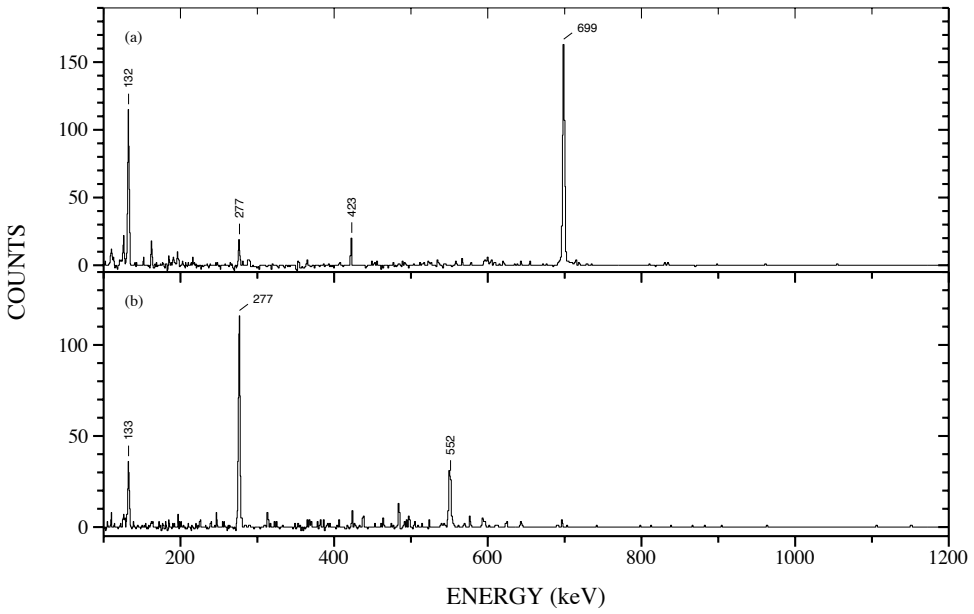

Figure 5.7: Spectra showing the new delayed transitions in Partial Level Scheme B. (a) The spectrum produced from the double gate 362 keV/685 keV in the delayed $\gamma\gamma\gamma$ cube. (b) The spectrum produced from the double gate 325 keV/644 keV in the delayed $\gamma\gamma\gamma$ cube.

expected 699-keV γ-ray coincidence, the 423-keV γ ray and the following 277- and 132-keV γ rays are seen in this spectrum, confirming the placement. The 552-keV γ-ray decays to the $I^{\pi} = 4^{+}$ level of the β-vibrational band from a $I^{\pi}=5^{-}$ level fed directly by the isomer. Figure 5.7 contains the coincidence spectrum produced by the double gate 325 keV/644 keV. The 552-keV γ ray and coincident ground-state band transitions are observed in this spectrum, supporting the placement of the 552-keV γ ray in the level scheme.

It was not possible to directly measure the DCO ratios for the 423- and 552-keV transitions, though it was possible to allocate them as $E2$ and $M1$, respectively, based on the spins and parity of the initial and final states.

Half-life measurement

To measure the half-life of the 7^- isomer a series of prompt-ΔT matrices were created, each with a coincidence gate on one of the delayed γ rays associated with the 7^- isomer, with energies of 325, 362, 809, 1083 and 1134 keV. These γ rays were selected due to the relatively large intensities of the transitions and the fact that clean gates could be set on them. Backgound-subtracted ΔT spectra were produced in each of these matrices by gating on the prompt transitions above the isomer. The prompt γ rays with energies of 289, 354, 407, 452 and 494 keV were selected as they provided the cleanest gates and decay most directly into the isomer. In total this produced 25 ΔT spectra from which the half-life of the 7^- was calculated.

Each ΔT spectrum was fitted with a convoluted exponential decay curve and gaussian using the *nanofit* program described in Section 4.3.1. The weighted average of the half-lives deduced in these fits was calculated to determine the half-life of the 7^- isomeric state as 19.0 $\pm$ 0.3 ns. The sum of the individual ΔT spectra, with a fit representing the half-life calculated from the weighted average, is shown in Fig. 5.8. The systematic error in the half-life was calculated from the standard deviation of the fitted values. The statistical error associated with the individual fits were of the order of 0.5 ns.

The error in the value of the half-life measured in this study has been reduced by a factor of 10 compared to previous studies due to a combination of the high statistics of the experiment, the implementation of the ΔT method and fitting with the *nanofit* program. The half-life established in this work is consistent within 2σ of the previous measurements of 15 $\pm$ 2 ns [65] and 16 $\pm$ 2 ns [56]. Other previous measurements of the half-life as 27 $\pm$5 [58] and 26 $\pm$ 3 ns [64] are consistent within 2σ and 3σ of the half-life established

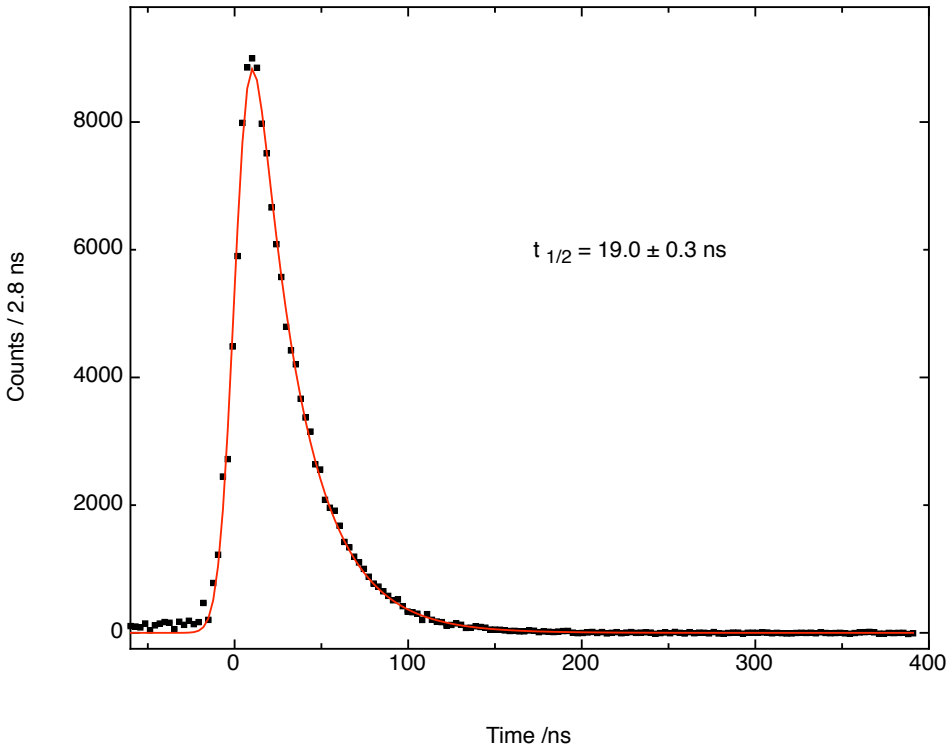

Figure 5.8: [Colour] The ΔT spectrum for the 1929-keV 7^- isomer produced from the sum of 25 individual time spectra. These time spectra were produced from gates on 5 prompt γ rays, with energies 289, 354, 407, 452 and 494 keV, in each of 5 prompt-ΔT matrices gated on delayed γ rays with energies 325, 362, 809, 1083 and 1134 keV. The red line shows a convoluted exponential decay curve with a half life of 19.0 ns.

in this study, repsectively; however, due to their large errors they can be discounted.

5.2.2 Bands 7a and 7b

Bands 7a and 7b and consequently bands 8a and 8b were confirmed as feeding into the 1929-keV isomer through analysis of the prompt-delayed matrix with the timing condition 12 ns $\leq \Delta T \leq$ 50 ns. These time limits were chosen based on the half-life of the isomeric state to give the maximum

possible statistics while reducing contamination from longer-lived isomers. The spectrum in Fig. 5.9 was produced from the summation of several gates on delayed γ rays decaying from the 1929-keV isomer with energies 362-, 325-, 492-, 672- and 1134-keV.

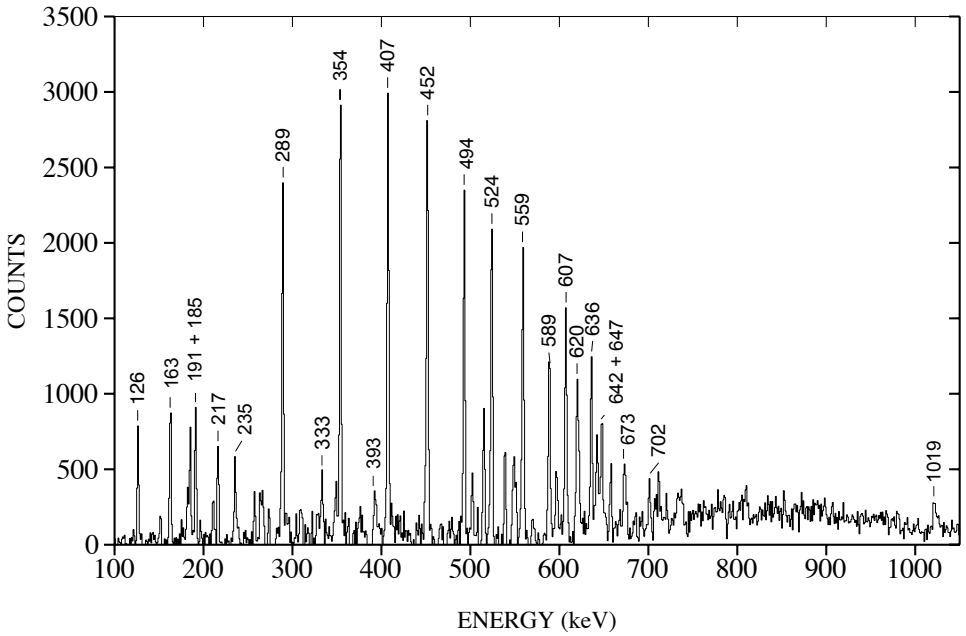

Figure 5.9: A spectrum produced by the sum of the individual gates on the 362-, 325-, 492-, 672- and 1134-keV delayed γ rays in the prompt-delayed matrix 12 ns $\leq\Delta T \leq$50 ns, showing the prompt γ rays above the 1929-keV isomer.

Due to the limited number of statistics in the prompt-delayed matrix it was not possible to observe the highest spin transitions of bands 7a and 7b with this method. Once the position above the isomer was confirmed the thick-target prompt $\gamma\gamma\gamma$ cubes and $\gamma\gamma\gamma\gamma$ hypercubes were used to investigate the band structure to high spin. A spectrum containing the transitions allocated to bands 7a is shown in Fig. 5.10(a). This spectrum was produced from the sum of triple gates ($7^- \rightarrow 19^-$)/ ($19^- \rightarrow 31^-$)/ ($19^- \rightarrow 31^-$) in the thick-target $\gamma\gamma\gamma\gamma$ hypercube. The γ rays labelled with open squares in the

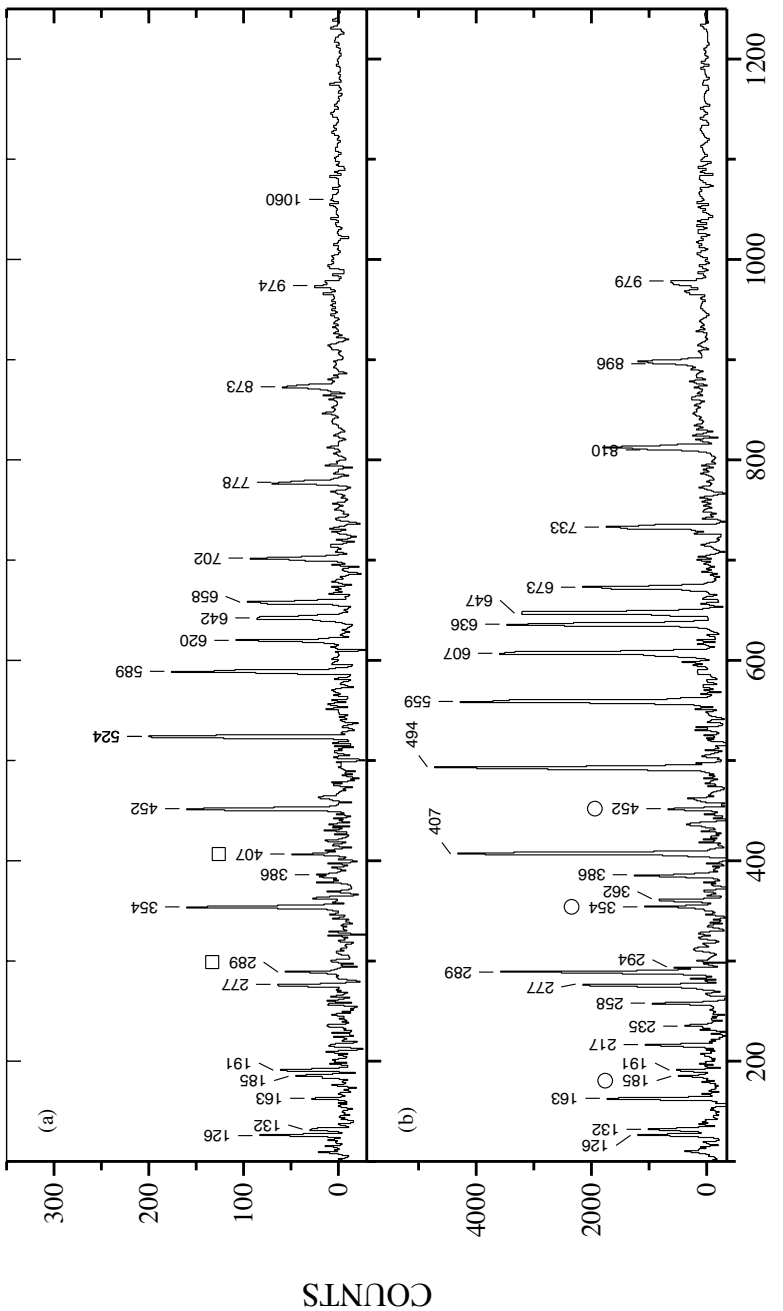

Figure 5.10: Spectra showing prompt transitions in Partial Level Scheme B produced from the sum of triple gates in the in the thick-target $\gamma\gamma\gamma\gamma$ hypercube or double gates in the thick-target $\gamma\gamma\gamma$ cube: (a) Band 7a, $(7^- \rightarrow 19^-)$/ $(19^- \rightarrow 31^-)$/ $(19^- \rightarrow 31^-)$. γ rays in Band 7b are labelled with open squares. (b) Band 7b, $(8^- \rightarrow 22^-)$/ $(22^- \rightarrow 32^-)$. The open circles denote the transitions belonging to Band 7a.

spectrum are those allocated to Band 7b. They are seen in this spectrum due to the connecting γ-ray transitions up to the I=15$^-$ level, also resolvable in this spectrum.

The level scheme for Band 7a produced in this work (Fig. 5.6) is consistent with that presented in Ref. [63]. The 1060-keV transition seen in the coincidence analysis performed in this work, and observed in Fig. 5.10(a), has been tentatively assigned as an extentsion to this band to a spin of I^π=33$^-$. The 185-keV γ ray decaying directly in to the isomer was identified for the first time in Ref. [63] and was confirmed in this study. The DCO ratio for this transition was measured in this study as 1.0 $\pm$ 0.1 indicating an $E2$ transition ($\Delta I = 2$) and confirms the spin assignments for this band.

Figure 5.10(b) shows the spectrum containing transitions assigned to Band 7b, produced from the sum of double gates (8$^-\rightarrow$22$^-$)/ (22$^-\rightarrow$32$^-$) in the thick-target $\gamma\gamma\gamma$ cube. The open circles label the transitions belonging to Band 7a. The level scheme produced for Band 7b in this work is consistent with that presented in Ref. [63].

Despite bands 7a and 7b feeding into an isomeric state, the ground-state band transitions up to spins $I^\pi = 6^-$ can be seen in the aforementioned spectra, which show only the γ rays coincident within 12 ns of the transitions in the band. The half-life of the 7$^-$ isomer is relatively short at 19.0 $\pm$ 0.3 ns, therefore, a substantial amount of transitions decay from the isomer before the timing condition $T_\gamma\leq$12 ns condition excludes them. The relatively low intensity of the ground-state transitions in these spectra indicates that some of the transitions into the ground-state band were excluded by the timing condition on the matrix.

5.2.3 Bands 8a and 8b

Due to the low intensity of bands 8a and 8b it was not possible to perform a meaningful coincidence analysis of these bands in the prompt-delayed matrix produced for the 1929-keV isomer. The lowest-lying transitions in these bands, with energies of 333 and 393 keV, along with the 1019-keV transition connecting the bands to Band 7b, are weakly populated in the spectrum showing the prompt coincidences of the 1929-keV isomeric state (Fig. 5.9). The structure and transitions associated with bands 8a and 8b were further examined in the thick-target $\gamma\gamma\gamma$ cube.

The spectrum shown in Fig. 5.11(a) was produced from the sum of triple gates, $(17^- \rightarrow 13^-)/\ (25^- \rightarrow 17^-)$, in the thick-target $\gamma\gamma\gamma$ cube and shows the transitions associated with Band 8a. The γ rays with energies 639, 709, 762, 806 and 844 keV were identified as part of Band 8a and extend the band to a spin of I^π=29$^-$ from the previously established level with spin of I^π=19$^-$ [63]. Transitions with energies 870 and 889 keV were also identified as possible extensions to Band 8a to spin I^π=33$^-$. Transitions linking Band 8a to Band 8b are also seen in this spectrum and have been established up to the level with spin of I^π=24$^-$ with energies of 152, 211, 265, 311, 348, and 377 keV. The latter two are identified for the first time in this work. Transitions belonging to Band 8b seen in this spectrum are labelled with solid triangles and the transitions associated with bands 7a and 7b are labelled with open triangles.

A spectrum showing the γ rays associated with Band 8b was created from the sum of triple gates, $(18^- \rightarrow 14-)/\ (26^- \rightarrow 14^-)$, in the thick-target $\gamma\gamma\gamma$ cube and is shown in Fig. 5.11 (b). The solid diamonds denote transitions belonging to Band 8a and the open diamonds denote the transitions associ-

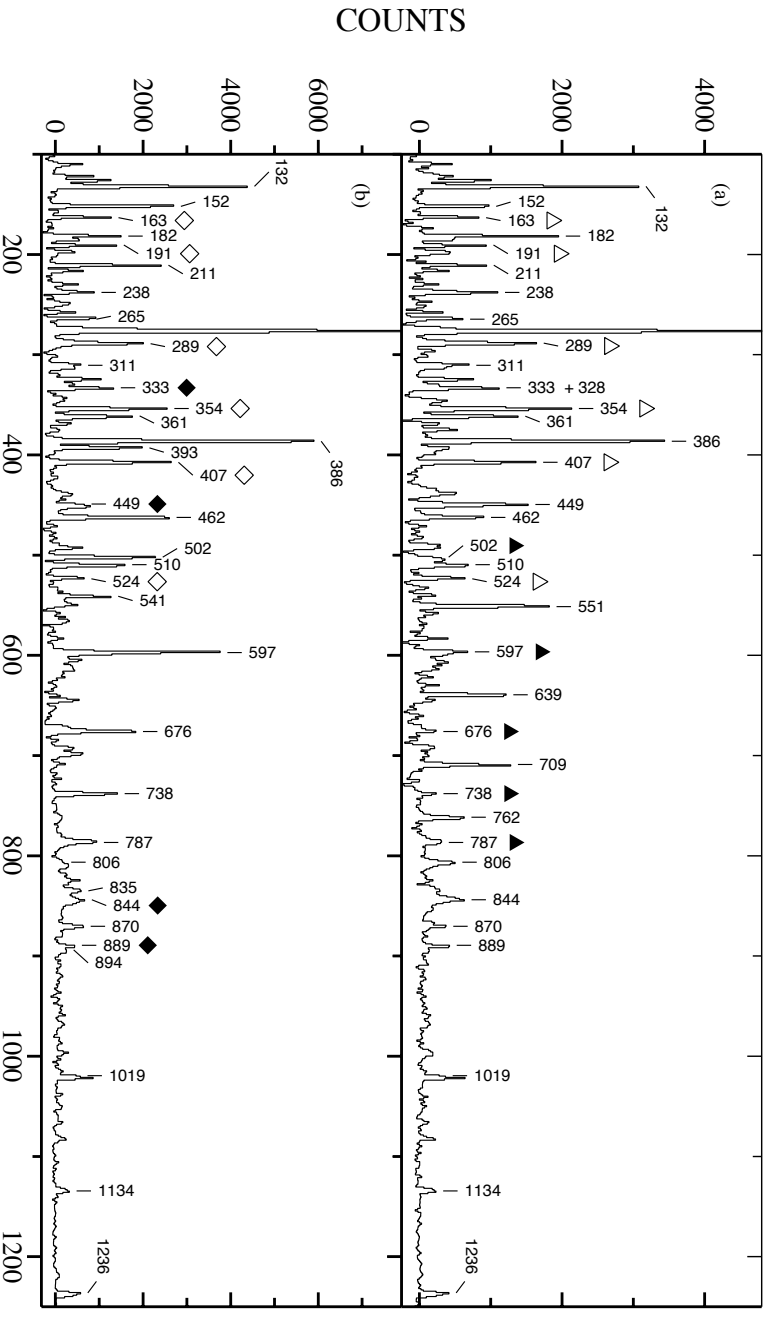

Figure 5.11: Spectra showing prompt transitions in Partial Level Scheme B produced from the sum of triple gates in the in the thick-target double gates in the thick-target $\gamma\gamma\gamma$ cube: (a) Band 8a, $(17^- \rightarrow 13^-)$/ $(25^- \rightarrow 17^-)$. The solid triangles denote the transitions belonging to Band 8b and the open triangles denote the transitions associated with bands 7a to 7b. (b) Band 8b, $(18^- \rightarrow 14-)$/ $(26^- \rightarrow 14^-)$. The solid diamonds denote the transitions belonging to Band 8a and the open diamonds denote the transitions associated with bands 7a to 7b.

ated with bands 7a and 7b. The 676-, 738-, 787- and 835-keV γ rays seen in this spectrum were identified as extending Band 8b to a spin of $I^{\pi}=28^{-}$ from the previously-presented level with spin of $I^{\pi}=20^{-}$ [63]. The 870- and 894-keV transitions were established as possible extensions to this band and have been tentatively assigned to spins $I^{\pi}=30^{-}$ and $I^{\pi}=32^{-}$, respectively. Transitions with energies 328 and 361 keV were also newly identified as transitions from the levels with $I^{\pi}=21^{-}$ and 23^{-} in Band 8b to 8a, respectively.

The γ-ray transitions from the band head of Band 8a to the $I^{\pi}=11^{-}$ level in Band 7a and the $I^{\pi}=12^{-}$ level in Band 7b are seen at 1019- and 1236-keV, respectively, in both the coincidence spectra for bands 8a and 8b. The DCO ratios for these transitions form the basis of the spin assignment for the band head of Band 8a and consequently both bands. The DCO ratio for the 1019-keV transition was measured as 0.41 ± 0.11 and suggests a $\Delta I = 1$ transition. The DCO for the 1236-keV transitions was measured as 1.28 ± 0.27 and indicates a $\Delta I = 2$ transition. Subsequently, it was determined that the band head of Band 8a has a spin of $I^{\pi}=13^{-}$ differing from that assigned in Ref. [63] of $I^{\pi}=11^{-}$. The latter was based on DCO ratios with significantly large errors and did not rule out the assignment presented in this work.

The half-life of the band-head state was found to be less than the experimental limit of $T_{1/2} \leq 10$ ns and is consistent with decays of the mixed $M1/E2$ and $E2$ nature. Therefore, the parity of the band was determined to be negative, in agreement with Ref. [63].

5.3 Spectroscopy of the 5848-keV and 7592-keV isomers

An isomeric state at 5848 keV was established in the study by Venkova *et al.* [64]. The level scheme presented in this reference is shown in Fig. 5.12 and shows the isomer as decaying into the 18^+ level of Band 1b, through an intermediate state at 5562 keV. A spin limit of $I \geq 20$ was also assigned to the isomer based on the decay sequence. Prior to the current experiment two delayed γ rays with energies of 287 and 1426 keV were known to decay from this isomer. The half-life of the state was measured to be 12 ± 4 ns based on the decay curve for the 287-keV transition. No prompt γ rays have been previously identified above this isomeric state.

An additional isomer, with a half-life of 41 ± 10 ns and a spin of $I \geq 16$, was proposed in the study by Venkova *et al.* [64], and is shown in Fig. 5.12. The study by Pederson *et al.* [66] also proposed an isomer with a half-life of ~ 130 ns feeding into bands 1a and 1b. The half-lives assigned in both of these previous studies, were based on the study of delayed components of several transitions in the ground-state band and bands 1a and 1b. Prior to the current study, no direct decays linked these proposed isomers to the established level scheme for ^{180}Os and the excitation energy of the states was unknown.

Partial Level Scheme C, shown in Fig. 5.13, presents the delayed transitions associated with the 5848-keV isomer as deduced in this work. This level scheme also contains the complex decay scheme for an additional isomeric state identified at 7592 keV, which decays into bands 1a and 3 as well as into the bands above the 5848-keV isomer.

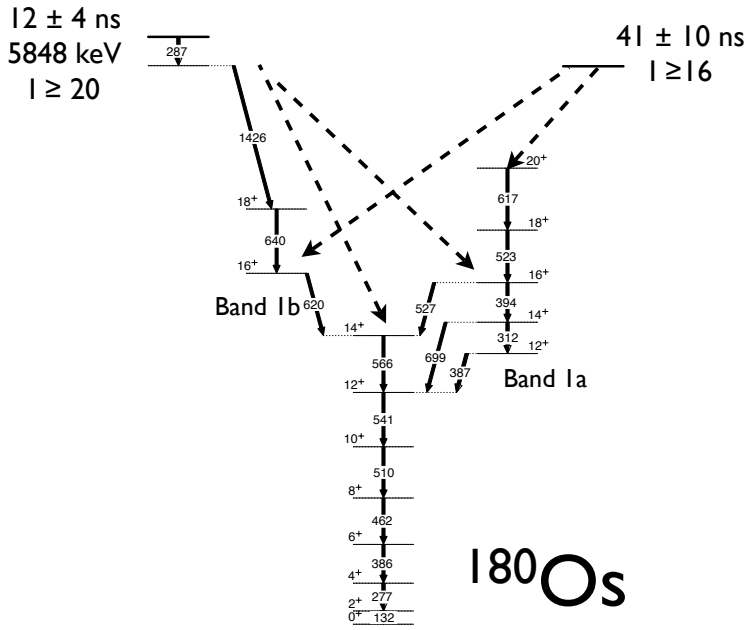

Figure 5.12: A partial level scheme for ^{180}Os deduced in Ref. [64]. The intensity of the γ rays has not been represented in this level schene. Tentative assignments are denoted with a dashed arrow.

Numerous histograms were created to investigate the level scheme of these isomers. The delayed transitions from the two isomeric states were first identified in this work in delayed $\gamma\gamma\gamma$ cubes with varying T_γ conditions. The prompt transitions above the isomers were then established through the coincidence analysis of prompt-delayed matrices, created with varying ΔT conditions. Once both the prompt and delayed γ rays were identified for each isomer, the half-lifes were measured in ΔT-prompt matrices and subsequent matrices were produced with timing conditions specific to each isomer.

For each isomer, a delayed $\gamma\gamma$ matrix and $\gamma\gamma\gamma$ cubes were created to contain only those transitions in coincidence with a prompt γ ray feeding that isomer. A range of ΔT was also specified and was derived from the half-

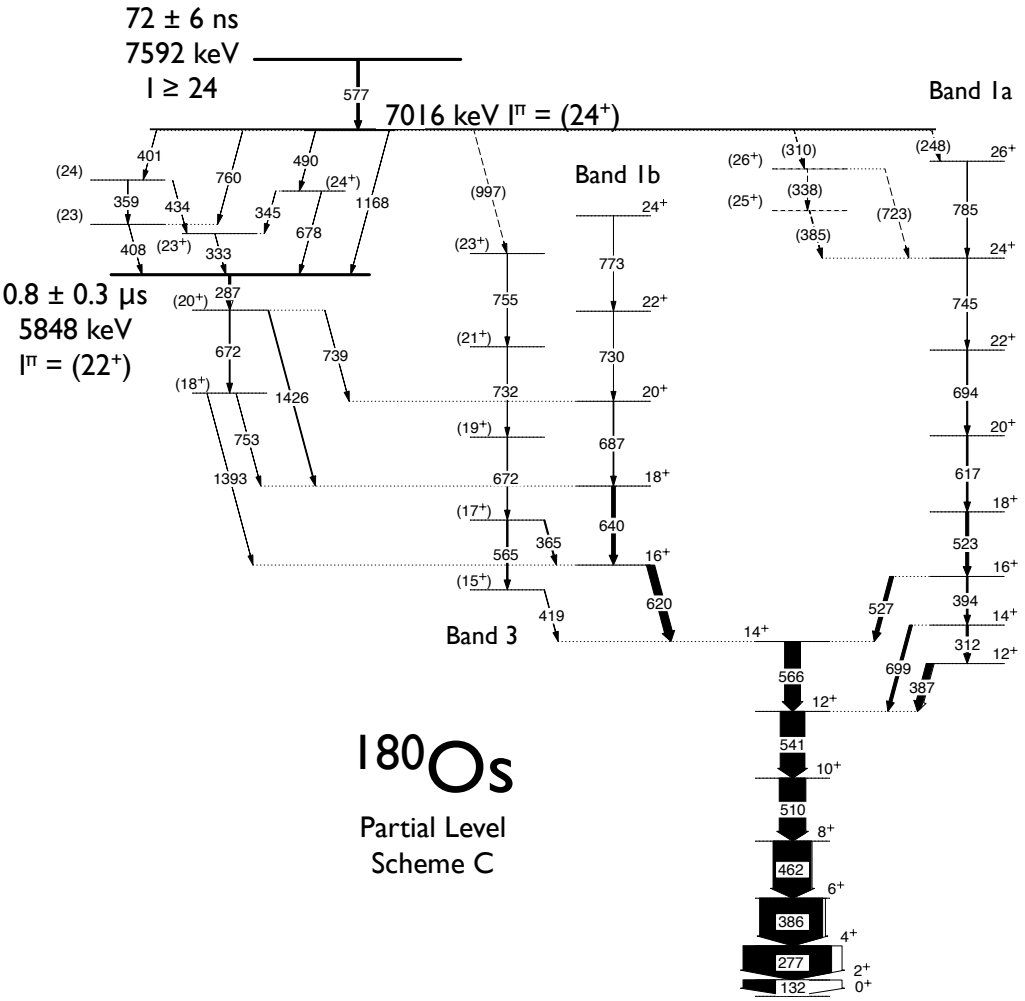

Figure 5.13: Partial Level Scheme C. A partial level scheme for ^{180}Os deduced in this work for the delayed transitions from the 5848-keV and 7592-keV isomers. Transition energies are given to the nearest keV. The widths of the arrows are proportional to the total intensity of the transition and the white sections represent the calculated internal conversion. Tentative assignments are denoted with a dashed arrow and tentative spins are given in brackets.

life measured for each isomeric state to give the highest possible statistics and least contaminated spectra. From these spectra the delayed level scheme in Fig. 5.13 was established. The intensities of the delayed γ rays for each

isomer were measured in the delayed $\gamma\gamma$ matrix specific to that isomer and were normalised to the intensity of the 277-keV transition in the ground-state band. The energies and intensities for the delayed transitions are listed in Table 5.4.

Table 5.4: Energies, intensities, initial and final spins for prompt γ rays in Partial Level Scheme C. The intensities are normalised to the 277-keV transition in the ground-state band and corrected for detector efficiency.

E_γ	$J_i^\pi \rightarrow J_f^\pi$	I_γ
	GSB	
132.3(1)	$2^+ \rightarrow 0^+$	46(3)
276.5(1)	$4^+ \rightarrow 2^+$	100(8)
386.3(1)	$6^+ \rightarrow 4^+$	71(4)
462.4(1)	$8^+ \rightarrow 6^+$	42.8(2)
510.3(1)	$10^+ \rightarrow 8^+$	29.4(9)
541.1(1)	$12^+ \rightarrow 10^+$	27.4(15)
566.2(1)	$14^+ \rightarrow 12^+$	17.6(10)
	Band 1a	
387.5(10)	$12^+ \rightarrow 12^+$	7.6(4)
311.9(10)	$14^+ \rightarrow 12^+$	2.3(2)
699.3(10)	$14^+ \rightarrow 12^+$	3.4(3)
394.3(1)	$16^+ \rightarrow 14^+$	1.8(2)
527.4(10)	$16^+ \rightarrow 14^+$	4.4(3)
523.3(1)	$18^+ \rightarrow 16^+$	3.4(2)
616.8(1)	$20^+ \rightarrow 18^+$	1.8(1)
694.2(1)	$22^+ \rightarrow 20^+$	1.2(2)
745.0(1)	$24^+ \rightarrow 22^+$	0.2(1)
785.4(1)	$26^+ \rightarrow 24^+$	0.1(1)
	Band 1b	
619.6(1)	$16^+ \rightarrow 14^+$	8.9(4)
640.2(1)	$18^+ \rightarrow 16^+$	4.1(2)
687.0(1)	$20^+ \rightarrow 18^+$	0.9(1)
729.8(10)	$22^+ \rightarrow 20^+$	0.2(1)

Table 5.4: Continued.

E_γ	$J_i^\pi \rightarrow J_f^\pi$	I_γ
773.3(1)	$24^+ \rightarrow 22^+$	0.2(1)
Band 3		
418.8(10)	$(15^+) \rightarrow 14^+$	0.5(2)
364.5(10)	$(17^+) \rightarrow 16^+$	1.1(2)
565.2(3)	$(17^+) \rightarrow (15^+)$	1.6(3)
672.0(1)	$(19^+) \rightarrow (17^+)$	0.7(1)
732.2(1)	$(21^+) \rightarrow (19^+)$	0.2(1)
755.4(1)	$(23^+) \rightarrow (21^+)$	0.1(1)
Decays from 5848-keV isomer		
753.2(1)	$(18^+) \rightarrow 18^+$	0.1(1)
1393.4(1)	$(18^+) \rightarrow 16^+$	0.1(1)
672.3(1)	$(20^+) \rightarrow (18^+)$	0.5(2)
738.5(10)	$(20^+) \rightarrow 20^+$	0.3(1)
1425.5(1)	$(20^+) \rightarrow 18^+$	1.2(3)
287.3(10)	$(22^+) \rightarrow (20^+)$	2.2(1)
Decays from 7592-keV isomer into 5848 keV isomer		
333.0(1)	$(23^+) \rightarrow (22^+)$	0.2(1)
407.7(1)	$(23) \rightarrow (22^+)$	0.3(1)
345.0(1)	$(24^+) \rightarrow (23^+)$	0.2(1)
678.0(10)	$(24^+) \rightarrow (22^+)$	0.1(1)
359.5(10)	$(24) \rightarrow (23)$	0.1(1)
434.2(10)	$(24) \rightarrow (23^+)$	0.1(1)
400.8(10)	$(24^+) \rightarrow (24)$	0.1(1)
490.0(1)	$(24^+) \rightarrow (24^+)$	0.4(1)
760.2(10)	$(24^+) \rightarrow (23)$	0.1(1)
1167.9(10)	$(24^+) \rightarrow (22^+)$	0.1(1)
576.7(10)	$\rightarrow (24^+)$	2.90(2)
Decays from the 7592-keV isomer		
248.4(10)	$(24^+) \rightarrow 26^+$	0.2(2)
310.4(1)	$(24^+) \rightarrow (26^+)$	0.3(1)
996.6(10)	$(24^+) \rightarrow (23^+)$	0.2(1)
385.4(10)	$(25^+) \rightarrow 24^+$	0.8(1)

Table 5.4: Continued.

E_γ	$J_i^\pi \rightarrow J_f^\pi$	I_γ
337.9(1)	$(26^+) \rightarrow (25^+)$	0.1(1)
723.4(10)	$(26^+) \rightarrow 24^+$	0.1(1)

Similarly, prompt $\gamma\gamma$ matrices and $\gamma\gamma\gamma$ cubes were created for each isomer, containing only those transitions in coincidence with a delayed γ ray from that isomer. The same ΔT range for the prompt-delayed coincidences was set equal to that used to create the delayed histograms for the isomer. Coincidence analysis within these prompt histograms was performed and produced the prompt level scheme for the two isomeric states, shown in Partial Level Scheme D in Fig. 5.14. The intensities of the prompt transitions were measured in the prompt $\gamma\gamma$ matrices for each isomer and are listed in Table 5.5 along with the energies of the transitions.

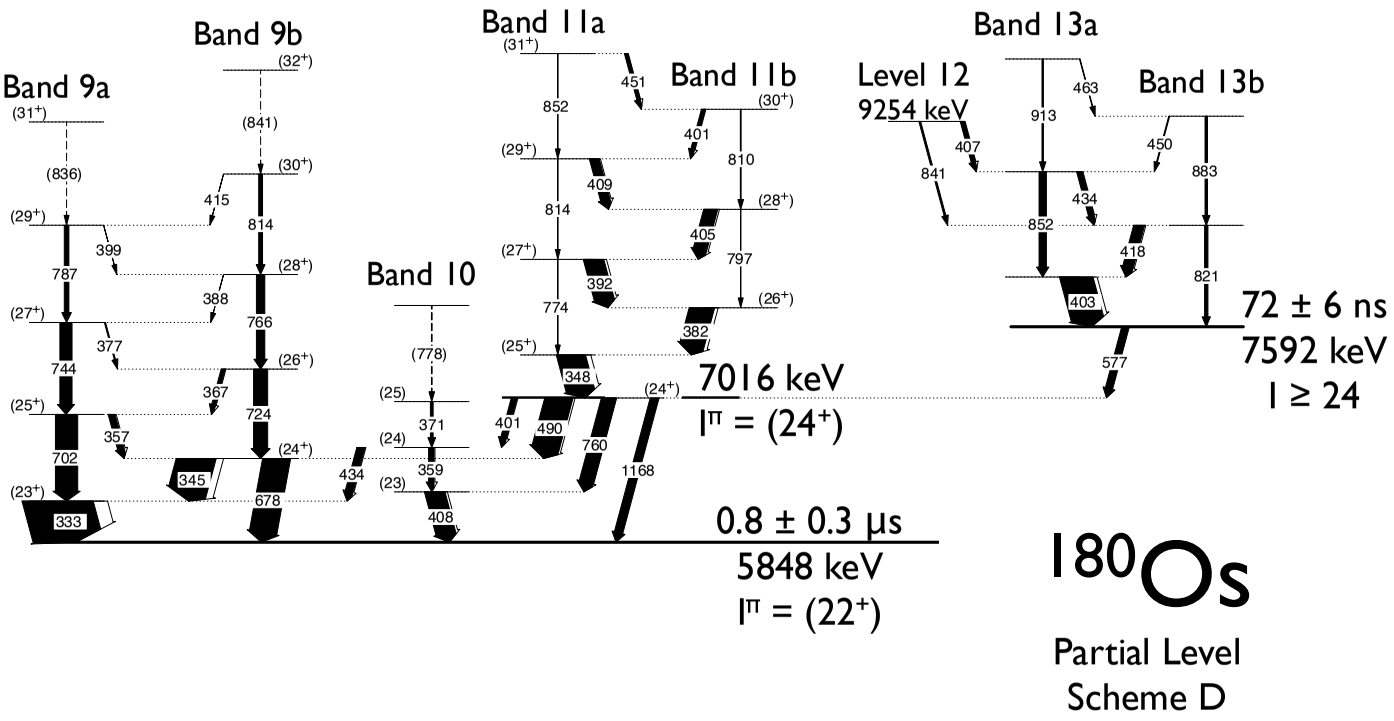

Figure 5.14: Partial Level Scheme D. A partial level scheme for ^{180}Os deduced in this work for the prompt transitions above the 5848-keV and 7592-keV isomers. Transition energies are given to the nearest keV. The widths of the arrows are proportional to the total intensity of the transition and the white sections represent the calculated internal conversion. The intensities above the 5848-keV and 7592-keV isomers are normalised individually to the 333-keV and 403-keV transitions, respectively. Tentative assignments are denoted with a dashed arrow and tentative spins are given in brackets.

Table 5.5: Energies, intensities, initial and final spins and DCO ratios for prompt γ rays in Partial Level Scheme D. The intensities are normalised to the strongest transition above each isomer and corrected for detector efficiency. A DCO ratio marked with * indicates the gate was set on a $M1$ transition.

E_γ	$J_i^\pi \rightarrow J_f^\pi$	I_γ	R^{DCO}
	Band 9a		
333.0(1)	$(23^+) \rightarrow (22^+)$	100.0(9)	0.2(1)
356.7(1)	$(25^+) \rightarrow (24^+)$	10(2)	0.4(2)
701.7(1)	$(25^+) \rightarrow (23^+)$	32(4)	2.9(1.0)*
377.3(9)	$(27^+) \rightarrow (26^+)$	2(1)	
744.3(1)	$(27^+) \rightarrow (25^+)$	18(3)	
399.0(5)	$(29^+) \rightarrow (28^+)$	0.6(6)	
787.4(2)	$(27^+) \rightarrow (27^+)$	7(2)	
836.0(8)	$(31^+) \rightarrow (29^+)$	0.1(1)	
	Band 9b		
344.9(1)	$(24^+) \rightarrow (23^+)$	56(5)	0.2(1)
678.0(1)	$(24^+) \rightarrow (22^+)$	40(4)	
367.0(1)	$(26^+) \rightarrow (25^+)$	6(2)	
723.7(2)	$(26^+) \rightarrow (24^+)$	20(3)	
388.4(1)	$(28^+) \rightarrow (27^+)$	0.9(7)	
765.7(1)	$(28^+) \rightarrow (26^+)$	12(2)	
414.5(1)	$(30^+) \rightarrow (29^+)$	1.2(4)	
813.6(2)	$(30^+) \rightarrow (28^+)$	6(2)	
840.7(4)	$(32^+) \rightarrow (30^+)$	1.6(6)	
	Band 10		
407.7(1)	$(23) \rightarrow (22^+)$	28.9(9)	
359.5(10)	$(24) \rightarrow (23)$	8(2)	
434.2(2)	$(24) \rightarrow (23^+)$	12(2)	
371.4(3)	$(25) \rightarrow (24)$	4(1)	
778.2(9)	$\rightarrow (25)$	1(1)	
	Band 11a		

Table 5.5: Continued.

E_γ	$J_i^\pi \rightarrow J_f^\pi$	I_γ	R^{DCO}
400.8(10)	$(24^+) \rightarrow (24)$	8.4(9)	
489.9(1)	$(24^+) \rightarrow (24^+)$	40(3)	
760.2(1)	$(24^+) \rightarrow (23^+)$	21(2)	
1167.9(1)	$(24^+) \rightarrow (22^+)$	12(2)	
348.3(1)	$(25^+) \rightarrow (24^+)$	41(3)	
391.9(1)	$(27^+) \rightarrow (26^+)$	29(2)	
773.6(3)	$(27^+) \rightarrow (25^+)$	1.6(8)	
409.1(2)	$(29^+) \rightarrow (28^+)$	14.0(9)	
814.1(4)	$(29^+) \rightarrow (27^+)$	0.3(7)	
450.9(1)	$(31^+) \rightarrow (30^+)$	5.0(7)	
852.0(7)	$(31^+) \rightarrow (29^+)$	2.0(6)	
Band 11b			
381.6(1)	$(26^+) \rightarrow (25^+)$	36(3)	
405.1(1)	$(28^+) \rightarrow (27^+)$	20(2)	
797.0(9)	$(28^+) \rightarrow (26^+)$	0.2(8)	
401.1(4)	$(30^+) \rightarrow (29^+)$	5.6(9)	
810.1(1)	$(30^+) \rightarrow (28^+)$	1.1(7)	
Level 12			
407.30(6)		13.1(22)	
841.1(4)		5.3(20)	
576.7(10)		11.90(12)	
Band 13a			
402.6(1)		100.0(6)	
433.8(1)		17(2)	
852.1(1)		22(3)	
463.2(10)		2(2)	
912.8(2)		4(2)	
Band 13b			
418.3(1)		33(3)	
821.0(3)		10(5)	
449.6(8)		1(1)	

Table 5.5: Continued.

E_γ	$J_i^\pi \rightarrow J_f^\pi$	I_γ	R^{DCO}
883.4(2)		8(2)	

5.3.1 Decay of the 5848-keV I^π=(22$^+$) isomer

The decay of the 5848-keV isomer was investigated in delayed $\gamma\gamma$ matrix and $\gamma\gamma\gamma$ cube, created with a gate on the prompt 333-, 345- and 678-keV γ rays above the isomer. The time difference between the prompt and delayed transitions was specified to be 150 ns $\leq \Delta T \leq$ 800 ns, with the timing of the second beam pulse at 410 ns excluded to avoid contamination.

Coincidence analysis of these matrices confirmed the decay scheme of the isomer as presented in Ref. [64]. The placement of the intermediate level at 5562 keV was further supported by the discovery of a 739-keV transition from this state to the $I = 20^+$ level of Band 1b. The spectrum produced by the double gate on the 287- and 620-keV transitions in the delayed $\gamma\gamma\gamma$ cube is shown in Fig. 5.15(a). The 739-keV γ ray can clearly be seen in this coincidence spectrum, supporting the placement in the level scheme. γ rays with energies 672, 753 and 1393 keV were also identified, in this work, to be part of the decay sequence of the 5848-keV isomer. The 672-keV γ ray decays into a new level at 4890 keV and the 753- and 1393-keV γ rays decay from this level to the 18$^+$ and 16$^+$ levels of Band 1b, respectively. The insert labelled (b) in Fig. 5.15 is the spectrum resulting from the sum of double gates (287 keV and 672 keV)/ (640 keV and 620 keV), in the delayed $\gamma\gamma\gamma$ cube, and clearly shows the 739- and 753-keV transitions.

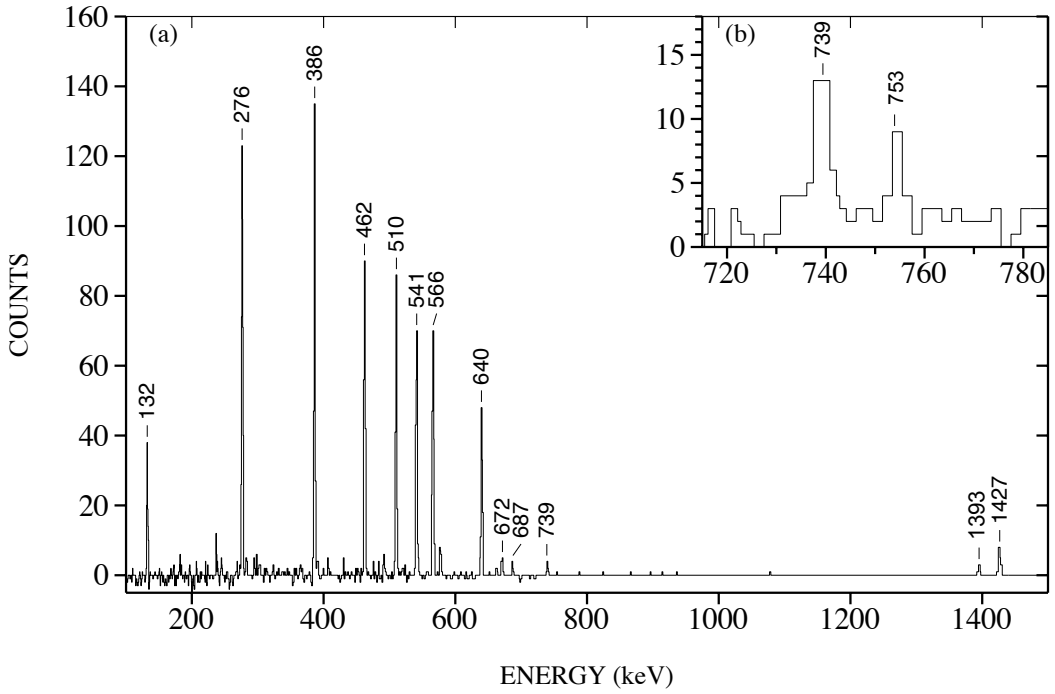

Figure 5.15: (a) A γ ray spectrum from the double gate on the 620-keV and 287-keV transitions in the delayed $\gamma\gamma\gamma$ cube for the 5848-keV isomer. (b) A section of the spectrum from the sum of double gates, (287 keV and 672 keV)/ (640 keV and 620 keV), in the same matrix to highlight the newly assigned 739- and 753-keV transitions.

Spin and parity assignment

The level at 5562-keV was tentatively assigned a spin of $I^{\pi} = (20^{+})$ based on the systematics of the decay. The 1426- and 739-keV γ rays were assigned as being $E2$ ($\Delta I = 2$) and $M1$ ($\Delta I = 0$) in nature, respectively. Higher spin assignments were not considered as transitions with a multipolarity of $L \geq 3$ would be significantly hindered. Similarly, $M2$ transitions were not considered. An spin assignment of $I^{\pi} = 18^{+}$ was also ruled out since no decays were observed to the $I^{\pi} = 16^{+}$ level of the ground-state band.

A spin assignment of $I = 19$ cannot be entirely ruled out as a possibil-

ity for the 5562-keV level. However, this would imply $M1/E1$ ($\Delta I = 1$) multipolarities for both the 739 and 1426 keV γ rays. The calculated transition probabilities for $M1/E1$ 1426-keV and 739-keV γ rays tell us that the 1426-keV γ ray would be an order of magnitude less intense than that for the 739-keV γ ray. The 1426-keV transition was measured in this work to be more intense than than the 739-keV γ ray (see Table 5.4), making the $I^{\pi} = (20^{+})$ assignment the most probable for this level.

Similarly, the level at 4890-keV was tentatively assigned a spin of $I^{\pi} = (18^{+})$ and the 672-, 753- and 1393- keV γ rays were assigned as $E2$ ($\Delta I = 2$), $M1$ ($\Delta I = 0$) and $E2$ ($\Delta I = 2$) in nature, respectively. Spin assignments of $I \leq 16$ and $I > 18$ and $M2$ transitions were ruled out based on similar logic to that presented for the 5562-keV isomer. A spin assignment of $I = 17$ was also ruled out as this would imply a $L = 3$ multiplicity for the 672-keV transition.

The multipolarity of the 287-keV transition, decaying directly from the isomeric state into the I^{π}=20^{+} state at 5562-keV, was determined using the internal-conversion method detailed in Section 4.4.2. The conversion coefficient was measured to be α= 0.13 $\pm$ 0.05, from the intensity flow through the I^{π}=20^{+} state. Table 5.6 contains the conversion coefficients calculated for the 287-keV transition. The measured value is within 1 standard deviation of the value calculated for an $E2$ transition and within 3 standard deviations of the values calculated for $E1$ and $M1$ transitions. Although it has not been possible to firmly establish the multipolarity in this work, the state has been tentatively assigned as $E2$. Spins of $I^{\pi} = 20^{+}$, 21^{+} and 22^{+} are all possible assignments for the 5848-keV isomer. The $I^{\pi} = 20^{+}$ was assigned based on the decay of the 7592-keV isomer presented in Section 5.3.3.

Table 5.6: Calculated conversion coefficients for a 287-keV γ ray.

Multipolarity	α
$E1$	0.027
$M1$	0.292
$E2$	0.104
$M2$	1.18
$E3$	0.529
$M3$	4.13
$E4$	2.96
$M4$	15.57

Half-life measurement

The analysis of the prompt-delayed matrices, with varying ranges of ΔT, suggests a half-life for the 5848-keV isomeric state of at least an order of magnitude larger than that previously measured of 12 $\pm$ 4 ns. The prompt γ-ray spectra produced from delayed 287-keV gates in the prompt-delayed matrices with 224 ns $\leq \Delta T \leq$ 336 ns and 588 ns $\leq \Delta T \leq$ 700 ns are shown in Fig. 5.16(a) and (b), respectively. The 333-, 345-, 348-, and 408-keV γ rays, identified in this work as the most intense prompt transitions for this isomer, are seen in both spectra, suggesting a half-life of the order of several hundred nanoseconds.

Obtaining an accurate measurement of the half-life was not trivial due to the low statistics and the fact that the counts were spread over a long period of time and, therefore, several interfering beam pulses. The ΔT spectrum shown in Fig. 5.17 is the result of a gate on the prompt 333-keV γ ray in the prompt-ΔT matrix, gated on the delayed 287-, 566-, 620- and 640-keV γ rays. A straight line was fitted by χ^2 minimisation to a logarithmic plot to measure the rate of exponential decay; a half-life of $T_{1/2} = 0.9 \pm 0.4$ μs was

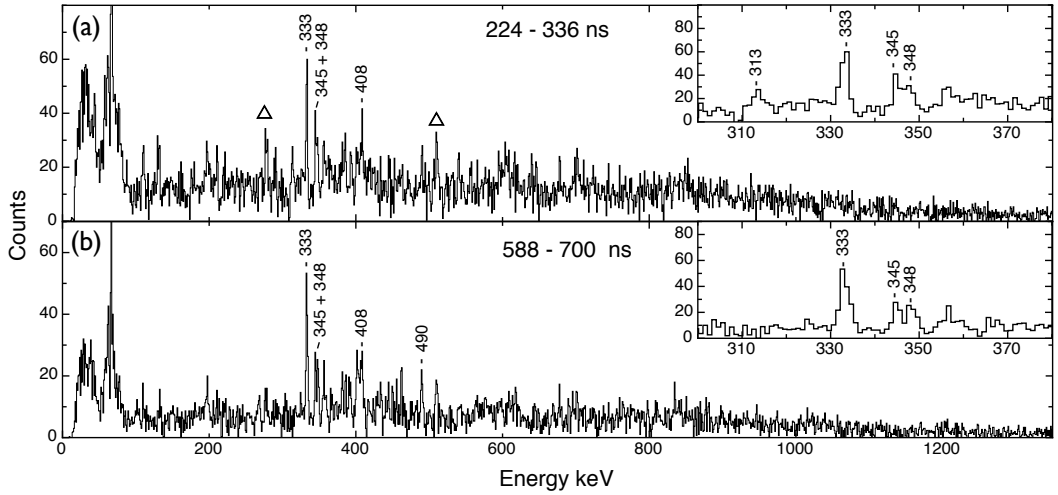

Figure 5.16: Prompt γ-ray spectra from the delayed 287-keV gate in prompt-delayed matrices with varying ΔT ranges. (a) 224 ns $\leq \Delta T \leq$ 336 ns, the open triangle denote ground-state band contaminants. (b) 588 ns $\leq \Delta T \leq$ 700 ns.

calculated. The large error was due to uncertainties in the fit created as a result of the low number of statistics in the 333-keV γ ray.

To reduce the error in the half-life for the 5848-keV isomer an additional attempt to estimate the half-life was made. The intensities of the 333-keV and 345-keV prompt γ rays were measured in the prompt spectra produced from ΔT gates in the ΔT-prompt matrix for this isomer, such as those shown in Fig. 5.16. The ranges 150 ns $\leq \Delta T \leq$ 250 ns, 250 ns $\leq \Delta T \leq$ 350 ns, 550 ns $\leq \Delta T \leq$ 650 ns and 650 ns $\leq \Delta T \leq$ 750 ns were selected as they give clean spectra and sufficient statistics to measure the 333- and 345-keV γ ray peaks. A straight line was fitted by χ^2 minimisation to the logarithmic plots of the intensities for both the 333- and 345-keV photopeaks. Half-lifes of $T_{1/2} = 0.8 \pm 0.3$ μs and $T_{1/2} = 0.7 \pm 0.3$ μs were extracted for the 333- and 345-keV peaks, respectively. The results of the individual fits are shown in

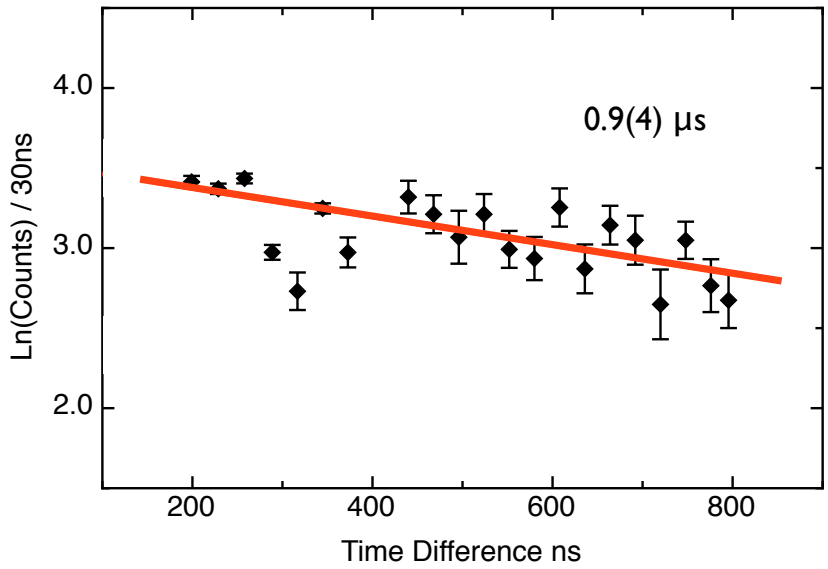

Figure 5.17: [Colour] A ΔT spectrum from the prompt 333-keV gate in the ΔT-prompt matrix for 5848-keV isomer gated on the 287-, 566-, 620- and 640-keV delayed γ rays. The counts shown are per 30 ns. The red line represents a decay with a half-life of 0.9 μs.

Fig. 5.18. The mean half life calculated with this method is $T_{1/2} = 0.8 \pm 0.3$.

5.3.2 Bands above the 5848-keV isomer

The prompt γ rays above the 5848-keV isomeric state were first identified in the γ-ray spectrum produced by the 287-keV delayed gate in the prompt-delayed matrix, with the prompt-delayed coincidence range of 150 ns $\leq \Delta T \leq$ 800 ns. Partial Level Scheme D in Fig. 5.14 shows the 5 bands identified as the prompt structure for the 5848-keV isomer. This level scheme was established through the analysis of the prompt $\gamma\gamma$ matrix and $\gamma\gamma\gamma$ cube produced to contain only prompt transitions in coincidence with the 287-, 640-, 620- and 566-keV delayed γ rays. The time difference between the prompt and delayed γ rays was specified to have the range 150 ns $\leq \Delta T \leq$ 800 ns.

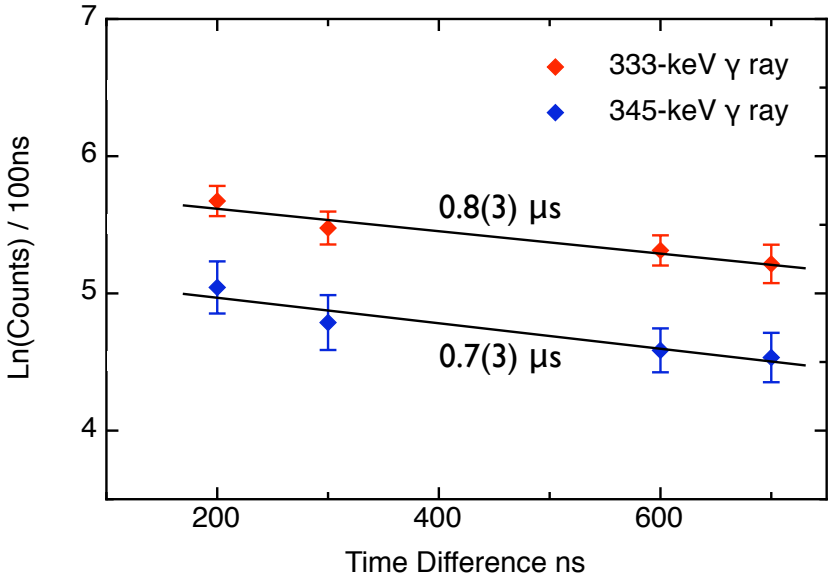

Figure 5.18: [Colour] A plot of the intensities in the 333-keV (red) and 345-keV (blue) peaks in 100-ns ΔT gates in the prompt-ΔT matrix for the 5848-keV isomer gated on the 287-, 566-, 620- and 640-keV delayed γ rays. The black lines represent the half-life fits for each respective data set.

The spin and parity assignments for all the levels above the 5848-keV isomer are based on the tentative assignment of $I^{\pi} = (22^{+})$ for the isomeric state.

Bands 9a and 9b

The spectrum shown in Fig. 5.19 (a) contains the transitions assigned to bands 9a and 9b. This spectrum was created from the sum of gates on the 333-, 345-, 678-, 702-, 724-, 744-, 766-, 787- and 814-keV γ rays in the prompt $\gamma\gamma$ matrix for this isomer. The ordering of the transitions for bands 9a and 9b was based on the intensities of coincident transitions in the individual gates for each γ ray and on the observation of strong inter-band transitions. Transitions allocated to several of the other prompt bands for this isomer

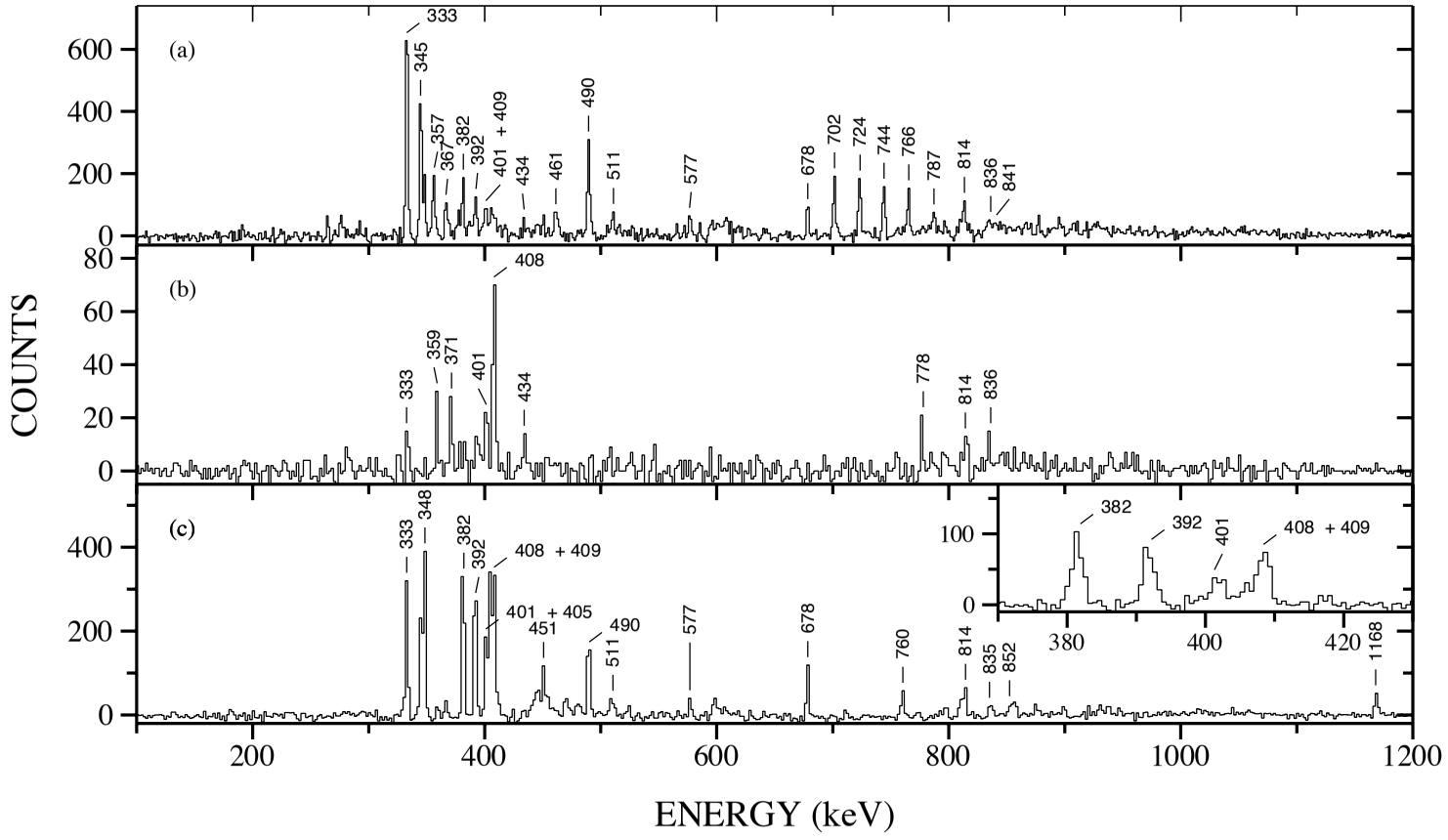

Figure 5.19: Spectra from gates in the prompt $\gamma\gamma$ matrix for the 5848-keV isomer. Details of the matrix are given in the text. (a) The sum of gates on the 333-, 345-, 678-, 702-, 724-, 744-, 766-, 787- and 814-keV γ rays, (b) The sum of gates on the 359- and 371-keV γ rays. (c) The sum of gates on the 348-, 382-, 392-, 405-, 409-, 490-, 760- and 1168-keV γ rays.

are also seen in this spectrum as they feed into the lower levels of these two bands. The γ ray at 461 keV could not be placed in this work.

DCO ratios were measured for the 333- and 356-keV transitions from Band 9a and the 345-keV transition from Band 9b. This was achieved from the sum of gates on transitions within bands 9a and 9b, respectively. The measured DCO ratios for the 333-, 345- and 356-keV transitions were measured as 0.2 $\pm$ 0.1, 0.2 $\pm$ 0.1 and 0.4 $\pm$ 0.2, respectively. If the transitions belonging to bands 9a and 9b are considered to be E2 transitions this would suggest dipole (ΔI=1) transitions. Due to the limited statistics, it was only possible to measure the DCO ratio for the 702-keV γ ray in Band 9a. The DCO ratio was measured as 2.9 $\pm$ 1.0 with the coincidence gate set on the 333-keV dipole transition. This further supports the quadrupole (ΔI= 2) nature for the 702-keV transition.

Band 10

The spectrum shown in Fig. 5.19 (b) was produced by the sum of gates on the 359- and 371-keV γ rays, allocated to Band 10, in the prompt $\gamma\gamma$ matrix for the 5848-keV isomer. The 408-keV γ ray, clearly seen in this spectrum, was assigned as the transition from the band-head of Band 10 directly into the isomeric state. A decay into the band head of Band 9a was also observed with an energy of 434 keV and was confirmed by the observation of the 333-keV transition in this spectrum. The 401-keV γ ray was positioned as the decay from the band head of Band 11a to Band 10. The 778-keV γ ray was tentatively assigned as an extension to Band 10. The γ rays at 814 and 836 keV are possibly those γ rays in bands 9b and 9a and point to some unobserved feeding between these levels.

The spins tentatively assigned to levels in Band 10 are based on the systematic of the decays from bands 11a and 11b. The 401- and 490-keV transitions were assigned to be ΔI=0 and ΔI=1 dipole transitions, giving a band head with spin I=23 and a dipole multipolarity of the 359-keV transition. It was not possible to measure the DCO ratios for the transitions in this band due to low statistics.

Bands 11a and 11b

Bands 11a and 11b were established to be based on a band head at 7016 keV. The transitions associated with bands 11a and 11b are seen in Fig. 5.19 (c). This spectrum was produced by the sum of gates on the 348-, 382-, 392-, 405-, 409-, 490-, 760- and 1168-keV γ rays associated with these bands. The ordering of the transitions in bands 11a and 11b was based on the strong inter band transitions and intensity relationships in the individual γ-ray gates in the prompt $\gamma\gamma$ matrix for this isomer. The transitions with energies of 401-, 760- and 490-keV were allocated as decaying from the band head into two levels of Band 10 and Band 9b, respectively. The subsequent 333-, 345- and 678-keV transitions are also seen in this spectrum supporting this placement. A 1168-keV γ ray was observed as feeding directly from the band head to the 5848-keV isomeric state. The 577-keV transition in this spectrum was found to decay from the isomeric state at 7592 keV. The decay of this isomer is discussed further in the following section. It should also be noted that the γ rays observed in the spectrum at 511 and 835 keV could not be placed in the level scheme due to the low intensities of these transitions in the individual gates.

A spin and parity of $I^{\pi} = (24^{+})$ was tentatively assigned for the band

head of bands 11a and 11b at 7016-keV. This was determined by the presence of the 1168-keV transition. A transition with $L \geq 3$ would be significantly hindered compared to the other transitions from the band head. The multipolarities for the 1168- and 490-keV transitions were therefore determined to be $E2$ (ΔI=0) and $M1$ (ΔI=0), respectively. The spins and parities for the levels in bands 11a and 11b were based on this band-head spin assignment. It was not possible to measure the DCO ratios for any transitions on this band, however spins were assigned based on the observation of strong linking transitions.

5.3.3 Decay of the 7592-keV isomer

The decay sequence of the 7592-keV isomer was studied in the delayed $\gamma\gamma$ matrix and $\gamma\gamma\gamma$ cube, created to contain only those delayed transitions in coincidence with the prompt 403-, 418-, 434- and 852-keV γ rays above the isomer. The time difference between the prompt and delayed transitions was limited to 50 ns $\leq \Delta T \leq$ 150 ns.

Analysis of these matrices identified a complex decay sequence for this isomer. It was established that the isomer decays solely through a 577-keV γ ray to the band-head state of bands 11a and 11b at 7016 keV. The spectrum shown in panel (a) of Fig. 5.20 was produced from the gate on the 577-keV γ ray in the delayed $\gamma\gamma$ matrix for this isomer. This spectrum clearly shows the low-lying transitions, expected from the decay from the band-head state, at 333, 407, 489, 760 and 1168 keV.

The 620- and 640-keV γ-ray transitions between states in Band 1b and the transitions belonging to the ground-state band are also strongly populated in this spectrum. The coincidences between the delayed transitions in the

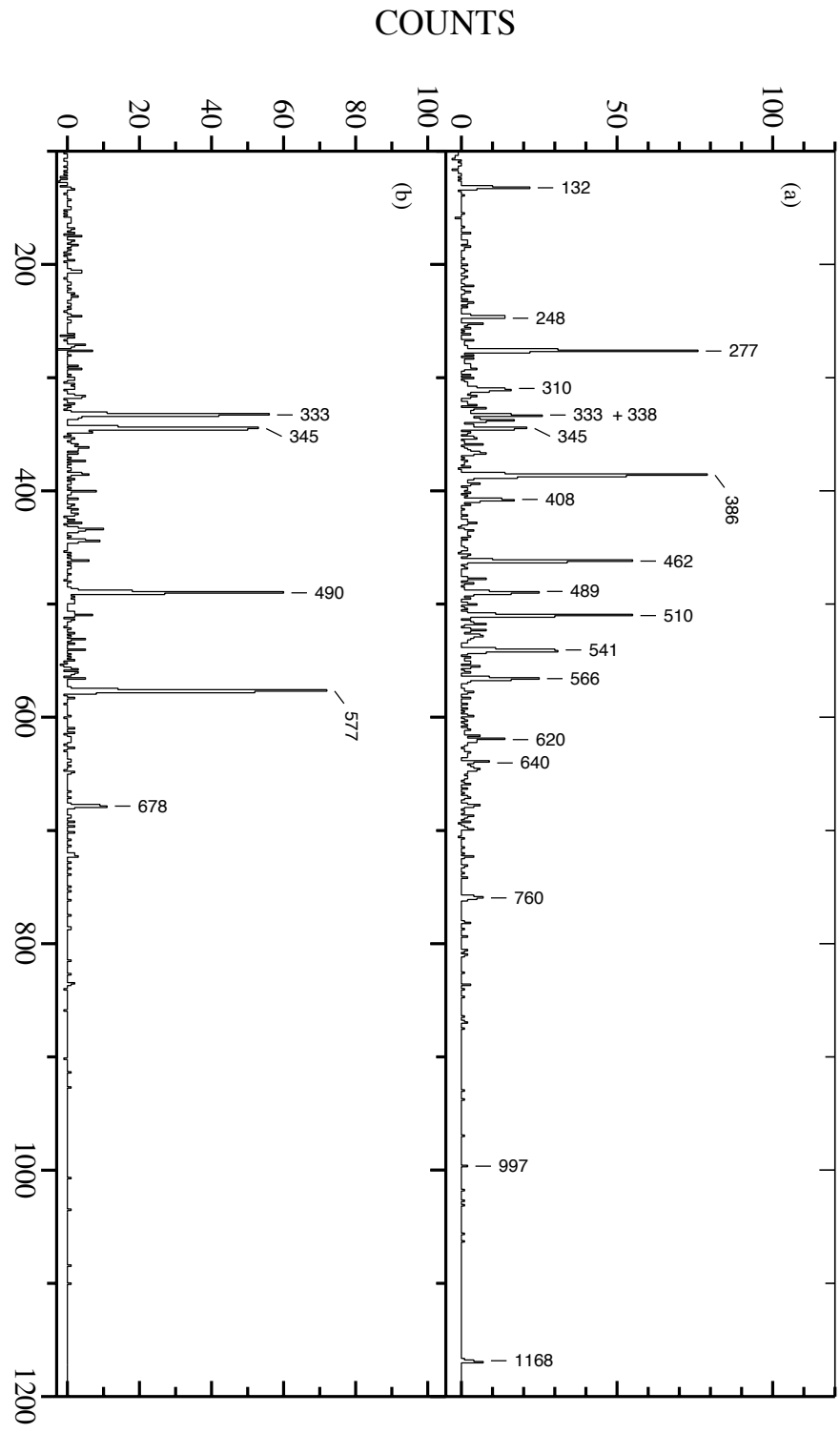

Figure 5.20: Spectra supporting the placement of the 7592-keV isomer, produced from gates in the delayed $\gamma\gamma$ matrix for the 7592-keV isomer. (a) Spectrum produced from the coincidence gate on the 577-keV γ ray. (b) Spectrum produced from the sum of coincidence gates on the 333-, 345- and 490-keV γ rays.

matrix were limited to 12 ns, removing the possibility that these γ-ray peaks were produced through the decay of the 5848-keV 0.8-μs isomer. The γ rays at 248, 310, 338 and 997 keV were identified as part of the fragmented decay scheme bypassing the 5848-keV isomeric state.

The decay of the 7592-keV isomer into the prompt bands above the 5848-keV isomer was further confirmed in the spectrum shown in Fig. 5.20(b). This spectrum was produced by the sum of the coincidence gates on the 333-, 345- and 490-keV γ rays, in the delayed $\gamma\gamma$ matrix. Only the transitions above the 5848-keV isomer are seen in this spectrum confirming the blocking of delayed coincidences across the isomeric state. The prompt transitions above the 5848-keV isomer are also restricted to only those populated via the 577-keV transition in the decay of the higher energy isomer. This supports the position of the the 577-keV γ ray and subsequently the 7592-keV isomer. Further evidence of the position of the 7592-keV isomer is given by the spectrum in Fig. 5.21 (a), showing the coincidence gate on the 760-keV γ ray. It clearly shows the 408- and 577-keV transitions in the coincidence with the 760-keV γ ray, as expected from the level scheme. The spectrum in Fig. 5.21 (b) shows the sum of gates on the 310- and 338-keV transitions, identified as part of the fragmented decay scheme for the 7592-keV isomer into Band 1a. The spectrum shows clear coincidences with transitions in the ground-state band. Further coincidence analysis established that both bands 1a and 1b were populated from the decay of the 7592-keV isomer and transitions below the $I^{\pi} = 24^{+}$ and $I^{\pi} = 26^{+}$ states, respectively were observed in the delayed $\gamma\gamma$ matrix for the isomer. Band 3 is also found to be populated weakly by the decay of this isomer. The fragmented decay into these bands could not be fully established and the tentative placement of transitions into

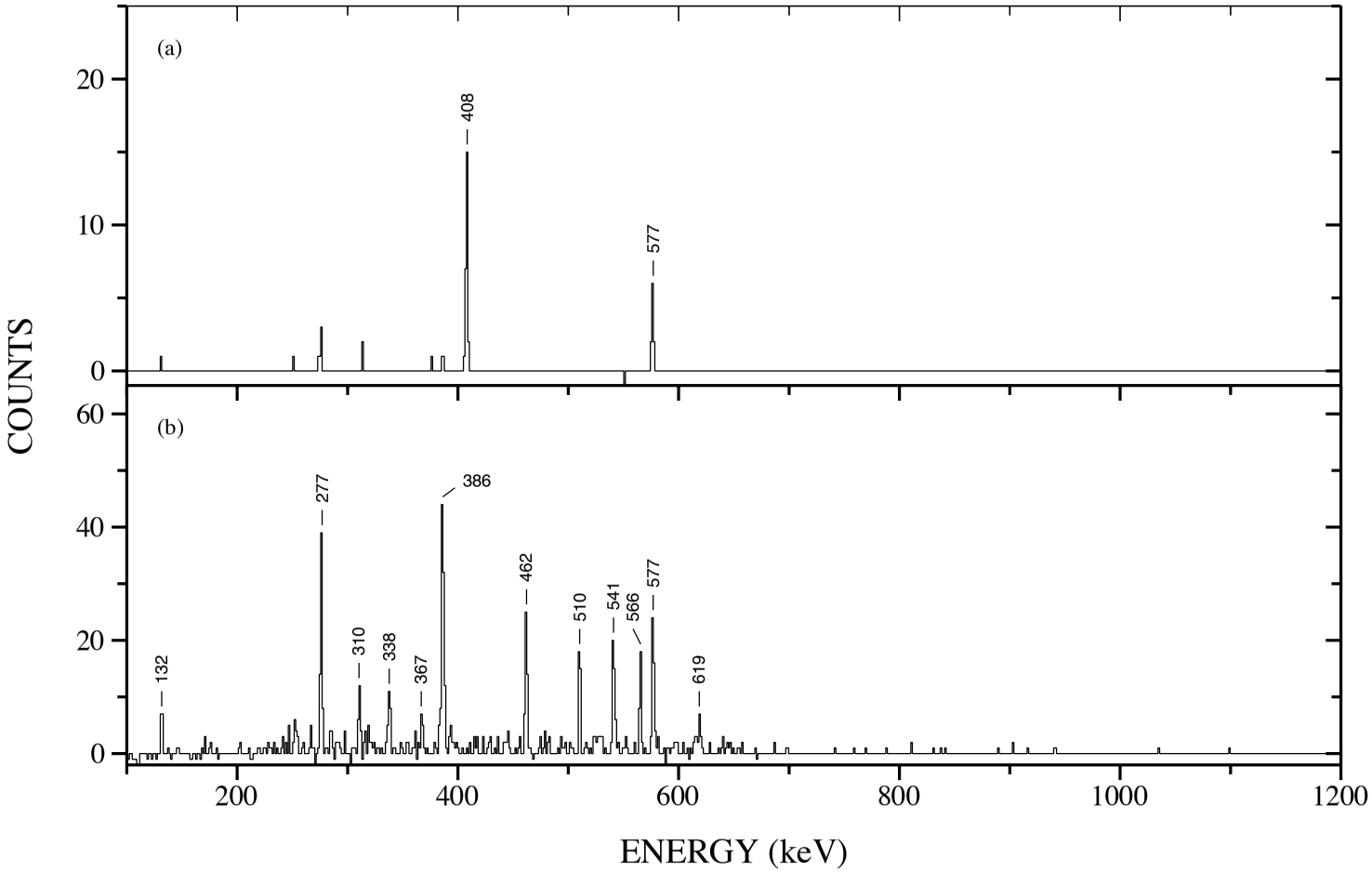

Figure 5.21: Spectra supporting the placement of the 7592-keV isomer, produced from gates in the delayed $\gamma\gamma$ matrix for the 7592-keV isomer. (a) Spectrum produced from the coincidence gate on the 760-keV γ ray. (b) Spectrum produced from the sum of coincidence gates on the 310-keV and 338-keV γ rays.

these bands was based solely on energy differences.

Spin and parity assignment

It was not possible to measure the multipolarity of the 577-keV transition in this work. The measurement of the internal conversion coefficient for this γ ray cannot be measured as it is approximately zero for any multipolarity of transition. A limit on the spin assigned to the 7592-keV isomer of $I > 24$ was based on the direct decay into the $I^{\pi} = (24^{+})$ 7016-keV level.

The decay of the 7592-keV isomer into the band head of bands 11a and 11b and the high-spin states of bands 1b and 1a provided information on the spin of the 5848-keV isomer. The spin assignments $I^{\pi} = (20^{+})$, (21^{+}) and (22^{+}) were all options for the 5848-keV state. By assigning the isomer as spin $I^{\pi} = (22^{+})$, the 7016-keV state subsequently has a spin of $I^{\pi} = (24^{+})$. It is then feasible that the isomer decays into the $I^{\pi} = 24^{+}$ and $I^{\pi} = 26^{+}$ states of bands 1a and 1b, respectively, via the 7016-keV state.

Half-life measurement

The half life of the 7592-keV isomer was investigated in the ΔT-prompt matrix, gated on the 577-keV delayed transition decaying directly from the isomeric state. ΔT spectra were produced from gates on the prompt 403-, 418-, 434-, 821- and 852-keV γ rays established for this isomer. A function of the form in Equation 4.8 was fitted to each decay curve by χ^2 minimization, and a mean half life of $T_{1/2} = 72 \pm 6$ ns was extracted. The sum of the ΔT spectra used to measure the half life is shown in Fig. 5.22 with a decay curve of half-life $T_{1/2} = 72$ ns shown by the red line.

The half-life of the isomer predicted in the study by Venkova *et al.* [64]

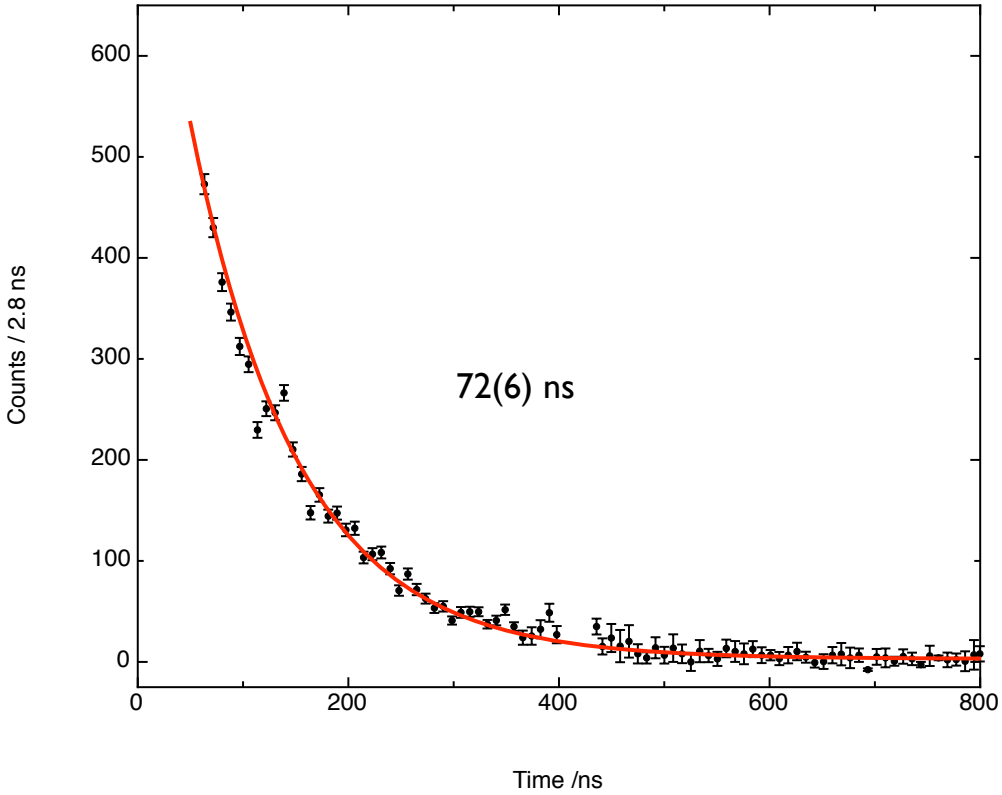

Figure 5.22: [Colour] The ΔT spectrum for the 7592-keV isomer produced from the sum of 5 individual ΔT spectra. These time spectra were produced from gates on 5 prompt γ rays, with energies 403-, 418-, 434-, 821- and 852-keV, in the prompt-ΔT matrix gated on the delayed 577-keV γ ray. The number of counts is given per 2.8 ns (5 channels). The red line shows the exponential decay curve with $T_{1/2} = 72$ ns.

was $T_{1/2} = 41 \pm 10$ ns and is within 3σ of the half life measured in this work. The half-life for an unknown isomer in the study by Pederson *et al.* [66] was estimated to be approximately 130 ns and does not agree with the half-life measured in this work for the 7952-keV isomer. It is possible that the long-lived components of the ground-state band transitions that produced this estimate, were due to the decay of the 5848-keV 0.8-μs isomer.

5.3.4 Bands above the 7592-keV isomer

The prompt structure of the 7292-keV isomer was investigated in the prompt $\gamma\gamma$ matrix created to have coincidences with the delayed 577-keV γ ray. The time difference between prompt and delayed transitions was limited to the range 50 ns $\leq \Delta T \leq$ 150 ns.

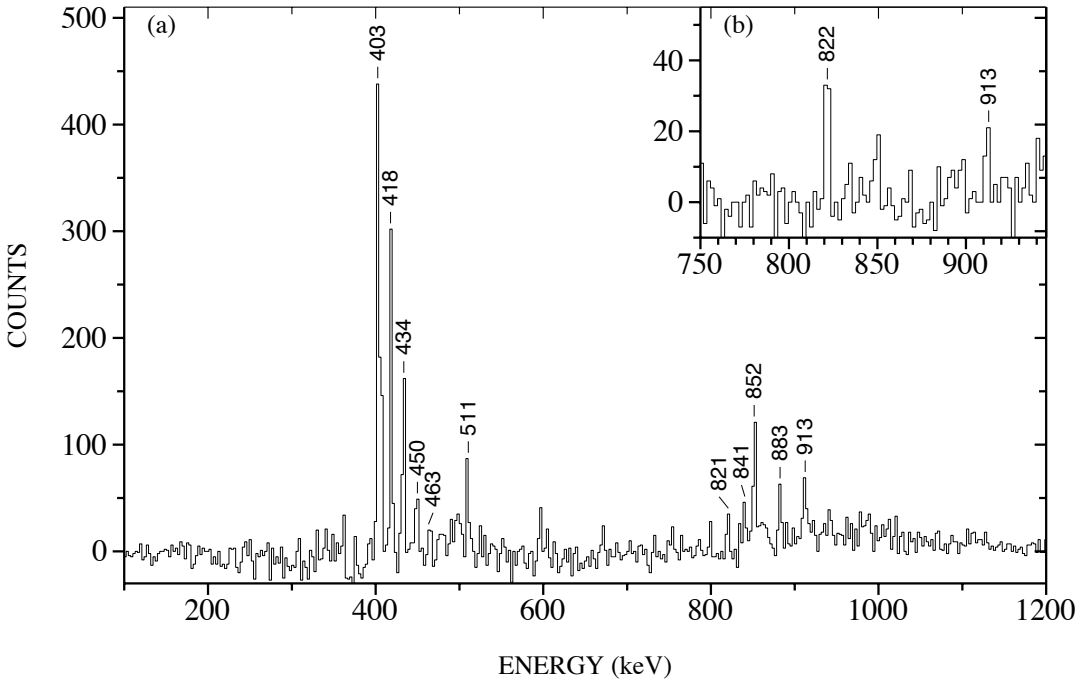

Figure 5.23: γ-ray coincidence spectra showing the transitions above the 7592-keV isomer, produced by the sum of gates in the prompt $\gamma\gamma$ matrix, gated on the 577-keV delayed transition. (a) A spectrum produced by the sum of gates on the 403-, 418-, 434-, 821-, 883- and 852-keV γ rays. (b) A spectrum produced by the sum of gates on the 434- and 883-keV γ rays.

Level 12 and bands 13a and 13b

The two bands established in this work to be above the 7952-keV isomer are presented in Partial Level Scheme D. The γ-ray coincidence spectrum created from the sum of gates on the 403-, 418-, 434-, 821-, 883- and 852-keV γ rays belonging to bands 13a and 13b are shown in Fig. 5.23. All the transitions belonging to Bans 13a and 13b can be observed in this spectrum, along with the 841-keV transition decaying into Band 13b from a level at 9254 keV, labelled as Level 12. A 407-keV γ ray was also identified to decay from Level 12 to Band 13a. The ordering and placement of the level scheme presented was based on further coincidence analysis of the prompt $\gamma\gamma$ matrix for this isomer and the intensities of the γ-ray photopeaks in the individual coincidence spectra.

It was not possible to measure the DCO ratios for the transitions in bands 13a and 13b, due to limited statistics. It can be assumed that the multipolarities within the bands are $E2$ ($\Delta I = 2$) and the inter-band transitions are $M1$ or mixed $M1/E2$ ($\Delta I = 1$) in nature. It is probable that the 407- and 841-keV are $M1$ ($\Delta I =$) and $E2$ ($\Delta I = 2$) in nature. However, no information on the lifetime of the state could be obtained so any tentative assignments of multipolarities must be treated with caution.

Chapter 6

Discussion

The quasiparticle configurations and structure for the prompt bands in Partial Level Schemes A and B have been interpreted in terms of the aligned angular momentum and Cranked Shell Model (CSM). The excitation energies of the intrinsic states are compared to those predicted by the BCS calculations. Where possible, $|\frac{g_K - g_R}{Q_0}|$ values have been calculated and compared to those predicted for the assignment of quasiparticle configurations.

The isomeric states are discussed in terms of reduced transition probabilities, K hinderance and the possible multi-quasiparticle configurations. The structures established above the two high-K isomers are discussed in terms of aligned angular momentum and the Shell Corrected Tilted Axis Cranking (SCTAC) calculations. The possible modes of excitation above the high-K isomers are investigated.

6.1 Total Routhian Surfaces

Total Routhian Surface (TRS) calculations were performed for ^{180}Os over a range of rotational frequencies [67]. The deformation parameters for $\hbar\omega$ =0 MeV were calculated as $\beta_2 = 0.222$, $\gamma = 0.2$ and $\beta_4 = -0.028$ and the TRS plot is shown in Fig. 6.1.

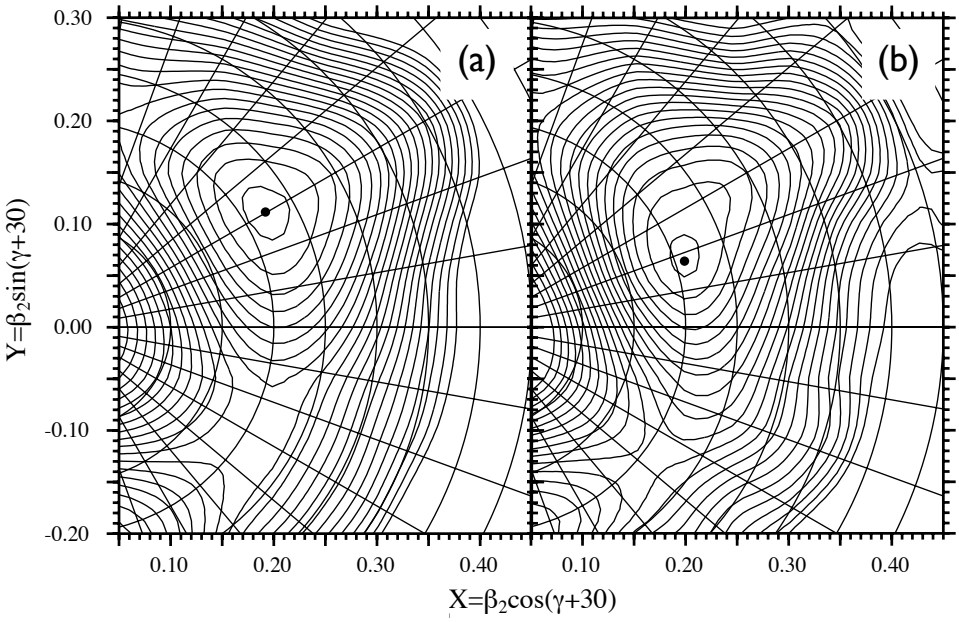

Figure 6.1: TRS plots for ^{180}Os at (a) $\hbar\omega = 0$ MeV and (b) $\hbar\omega = 0.25$ MeV, where the contours represent an energy difference of 200 keV. The minima occur at $\beta_2 = 0.222$, $\gamma = 0.2$ and $\beta_4 = -0.028$ and $\beta_2 = 0.209$, $\gamma = -12.1$ and $\beta_4 = -0.040$, respectively.

At a $\hbar\omega = 0.25$ MeV the deformation parameters were calculated as $\beta_2 = 0.209$, $\gamma = -12.1$ and $\beta_4 = -0.040$. A significant difference in the γ parameter from the $\hbar\omega = 0$ MeV minimum suggests a degree of γ softness in the nucleus. The potential well in the direction of the γ-deformation parameter is shallow, particularly at higher rotational frequencies, indicating a susceptibility to γ vibrations and triaxiality.

6.2 Cranked-shell model calculations

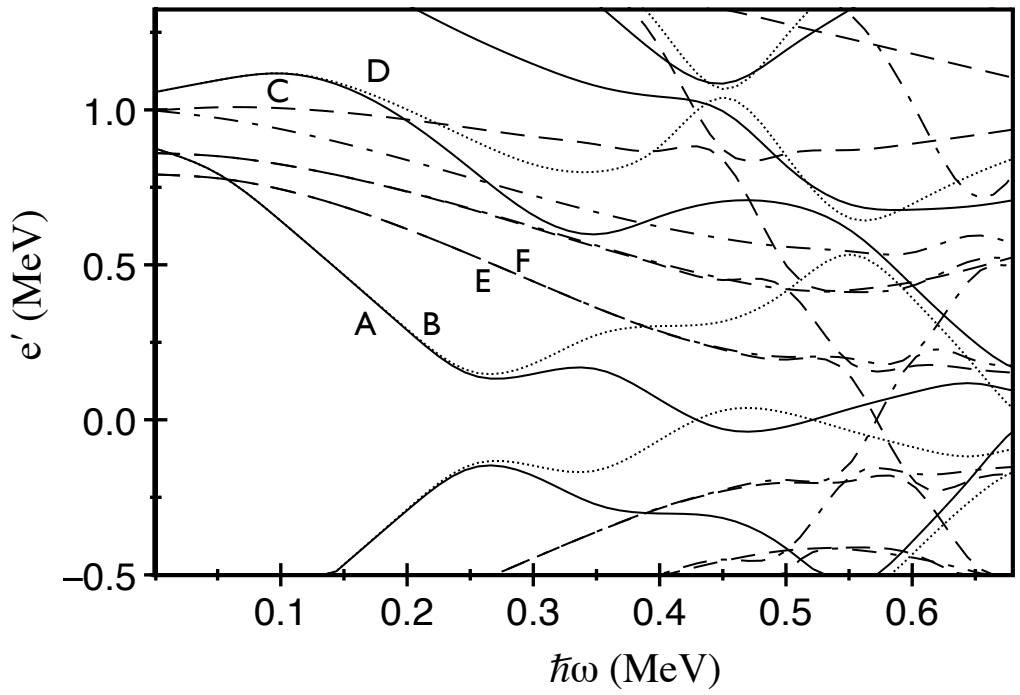

Figure 6.2: Theoretical quasineutron Routhians for ^{180}Os as predicted by CSM calculations performed with deformation parameters $\beta_2 = 0.222$, $\gamma = 0.2$ and $\beta_4 = -0.028$. Solid lines refer to (π, α)=(+, +1/2), dotted lines refer to (π, α)=(+, -1/2), dashed lines refer to (π, α)=(-, -1/2), and dash-dotted lines denote (π, α)=(-, -1/2).

In order to understand the properties of the prompt bands of ^{180}Os presented in this work, CSM calculations were performed as described in Section 2.3. The CSM calculations were performed using the deformation parameters $\beta_2 = 0.222$, $\gamma = 0.2$ and $\beta_4 = -0.028$ as extracted from the $\hbar\omega = 0$ MeV TRS calculations. The calculated quasiparticle Routhians, e', of the quasineutron and quasiproton orbitals are plotted, as a function of the rotation frequency $\hbar\omega$, in Figs 6.2 and 6.3, respectively.

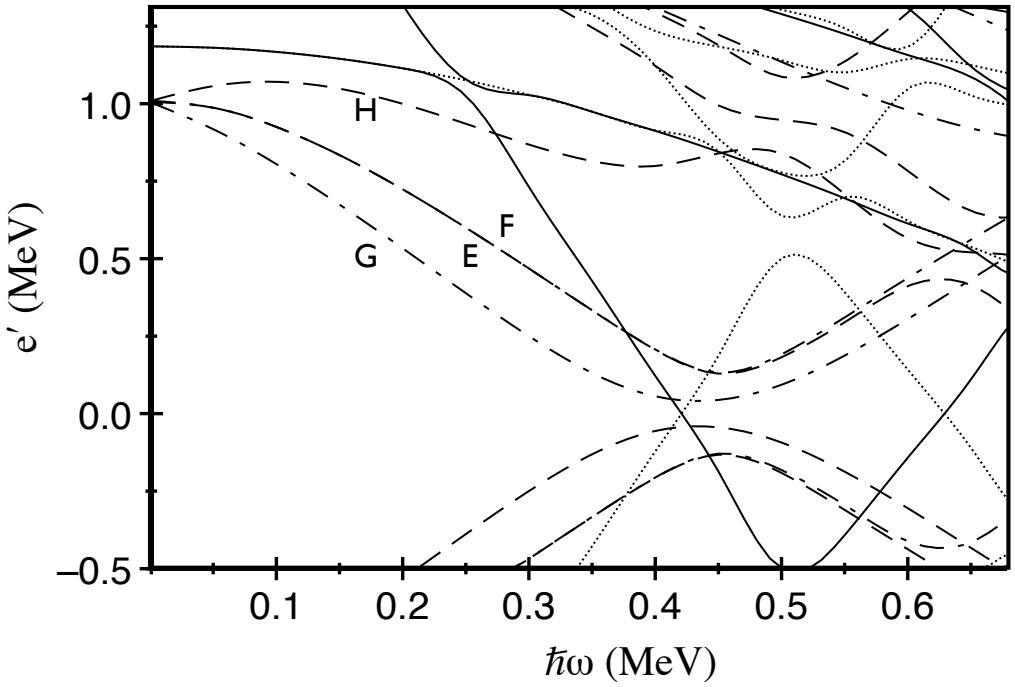

Figure 6.3: Theoretical quasiproton Routhians for ^{180}Os as predicted by CSM calculations performed with deformation parameters $\beta_2 = 0.222$, $\gamma = 0.2$ and $\beta_4 = -0.028$. Solid lines refer to (π, α)=(+, +1/2), dotted lines refer to (π, α)=(+, -1/2), dashed lines refer to (π, α)=(-, -1/2), and dash-dotted lines denote (π, α)=(-, -1/2).

The orbitals are labeled in terms of the only quantum numbers that are conserved in a rotating system, parity, π and signature, α. The standard convention, described in Ref. [68] is used in this thesis. The positive-parity orbitals closest to the Fermi surface are given the labels A and B and refer to the positive and negative signatures, (π,α) = (+, +1/2)$_1$ and (+, -1/2)$_1$, respectively. C and D refer to the next positive-parity states, (π,α) = (+, +1/2)$_2$ and (+, -1/2)$_2$, respectively. The negative-parity orbitals closest to the Fermi surface are given the labels E and F referring to the negative and positive signatures, (π,α) = (-, -1/2)$_1$ and (-, +1/2)$_1$, respectively. G and H

refer to the next negative-parity orbitals, (π,α) = (-, -1/2)$_2$ and (-, +1/2)$_2$, respectively.

The neutron orbitals closest to the Fermi surface are the negative-parity orbitals E and F, originating from the $\frac{7}{2}$[514] orbital. Although this Nilsson configuration is valid at $\hbar\omega = 0$ MeV, the Nilsson quantum numbers are not conserved in a rotating nucleus and other negative parity orbitals near the Fermi surface maybe mixed into this configuration for $\hbar\omega > 0$ MeV. Similarly, the orbitals labelled G and H are dominated by the $\frac{1}{2}$[521] Nilsson configuration [63]. The positive-parity quasineutron orbitals assigned as A, B, C and D are derived from the $i_{13/2}$ Nilsson orbitals closest to the Fermi surface. Orbitals A and B are dominated by the $\frac{7}{2}$[633] configuration and C and D may be based on the $\frac{9}{2}$[624] or $\frac{5}{2}$[642] Nilsson orbitals. The quasiproton orbitals closest to the Fermi surface are E and F and are based on the $h_{11/2}$ Nilsson configurations. G and H are based on Nilsson orbitals originating from the $h_{9/2}$ shell.

The band crossings and gains in aligned angular momentum predicted by the CSM calculations are summarised in Table 6.1.

Configuration	$\hbar\omega_c$ (MeV)	Δi_x ($\hbar$)
ν AB	0.26	≈ 7
ν BC	0.34	≈ 6
ν AD	0.35	≈ 4
ν CD	0.45	≈ 4
ν EF	0.46	≈ 4
π EF	0.45	≈ 6
π GH	0.46	≈ 5

Table 6.1: Predicted quasiparticle crossing frequencies $\hbar\omega_c$, and gains in aligned angular momentum Δi_x from the CSM calculations in Figs. 6.2 and 6.3.

6.3 Blocked BCS calculations

The properties of the high-K states presented in this thesis are interpreted using Blocked BCS calculations. Blocked BCS calculations were performed for ^{180}Os using monopole pairing strengths of G_n=21.0/A MeV and G_p=22.0/A MeV for neutrons and protons, respectively [69]. The deformation parameters $\epsilon_2 = 0.217$ and $\epsilon_4 = 0.053$ were taken from Reference [70]. The results of the blocked BCS calculations are given in Table 6.2 along with the predicted value of $|\frac{g_K - g_R}{Q_0}|$ for each multi-quasiparticle configuration (see Section 4.4.3).

Table 6.2: The excitation energy for multi-quasiparticle states predicted by blocked BCS calculations and predicted values of $\frac{g_K - g_R}{Q_0}$ for each multi-quasiparticle configuration.

K^π	E^* (keV)	ν	π	$\lvert\frac{g_K - g_R}{Q_0}\rvert$
		2ν 0π		
6^+	1625	$\frac{7}{2}[514]$ $\frac{5}{2}[512]$		-0.050
4^+	1665	$\frac{7}{2}[514]$ $\frac{1}{2}[521]$		0.045
8^-	1875	$\frac{7}{2}[514]$ $\frac{9}{2}[624]$		-0.013
7^-	1704	$\frac{7}{2}[514]$ $\frac{7}{2}[633]$		-0.036
6^-	2419	$\frac{7}{2}[514]$ $\frac{5}{2}[642]$		-0.005
7^-	1858	$\frac{5}{2}[512]$ $\frac{9}{2}[624]$		-0.064
6^-	2190	$\frac{5}{2}[512]$ $\frac{7}{2}[633]$		-0.069
5^-	1890	$\frac{1}{2}[521]$ $\frac{9}{2}[624]$		-0.002
8^+	1923	$\frac{9}{2}[624]$ $\frac{7}{2}[633]$		-0.023
		0ν 2π		
7^-	2432		$\frac{5}{2}[402]$ $\frac{9}{2}[514]$	0.173
8^-	2406		$\frac{5}{2}[402]$ $\frac{11}{2}[505]$	0.166
10^+	2556		$\frac{9}{2}[514]$ $\frac{11}{2}[505]$	0.156
		4ν 0π		
11^-	2866	$\frac{7}{2}[514]$ $\frac{5}{2}[512]\frac{1}{2}[521]$ $\frac{9}{2}[624]$		-0.019

Table 6.2: Continued.

K^π	E^* (keV)	ν	π	$\left\vert\frac{g_K-g_R}{Q_0}\right\vert$
14^+	2909	$\frac{7}{2}[514]\ \frac{5}{2}[512]\frac{9}{2}[624]\ \frac{7}{2}[633]$		-0.023
13^+	3664	$\frac{7}{2}[514]\ \frac{9}{2}[512]\frac{9}{2}[624]\ \frac{5}{2}[642]$		-0.023
12^+	2952	$\frac{7}{2}[514]\ \frac{1}{2}[521]\frac{9}{2}[624]\ \frac{7}{2}[633]$		-0.009
14^-	3750	$\frac{7}{2}[514]\ \frac{9}{2}[624]\frac{7}{2}[633]\ \frac{5}{2}[642]$		-0.004
14^+	4059	$\frac{7}{2}[514]\ \frac{9}{2}[624]\frac{7}{2}[633]\ \frac{5}{2}[523]$		-0.004
		$2\nu\ 2\pi$		
18^-	4432	$\frac{7}{2}[514]\ \frac{9}{2}[624]$	$\frac{9}{2}[514]\ \frac{11}{2}[505]$	-0.088
17^-	4261	$\frac{7}{2}[514]\ \frac{7}{2}[633]$	$\frac{9}{2}[514]\ \frac{11}{2}[505]$	-0.096
18^+	4479	$\frac{9}{2}[624]\ \frac{7}{2}[633]$	$\frac{9}{2}[514]\ \frac{11}{2}[505]$	-0.091
		$4\nu\ 2\pi$		
21^-	5422	$\frac{7}{2}[514]\frac{5}{2}[512]\frac{1}{2}[521]\frac{9}{2}[624]$	$\frac{9}{2}[514]\frac{11}{2}[505]$	0.071
21^-	5341	$\frac{7}{2}[514]\frac{5}{2}[512]\frac{9}{2}[624]\frac{7}{2}[633]$	$\frac{5}{2}[402]\frac{9}{2}[514]$	0.051
22^-	5315	$\frac{7}{2}[514]\frac{5}{2}[512]\frac{9}{2}[624]\frac{7}{2}[633]$	$\frac{5}{2}[402]\frac{11}{2}[505]$	0.100
24^+	5465	$\frac{7}{2}[514]\frac{5}{2}[512]\frac{9}{2}[624]\frac{7}{2}[633]$	$\frac{9}{2}[514]\frac{11}{2}[505]$	0.062
23^-	5829	$\frac{7}{2}[514]\frac{5}{2}[512]\frac{9}{2}[624]\frac{7}{2}[633]$	$\frac{7}{2}[404]\frac{11}{2}[505]$	0.042
22^+	5508	$\frac{7}{2}[514]\frac{1}{2}[521]\frac{9}{2}[624]\frac{7}{2}[633]$	$\frac{9}{2}[514]\frac{11}{2}[505]$	0.088
24^-	6306	$\frac{7}{2}[514]\frac{9}{2}[624]\frac{7}{2}[633]\frac{5}{2}[642]$	$\frac{9}{2}[514]\frac{11}{2}[505]$	0.084
		$4\nu\ 4\pi$		
27^-	7160	$\frac{7}{2}[514]\frac{5}{2}[512]\frac{9}{2}[624]\frac{7}{2}[633]$	$\frac{5}{2}[402]\frac{9}{2}[514]\frac{1}{2}[541]\frac{11}{2}[505]$	0.071
28^-	7465	$\frac{7}{2}[514]\frac{5}{2}[512]\frac{9}{2}[624]\frac{7}{2}[633]$	$\frac{5}{2}[402]\frac{9}{2}[514]\frac{11}{2}[505]\frac{3}{2}[532]$	0.074
28^+	7502	$\frac{7}{2}[514]\frac{5}{2}[512]\frac{9}{2}[624]\frac{7}{2}[633]$	$\frac{5}{2}[402]\frac{9}{2}[514]\frac{11}{2}[505]\frac{3}{2}[532]$	0.074
28^+	7746	$\frac{7}{2}[514]\frac{5}{2}[512]\frac{9}{2}[624]\frac{7}{2}[633]$	$\frac{5}{2}[402]\frac{9}{2}[514]\frac{11}{2}[505]\frac{3}{2}[651]$	0.088
28^-	7750	$\frac{7}{2}[514]\frac{5}{2}[512]\frac{9}{2}[624]\frac{7}{2}[633]$	$\frac{9}{2}[514]\frac{7}{2}[404]\frac{1}{2}[541]\frac{11}{2}[505]$	0.060
29^-	8055	$\frac{7}{2}[514]\frac{5}{2}[512]\frac{9}{2}[624]\frac{7}{2}[633]$	$\frac{9}{2}[514]\frac{7}{2}[404]\frac{11}{2}[505]\frac{3}{2}[532]$	0.063
29^+	8092	$\frac{7}{2}[514]\frac{5}{2}[512]\frac{9}{2}[624]\frac{7}{2}[633]$	$\frac{9}{2}[514]\frac{7}{2}[404]\frac{11}{2}[505]\frac{3}{2}[402]$	0.063

6.4 Quasiparticle configurations

The crossings in several of the prompt bands in ^{180}Os have been discussed in several studies [62, 63]. Quasiparticle configurations have also been previously assigned to several of the band-head states. However, in order to establish possible quasiparticle configurations for the newly identified Band 3 and the significantly extended bands 8a and 8b, the alignment behavior of all the bands in ^{180}Os are considered in this thesis. A summary of the crossings observed for all bands in ^{180}Os will be presented and discussed in terms of the assigned quasiparticle configurations.

6.4.1 Quasiparticle alignment

Figure 6.4 shows the plots of the aligned angular momentum, against rotational frequency for bands 1a, 1b, 2 and 3 produced in this work. Figure 6.5 shows the plots of the aligned angular momentum, against rotational frequency for bands 4, 5, 6, 7a and 7b. Figure 6.6 shows the corresponding experimental Routhians, e' for bands 1-6. A reference band with the Harris parameters $\Im_0 = 25.1\ \hbar^2$MeV and $\Im_1 = 57.3\ \hbar^4$MeV was subtracted in the alignment calculations [71].

A summary of the rotational frequency at which band crossings were observed $\hbar\omega_c$, the gain in aligned angular momentum Δi_x, measured for each crossing and the quasiparticle configurations, is given in Table 6.3. The bands are also labelled by parity and signature in the form $(\pi, \alpha)_i$, where i is a running index chosen to match those assigned in previous Refs. [63] and [62]. Crossings are seen in two distinct ranges of rotational frequency. The first set of crossings are observed in the range 0.24 MeV $\leq \hbar\omega \leq$ 0.29 MeV

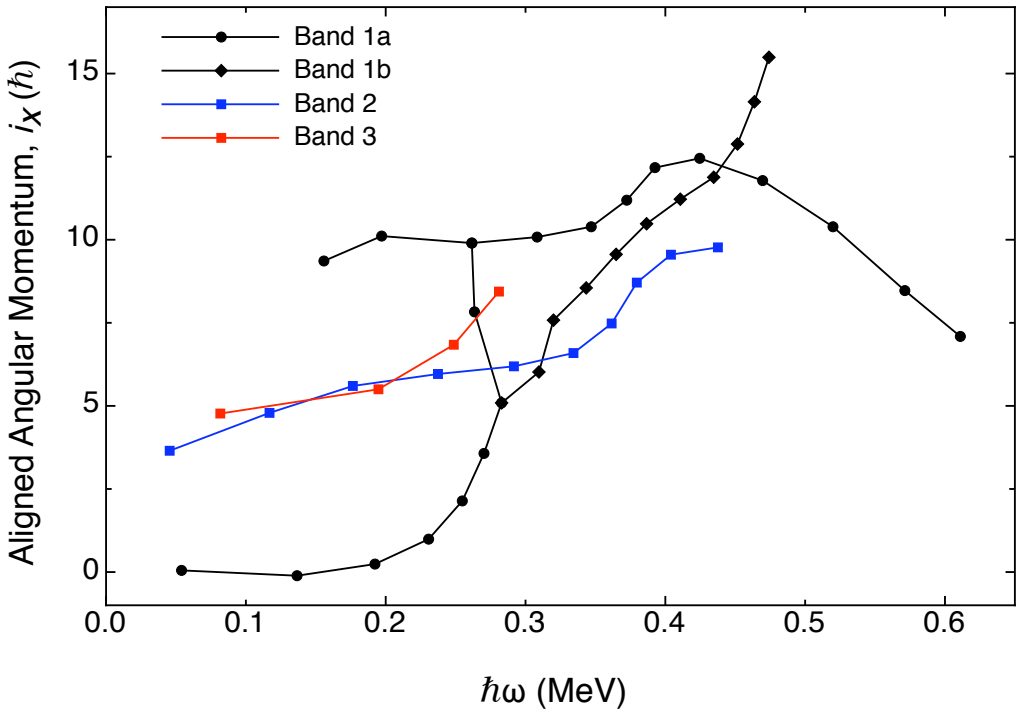

Figure 6.4: [Colour] Aligned angular momentum, i_x against rotational frequency for bands 1a, 1b, 2 and 3. Reference bands with Harris parameters $\Im_0 = 25.1\ \hbar^2$MeV and $\Im_1 = 57.3\ \hbar^4$MeV were subtracted from the data. K values equal to the band-head spins were assumed.

and are due to the neutron AB, AD and BC crossings. The νAB crossing is theoretically predicted by the CSM to occur at $\hbar\omega_c = 0.26$ MeV as shown in Fig. 6.2. This is consistent with the νAB crossings observed in the isotones ^{179}Re and and ^{181}Ir at $\hbar\omega_c = 0.26$ and 0.28 MeV, respectively [72, 73]. The ν BC and ν AD crossings were observed at $\hbar\omega = 0.29$ MeV and 0.32 MeV in ^{181}Os [74] and ^{179}Os [75], respectively.

Figures 6.4, 6.5 and 6.6 show that a second set of crossings take place in the 0.35 MeV $\leq \hbar\omega_c \leq$ 0.43 MeV rotational-frequency range. From the CSM calculations these crossings could be due to either the νCD or νEF

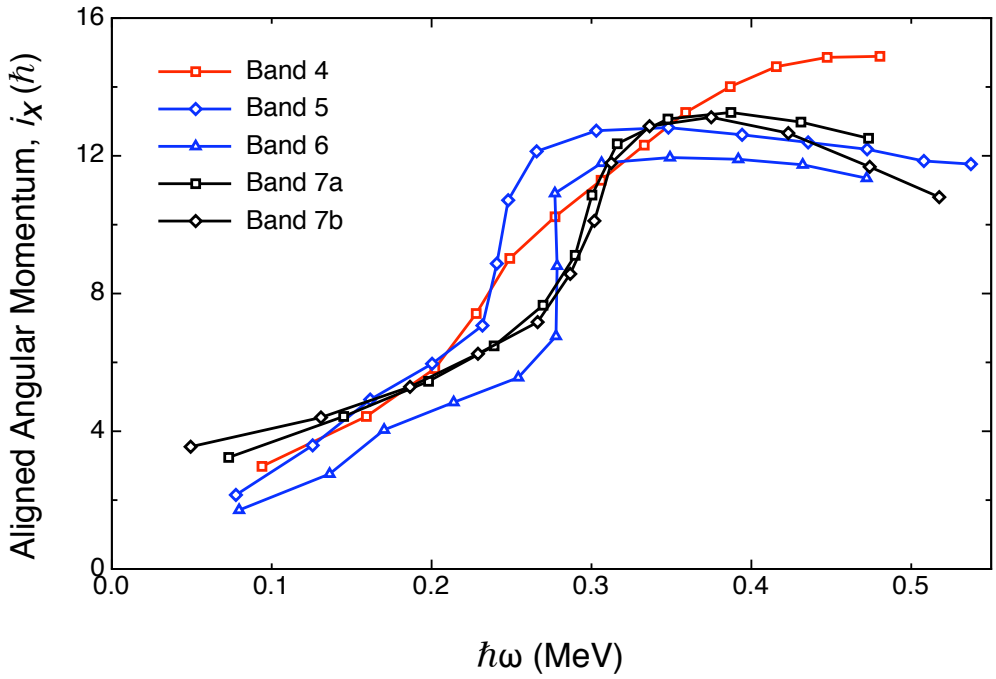

Figure 6.5: [Colour] Aligned angular momentum against rotational frequency for bands 4, 5, 6, 7a and 7b. Reference bands with Harris parameters $\Im_0 = 25.1\ \hbar^2$MeV and $\Im_1 = 57.3\ \hbar^4$MeV were subtracted from the data. K values equal to the band-head spins were assumed.

crossings, or a proton crossing. The first proton crossing is predicted by the CSM calculations to occur at a rotational frequency of $\hbar\omega_c = 0.45$ MeV, as shown in Fig. 6.3. Since some experimental deviation from the rotational frequencies of crossings predicted by the CSM occurs, proton crossings must be addressed when determining which orbitals are crossing in the 0.35 MeV $\leq \hbar\omega_c \leq$ 0.43 MeV rotational-frequency range. The proton crossing should be observed in all the bands built upon quasineutron configurations. However, the crossings in this frequency range were blocked for bands 4-8 in ^{180}Os, which are built on configurations of quasineutrons alone, suggesting that the crossings are due to the alignment of neutron orbitals. A crossing has also been observed in the $\frac{1}{2}$[541] quasiproton band of ^{181}Ir at

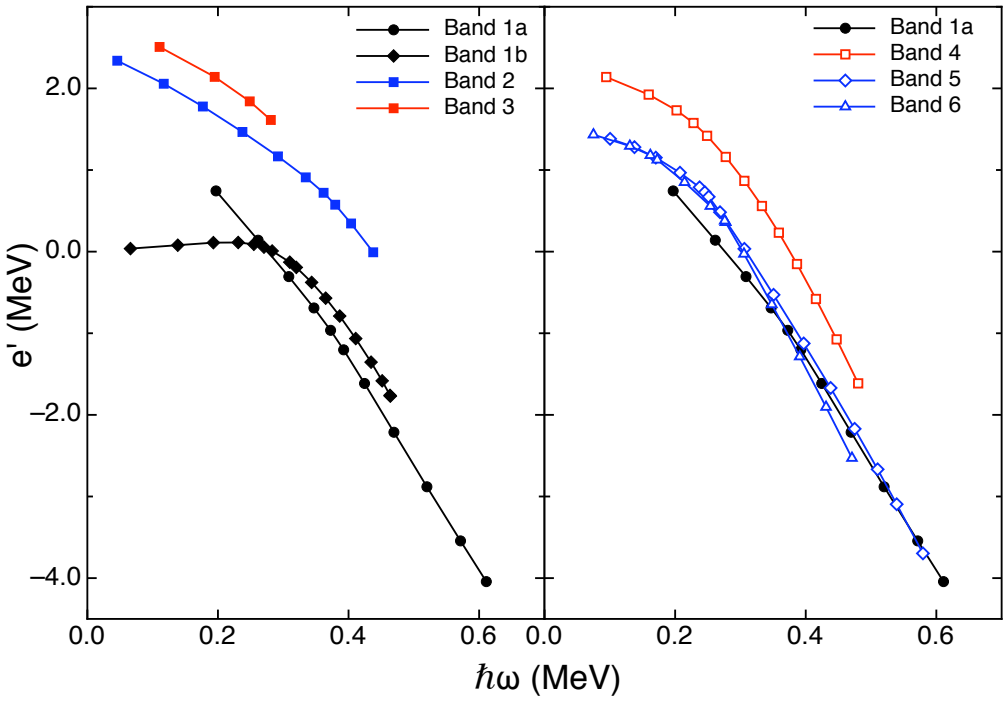

Figure 6.6: [Colour] Routhians for bands 2-6. Open symbols denote negative parity bands. Reference bands with Harris parameters $\Im_0 = 25.1\ \hbar^2$MeV and $\Im_1 = 57.3\ \hbar^4$MeV were subtracted from the data.

$\hbar\omega_c = 0.42$ MeV [72]. Since the proton crossing is blocked in this band, the observed band crossing must be due to the alignment of neutrons. The observation of this crossing supports the conclusion that the crossings observed in the 0.35 MeV $\leq \hbar\omega_c \leq$ 0.43 MeV region of ^{180}Os are due to neutrons. As such a proton crossing can be excluded from consideration in ^{180}Os for $\hbar\omega < 0.5$ MeV. Proton crossings have not been observed in this rotational-frequency range in the neighbouring nuclei including ^{181}Os [74], ^{182}Os [76], ^{181}Ir [72] and ^{179}Re [73].

It has now been established that band crossings observed in the region 0.35 MeV $\leq \hbar\omega_c \leq$ 0.43 MeV are due to the alignment of neutron orbitals.

Band	$(\pi,\alpha)_i$	$\hbar\omega_c$(MeV)	Δi_x ($\hbar$)	Configuration	Crossing
Band 1a	$(+,0)_0$	0.27	$\approx$10		AB
		0.39	$\approx$4		EF
Band 1b	$(+,0)_4$	0.31	$\approx$4		BC
		0.43	$\geq$4		EF
Band 2	$(+,1)_7$	0.36	$\approx$4	$\nu\frac{7}{2}[633]\frac{5}{2}[642]$	EF
				or $\nu\frac{7}{2}[633]\frac{9}{2}[624]$	
Band 3	$(+,1)_{new}$	0.25	$\geq$4	$\nu\frac{9}{2}[624]\frac{5}{2}[642]$	AB
Band 4	$(-,1)_5$	$\approx$0.24	$\approx$6	$\nu\frac{7}{2}[733]\frac{1}{2}[521]$	BC
		$\approx$0.35	$\approx$4		EF
Band 5	$(-,1)_3$	0.27	$\approx$9	$\nu\frac{7}{2}[514]\frac{7}{2}[633]$	BC
Band 6	$(-,0)_2$	0.29	$\approx$9	$\nu\frac{7}{2}[514]\frac{7}{2}[633]$	BC

Table 6.3: A summary of the rotational frequency of band crossings $\hbar\omega_c$, gains in alignment, Δi_x, and quasiparticle configurations for bands 1-6 from Figs 6.4, 6.5 and 6.6. The bands are also labelled by their signature and parity $(\pi,\alpha)_i$.

The CSM calculations for neutrons, shown in Fig. 6.2, predict that both νCD and νEF crossings should occur in the 0.35 MeV $\leq \hbar\omega \leq$ 0.43 MeV region. However, only one crossing is observed in the second crossing range for bands 1a and 1b, where neither crossing is blocked. Therefore, it follows that only one of these neutron crossings is being observed in the 0.35 MeV $\leq \hbar\omega_c \leq$ 0.43 MeV range. Due to the fact that the second crossing is blocked in all the negative parity bands of ^{180}Os (which would most likely contain a quasineutron in the EF orbitals), as shown in Figs. 6.5 and 6.6, it is considered that crossings in the 0.35 MeV $\leq \hbar\omega \leq$ 0.43 MeV rotational-frequency range are due to the alignment of the νEF orbitals. This conclusion is supported by the lack of crossing in this rotational-frequency range in the band based on the νEF, $\frac{7}{2}$[514] quasineutron in ^{181}Os [74].

6.4.2 Band 1a and 1b

The fully-paired ground-state band is described by signature and parity as $(+, 0)_0$. From the Routhian plots in Fig. 6.6 and alignments in Fig. 6.4, the ground-state band is observed to cross with Band 1a at $\hbar\omega_c = 0.27$ MeV. This corresponds to a gain in alignment $\Delta i_x \approx 10\ \hbar$ (Fig. 6.4) and is consistent with the νAB crossing. A second crossing is observed in Band 1a at $\hbar\omega = 0.39$ MeV and shows a gain in alignment of $\Delta i_x \approx 4\ \hbar$ (see Table 6.3), consistent with a νEF crossing, as discussed in the previous section. Figure 6.6 shows that the ground-state remains yrast until $\hbar\omega = 0.27$ MeV at which point Band 1a becomes yrast.

Band 1b can also be considered as a continuation of the ground-state band which has crossed with a $\nu(i_{13/2})^2$ configuration at $\hbar\omega = 0.31$ MeV, with a corresponding gain in alignment of $\Delta i_x \approx 4\hbar$. This is consistent with either a νBC or νAD crossing. The crossing is observed to occur at a slightly lower rotational frequency than predicted by the CSM calculations, however, it is within the range of the observed crossing frequencies in ^{181}Os (see Section 6.4.1). Band 1b was assigned to the νBC configuration in Ref. [63]. This assignment was based upon the similarities in the experimental Routhians of bands 1a and 1b, shown in Fig. 6.6, where the νBC band is predicted to closely resemble that of the νAB band. The beginning of a second crossing (EF) is observed in Band 1b at $\hbar\omega = 0.43$ MeV with an alignment gain of $\Delta i_x > 4\ \hbar$.

6.4.3 Band 2

Band 2, $(+,1)_7$ was previously presented as being based on an intrinsic state with a $\nu(i_{13/2})^2$ configuration [62, 63]. A neutron in the $\frac{7}{2}[633]$ orbital is expected to be included in the configuration since the first crossings νAB, νBC and νAD are all blocked. A backbend was observed in the 0.35 MeV $\leq \hbar\omega_c \leq$ 0.43 MeV region as seen in the alignment plot in Fig. 6.4. The crossing was measured at a rotational frequency of $\hbar\omega = 0.36$ MeV with a corresponding gain in alignment of $\Delta i_x > 4\ \hbar$. This crossing is consistent with the νEF crossing and supports the assignment of positive parity to the band since the lowest-lying negative parity orbitals, E and F, are not blocked. Two possible configurations must be considered for the band-head state of Band 2 since it is ambiguous which Nilsson orbitals are contributing to the C and D orbitals. For a band-head state based on a νAC configuration the possible Nilsson configurations are $\nu\frac{7}{2}[633]\frac{5}{2}[642]$ and $\nu\frac{7}{2}[633]\frac{9}{2}[624]$. The alignment of Band 2 at $\hbar\omega = 0$ is $i_x \approx 5\ \hbar$ and is consistent with the j and Ω values for both of these configurations.

Band 2 exhibits similar alignment properties to the (+,1) band built on the $\nu\frac{7}{2}[633]\frac{9}{2}[624]$ configuration in ^{182}Os [3, 76, 77], and as such is considered the most likely configuration for the band-head state of Band 2. The band-head state of Band 2 in ^{180}Os was assigned a spin of I^π=8^+ to reflect this comparison. The BCS calculations predict an excitation energy of $E^* =$ 1923 keV for the $K^\pi = 8^+$ coupling of this configuration. The excitation of the band-head state was measured as $E^* = 2427$ keV differing slightly from the theory.

6.4.4 Band 3

Band 3, $(+,1)_{new}$, was established in this thesis and the lowest-lying state in this band was observed at an excitation energy of $E^* = 3293$ keV and spin of $I^\pi = 15^+$. This is consistent with the energy of 4-quasiparticle states as predicted by the BCS calculations in Table 6.2. A possible configuration for this state is the 4-quasineutrons in the $\nu\frac{7}{2}[514]$ $\frac{5}{2}[512]$ $\frac{9}{2}[624]$ $\frac{5}{2}[642]$ Nilsson orbitals. The beginning of a band crossing is observed at $\hbar\omega = 0.25$ MeV with an alignment gain of $\Delta i_x > 4$ $\hbar$, see Fig 6.4. This is consistent with the νAB crossing in Band 1a (Fig. 6.4) and as such excludes the $\frac{7}{2}[633]$ orbital from the configuration. From the BCS calculations, the closest lying configuration without a $\frac{7}{2}[633]$ quasineutron was the aforementioned configuration. The $K^\pi = 13^+$ configuration was calculated as having an excitation energy of $E^* = 3664$ keV. An additional 4-quasineutron configuration ($\frac{7}{2}[514]$ $\frac{5}{2}[512]$ $\frac{1}{2}[521]$ $\frac{9}{2}[624]$) was predicted to have $K^\pi = 11^-$ at $E^* = 2866$ keV, however this was discounted since the initial alignment of the band resembles that of Band 2, suggesting the configuration contains $\nu(i_{13/2})^2$ orbitals.

6.4.5 Band 4

It has previously been established that Band 4, $(-,1)_5$ is based on νAG 2-quasiparticle configuration [62]. A possible configuration is $\nu\frac{7}{2}[733]\frac{1}{2}[521]$, and is consistent with the observed alignment features for this band. The first crossing is observed at $\hbar\omega = 0.24$ MeV with an alignment gain of $\Delta i_x \approx 6$ consistent with the νBC crossing. A second crossing is observed at $\hbar\omega = 0.35$ MeV consistent with an νEF crossing as discussed in Section 6.4.1.

As well as decaying into the ground-state band, strong transitions from

Band 4 are observed to levels with $I^\pi = 7^-$, 9^- and 11^- in Band 5, suggesting the bands may be based on a similar configuration. Bands 5 and 6 are based on the $\frac{7}{2}[514]\frac{7}{2}[633]$ 2-quasineutron configuration (discussed further in Section 6.4.6) and have the $\frac{7}{2}[633]$ quasineutron in common with Band 4 accounting for the transitions observed between the bands with equal signature.

6.4.6 Bands 5 and 6

The signature partners, bands 5, $(-,1)_3$, and 6, $(-,0)_2$, were previously identified to be based on the $\frac{7}{2}[514]$ $\frac{7}{2}[633]$ 2-quasineutron configuration [62, 63]. This is also the configuration that forms the $K^\pi = 7^-$ isomeric state and band-head state of bands 7a and 7b. In the case of bands 5 and 6, the Ω projections couple as $K = \Omega_1 - \Omega_2$. The alignments for bands 5 and 6 follow closely those for bands 7a and 7b, as shown in Fig. 6.5. In all four of these bands the νEF crossing, expected in the range 0.35 MeV $\leq \hbar\omega_c \leq$ 0.43 MeV, is blocked by the occupation of the $\frac{7}{2}[514]$ quasineutron orbital. The νAB crossing is similarly blocked by the $\frac{7}{2}[633]$ quasineutron. A crossing is observed for each band in the region expected for either the νAD or νBC crossings. The crossings observed for Bands 5 and 6 are at a slightly lower rotational frequency than those in bands 7a and 7b, as shown in Figure 6.5. This suggests it is the lower frequency νBC crossing that is observed in bands 5 and 6. It follows that bands 5 and 6 are based on the νAF and νAE configurations, respectively.

It was also presented in Refs. [62, 63] that at low spins bands 5 and 6 are based on octupole vibrations as expected for negative parity configurations including a ν $i_{13/2}$ orbital [78]. This is supported by the uneven alignment

at low spin as observed in Fig. 6.5 and the favoured depopulation of the odd signature band due to the admixture of the octopole $K^{\pi}=0^{-}$ band. This has been seen in several bands in the region, for example in the isotone ^{178}W [79] and in the isotope ^{182}Os [76].

6.4.7 Bands 7a and 7b

Figure 6.7 shows the plots of the aligned angular momentum against rotational frequency for bands 7a, 7b, 8a and 8b. Figure 6.8(a) shows the corresponding experimental Routhians, e' for these bands. A reference band with the Harris parameters $\Im_0 = 25.1\ \hbar^2$MeV and $\Im_1 = 57.3\ \hbar^4$MeV was subtracted in the calculations [71].

A summary of the rotational frequency at which crossings were observed, along with the gain in aligned angular momentum measured for each crossing, is given in Table 6.4.

Band	$(\pi,\alpha)_i$	$\hbar\omega_c$(MeV)	Δi ($\hbar$)	Configuration	Crossing
Band 7a	$(-,1)_1$	0.29	$\approx$5	$\frac{7}{2}$[514],$\frac{7}{2}$[633]	AD
Band 7b	$(-,0)_1$	0.29	$\approx$5	$\frac{7}{2}$[514],$\frac{7}{2}$[633]	AD
Band 8a	$(-,1)_9$	0.39	$\geq$2		
Band 8b	$(-,0)_9$	0.39	$\geq$3		

Table 6.4: A summary of the rotational frequency of band crossings, $\hbar\omega_c$, gains in alignment, Δi_x, and quasiparticle configurations for bands 7a, 7b, 8a and 8b from Figs 6.7 and 6.8. The bands are also labelled by their signature and parity $(\pi,\alpha)_i$.

The strongly coupled signature partners, bands 7a and 7b, are based on the isomeric state with a $\nu\frac{7}{2}[514]\frac{7}{2}[633]$ 2-quasiparticle configuration, coupled to $K^{\pi}=7^{-}$, as reported in several previous studies [62, 63]. The band-head state is the well known K isomer with a half-life of $T_{1/2} = 19.0 \pm 0.3$ ns

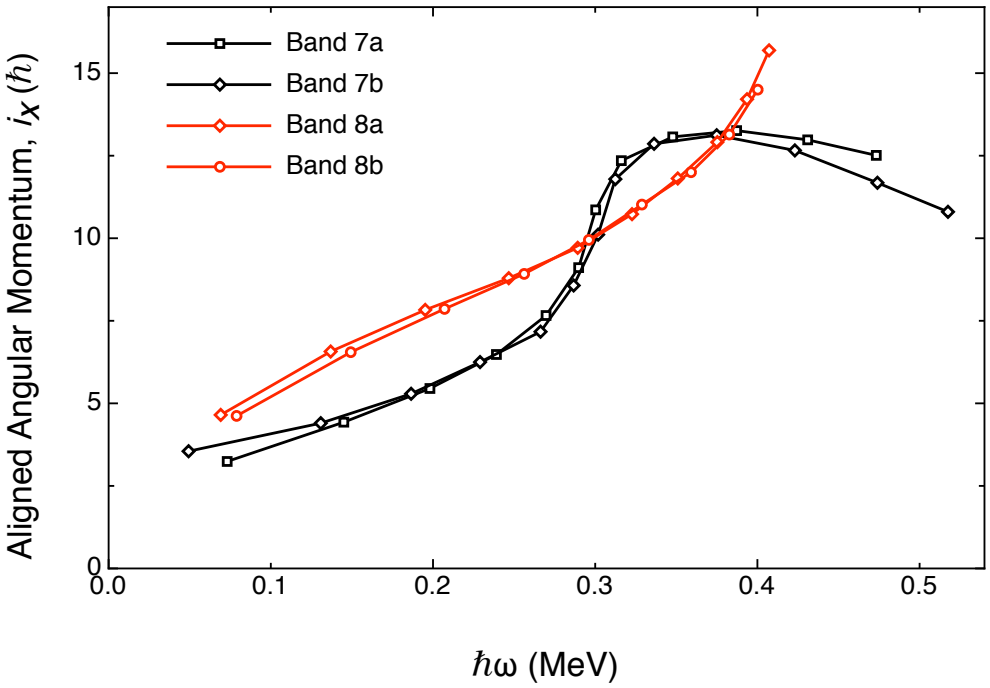

Figure 6.7: [Colour] Aligned angular momentum against rotational frequency for bands 7a, 7b, 8a and 8b. Reference bands with Harris parameters $\Im_0 = 25.1\ \hbar^2$MeV and $\Im_1 = 57.3\ \hbar^4$MeV were subtracted from the data. K values equal to the band head spins were assumed.

measured in this work. Bands 7a and 7b each undergo a band crossing at a rotational frequency of $\hbar\omega_c = 0.29$ MeV, resulting in a gain in alignment of $\Delta i_x > 4\ \hbar$. This is consistent with the νAD crossing, at a slightly higher rotational frequency than the νBC crossing observed in bands 5 and 6. Consequently, the $(-,0)_1$ band (Band 7b) is based on the νBF configuration and the $(-,1)_1$ band (Band 7a) is based on the νBE configuration. No crossing is observed in the 0.35 MeV $\leq \hbar\omega_c \leq$ 0.43 MeV region (EF) as expected for this configuration.

The BCS calculations predict an excitation energy of $E^* = 1704$ keV for the $K = 7$, $\nu\frac{7}{2}[514]\frac{7}{2}[633]$ configuration (see Table 6.2) compared to the

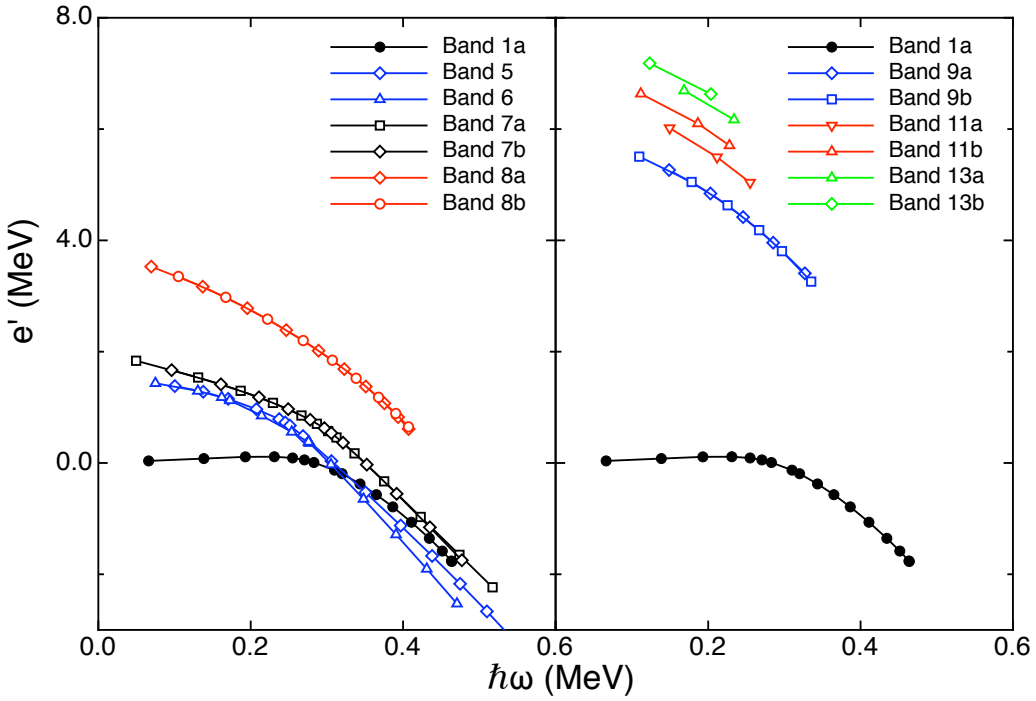

Figure 6.8: [Colour] Routhians for bands 7-13. Open symbols for negative parity bands. Reference bands with Harris parameters $\Im_0 = 25.1\ \hbar^2$MeV and $\Im_1 = 57.3\ \hbar^4$MeV were subtracted from the data.

experimentally observed excitation energy of $E^* = 1929$ keV. The theoretical $|\frac{g_k - g_R}{Q_0}|$ value for the $\nu\frac{7}{2}[514]\ \frac{7}{2}[633]$ configuration was calculated as $|\frac{g_k - g_R}{Q_0}| = 0.036$ via the method described in Section 4.4.3. The experimental $|\frac{g_k - g_R}{Q_0}|$ values were measured up to the spin $I^\pi = 16^-$ level and are shown in Fig. 6.9. The weighted average of the experimental $|\frac{g_k - g_R}{Q_0}|$ value was calculated as $|\frac{g_k - g_R}{Q_0}| = 0.015 \pm 0.001$ and is displayed as a black line in the figure. The theoretical $|\frac{g_k - g_R}{Q_0}|$ values for the $\nu\frac{7}{2}[514]\frac{7}{2}[633]$ and $\frac{5}{2}[512]\ \frac{9}{2}[624]$ configurations are also shown. All of the theoretical values lie outside of the experimental value. This may be due an overestimate of the Q_0 value used to calculate the theoretical $|\frac{g_k - g_R}{Q_0}|$ values (see Section 4.4.3). The theoretical

$|\frac{g_k - g_R}{Q_0}|$ value for the $\nu\frac{7}{2}[514]$ $\frac{7}{2}[633]$ configuration lies closest to experimental $|\frac{g_k - g_R}{Q_0}|$ value supporting the assignment.

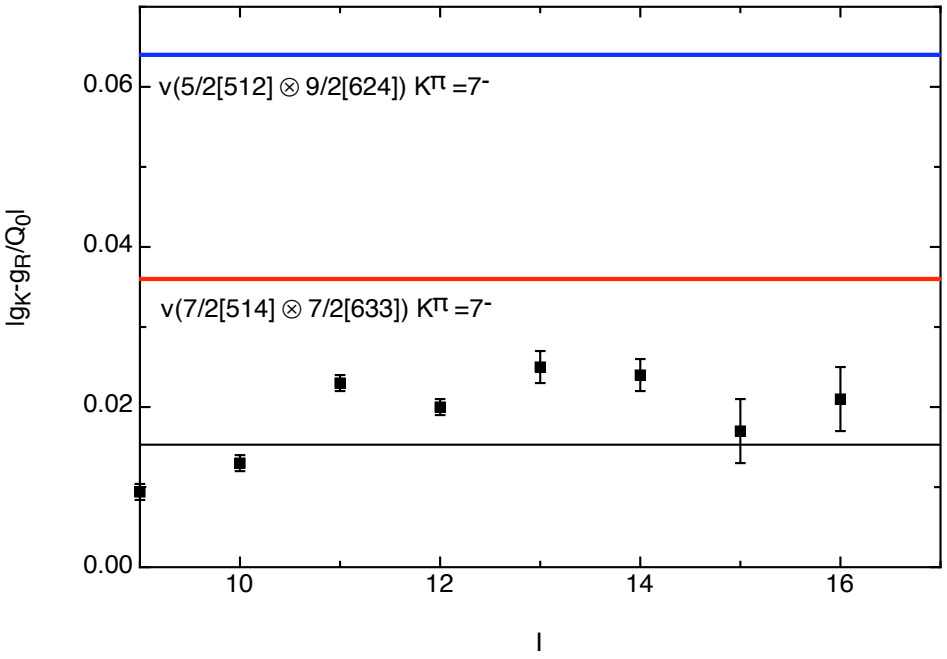

Figure 6.9: [Colour] Measured $|\frac{g_k - g_R}{Q_0}|$ values for bands 7a and 7b; the weighted mean is shown as the solid black line. The theoretically calculated $|\frac{g_k - g_R}{Q_0}|$ values are shown for the possible 2-quasiparticle configurations.

6.4.8 Decay of the 7^- isomer

The partial half-lives $T^P_{1/2}$, Weisskopf estimates, $\mathrm{T}^W_{1/2}$, and reduced hindrances, f_ν, were calculated for the transitions decaying from the K^π=7^- isomeric state and are displayed in Table 6.5. The Weisskopf estimates for the $E1$ transitions have been multiplied by a factor of 10^4 to account for their observed additional hindrance, with respect to the Weisskopf estimates [80].

The K hindrances measured in this thesis are of the same order of magnitude to those measured in Refs. [62, 64]. The small differences in the

Energy	Multipolarity	$T^W_{1/2}$ (ns)	$T^P_{1/2}$ (ns)	ν	f_ν
1134	$E1$	0.15×10^{-3}	462	6	8.23
672	$E1$	7.1×10^{-3}	213	6	5.57
549	$E1$	1.3×10^{-2}	77	6	4.25
51	$E1$	16	862	6	1.94
302	$E1$	7.9×10^{-11}	50	6	2.92
325	$E2$	2.6	236	5	2.47

Table 6.5: Hinderance factors per degree of K forbideness, f_ν, for the transitions from the 1928-keV isomer. The weisskopf estimate for $E1$ transitions have been multiplied by 10^4 [80].

hindrances arises from the new measurements of the half-life of the isomer and the intensity of the transitions. It is usual to expect a hindrance of $f_\nu \sim 100$ per degree of K forbideness in this region. The lower than expected value of f_ν in this isomer has been attributed to mixing with lower K states in the nucleus [62].

6.4.9 Bands 8a and 8b

The assignment of a quasiparticle configuration to the band-head of bands 8a and 8b is ambiguous. Several configurations must be considered as possibilities, with the supporting evidence for each being based on the excitation energy, $|\frac{g_k - g_R}{Q_0}|$ values and the aligned-angular momentum plots. A configuration of $\nu\frac{7}{2}[514]\frac{7}{2}[633]$ and $\pi\frac{9}{2}[514]\frac{1}{2}[541]$ was assigned to the band-head state in Ref. [63]. The $\pi\frac{1}{2}[541]$ orbital lies far from the Fermi surface for ^{180}Os, and as such was not considered in the BCS calculations carried out for this thesis or as part of the quasiparticle configuration for this band.

The $|\frac{g_k - g_R}{Q_0}|$ values were measured for states in both bands 8a and 8b and are plotted against the I in Fig. 6.10. The errors become substantially large

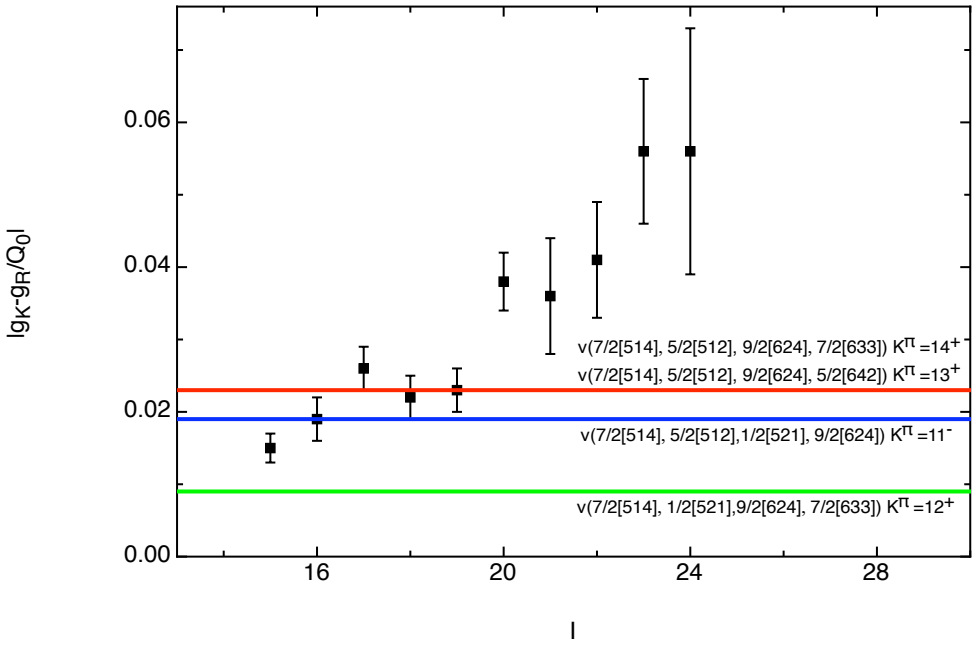

Figure 6.10: [Colour] Measured $|\frac{g_k - g_R}{Q_0}|$ values for bands 8a and 8b; the weighted mean is shown as the solid black line. The theoretically calculated $|\frac{g_k - g_R}{Q_0}|$ values are shown for the possible 4-quasiparticle configurations.

for the high spin $|\frac{g_k - g_R}{Q_0}|$ values due to the uncertainties in the intensity. The weighted average was calculated as $|\frac{g_k - g_R}{Q_0}| = 0.022 \pm 0.001$ and is comparable to the theoretical $|\frac{g_k - g_R}{Q_0}|$ values for four 4-quasineutron configurations: $\nu\ \frac{7}{2}[514]\frac{5}{2}[512]\frac{1}{2}[521]\ \frac{9}{2}[624]$, $\nu\ \frac{7}{2}[514]\ \frac{5}{2}[512]\ \frac{9}{2}[624]\ \frac{7}{2}[633]$, $\nu\ \frac{7}{2}[514]\ \frac{9}{2}[512]\frac{9}{2}[624]\ \frac{5}{2}[642]$ and $\nu\ \frac{7}{2}[514]\ \frac{1}{2}[521]\frac{9}{2}[624]\ \frac{7}{2}[633]$ with $|\frac{g_k - g_R}{Q_0}|$ values of 0.019, 0.023, 0.023, and 0.009, respectively. These values are plotted for comparison with the experimental data in Fig. 6.10. Bands 8a and 8b were determined to have negative parity based on the non isomeric lifetime for the band-head decays into Band 7a (see Section 5.2.3). The $\nu\ \frac{7}{2}[514]\frac{5}{2}[512]\frac{1}{2}[521]\ \frac{9}{2}[624]$ configuration is the only negative parity configuration that has a $|\frac{g_k - g_R}{Q_0}|$ value consistent with the experimentally determined value.

Although the $|\frac{g_k - g_R}{Q_0}|$ values suggest the 4-quasineutron state with the

configuration $\nu\ \frac{7}{2}[514]\ \frac{5}{2}[512]\frac{1}{2}[521]\ \frac{9}{2}[624]$ is the most likely configuration, a discontinuity arises with the aligned angular momentum plots. The plot of the aligned angular momentum against rotational frequency is shown in Fig. 6.7. There is no increase in the alignment in the first crossing region, suggesting that the νAB and the νCD orbitals may both be occupied. A more likely configuration in this case would be the $\nu\frac{7}{2}[514]\ \frac{9}{2}[624]\ \frac{7}{2}[633]\ \frac{5}{2}[642]$ configuration as it contains a quasineutron in both the AB and CD orbitals. The theoretical $|\frac{g_k - g_R}{Q_0}|$ value for this configuration is $|\frac{g_k - g_R}{Q_0}| = 0.004$ and is inconsistent with the experimental value, however a similar discrepancy was noticed for bands 7a and 7b, shown in Fig. 6.9. A gain in alignment is observed at a rotational frequency of $\hbar\omega_c = 0.39$ MeV, consistent with a νEF crossing, which should be blocked by the $\frac{7}{2}[633]$ neutron in this configuration. However, this band crossing is only observed at spins where states have been tentatively assigned so does not definitively rule out this configuration.

The band-head excitation energy was measured as $E^* = 3706$ keV, consistent with the value of $E^* = 3750$-keV predicted for the $\nu\frac{7}{2}[514]\ \frac{9}{2}[624]\ \frac{7}{2}[633]\ \frac{5}{2}[642]$ configuration. This configuration contains the quasineutrons on which bands 7a and 7b are based and would explain the decay into these bands. $K \leq 9$ was assigned to the band-head of bands 8a and 8b; a higher assignment of K for this band would result in a degree of K forbideness and an isomeric state which was not observed.

6.5 5848-keV isomer

6.5.1 Decay of the 5848-keV isomer

The spin of the 5848-keV isomer was tentatively assigned as $I^{\pi} = 22^{+}$ based on the internal conversion of the 287-keV transition. This transition was found to be a $\Delta I = 2$ multipolarity, although a $\Delta I = 1$ multipolarity was not entirely ruled out (see Section 5.3.1). The value of K for the 5848-keV isomer has been assigned as equal to the band-head spin to give $K^{\pi}= 22^{+}$ for the isomer. Only one $K^{\pi}= 22^{+}$ level was predicted by the BCS calculations. The 6-quasiparticle configuration, $\nu\frac{7}{2}[514]$ $\frac{1}{2}[521]\frac{9}{2}[624]$ $\frac{7}{2}[633]$ and $\pi\frac{9}{2}[514]$ $\frac{11}{2}[505]$, was predicted to have a excitation energy of $E^{*} = 5508$ keV and is in relatively good agreement with the experimental excitation energy of 5848 keV.

The K value of the band fed by the decay of the 5848-keV isomer (see Fig 5.13) was estimated to have $K \leq$ 18 and a possible $\nu\frac{9}{2}[624]$ $\frac{7}{2}[633]$ $\pi\frac{9}{2}[514]$ $\frac{11}{2}[505]$ configuration. The two states observed in this band decay into Band 1b above the νBC band crossing, consisting of a neutron in the $\frac{7}{2}[633]$ orbital and another neutron, possibly in the $\frac{9}{2}[624]$ orbital. Having these orbitals in common may explain the decay solely to this band.

The Weisskopf estimate, $T^{W}_{1/2}$, and the reduced K-hindrance, f_{ν}, have been calculated for a 287-keV transition with $E1$, $M1$, $E2$ and $M2$ multipolarities. The results are displayed in Table 6.6. The Weisskopf estimates for the $E1$ transitions have been multiplied by a factor of 10^{4} to account for their observed additional hindrance, with respect to the Weisskopf estimates [80]. The K hindrance for the $E2$ transition was calculated as $f_{\nu} = 12.9$, and is of the same order expected for the ^{180}Os isotopes [64]. This supports the

assignment of an $E2$ multipolarity for the 287-keV isomer, and the assigned configuration of the band.

Multipolarity	estimate of half-life (s)	ν	f_ν
$E1^*$	9.2×10^{-11}	3	20.5
$M1$	5.24×10^{-13}	3	115.2
$E2$	4.80×10^{-9}	2	12.9
$M2$	3.19×10^{-7}	2	1.6

Table 6.6: Hinderance factors per degree of K forbideness, f_ν, for the 287-keV transition from the 5848-keV isomer. The weisskopf estimate for the $E1$ transition has been multiplied by 10^4 [80].

6.5.2 Bands 9a and 9b

The band-head state of bands 9a and 9b is the isomeric state at 5848-keV. The experimental $|\frac{g_K - g_R}{Q_0}|$ values were measured for states up to spins of $I^\pi = 27^+$ and 28^+ for bands 9a and 9b, respectively. The weighted average was calculated as $|\frac{g_K - g_R}{Q_0}| = 0.012 \pm 0.001$. The theoretical $|\frac{g_K - g_R}{Q_0}|$ value for the configuration assigned to the isomer was calculated as $|\frac{g_K - g_R}{Q_0}| = 0.088$ and is not consistent with the experimental measurement, however there is no other quasiparticle configuration that agrees with the experimental value. This may be due to the fact that $|\frac{g_K - g_R}{Q_0}|$ values assume a purely rotational model which may not hold true for these bands. Additionally, the theoretical $|\frac{g_K - g_R}{Q_0}|$ values were calculated using a value of Q_0 which may not be accurate for a multi-quasiparticle where the deformation parameters may have changed.

Figure 6.11 shows the aligned angular momentum against rotational frequency for bands 9a and 9b. No backbends are observed in these bands for

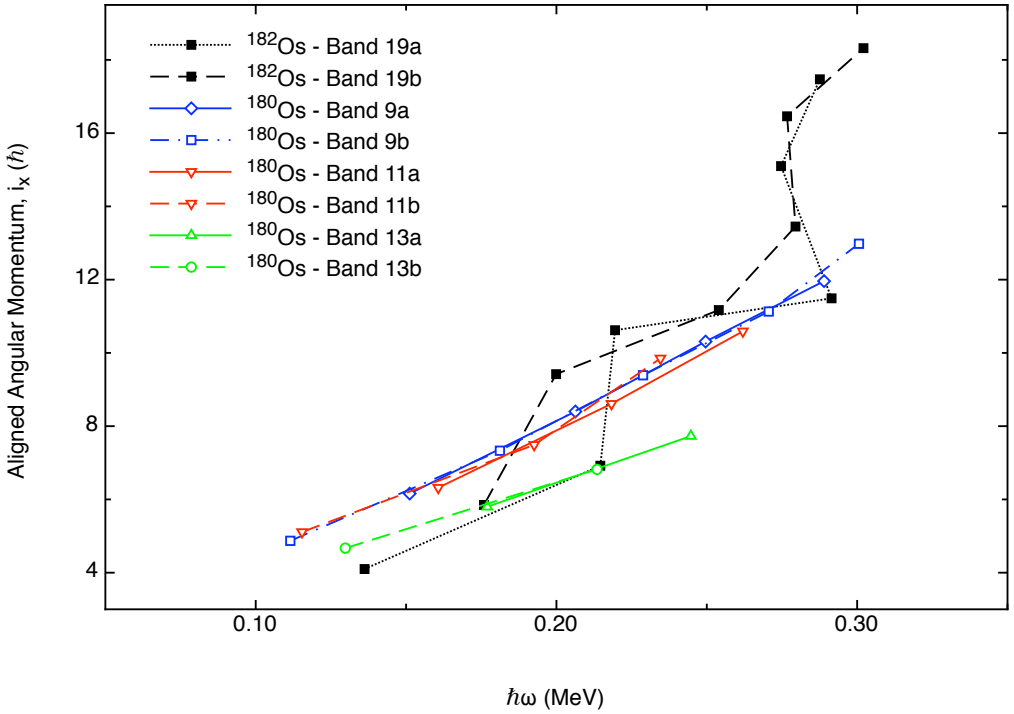

Figure 6.11: [Colour] Aligned angular momentum against rotational frequency for bands 9a, 9b, 11a, 11b, 13a and 13b. Reference bands with Harris parameters $\Im_0 = 25.1\ \hbar^2$MeV and $\Im_1 = 57.3\ \hbar^4$MeV were subtracted from the data. K values equal to the band head spins were assumed. The Band based on the K^π=25^+ in ^{182}Os is also shown.

$\hbar\omega < 0.3$ MeV as all the possible neutron crossings are blocked. The alignment appears to increase more rapidly with rotational frequency than for the lower K bands. This may be due to mixing vibrational states, similar to the bands observed above the $K^\pi = 25^+$ 130 ns isomer in ^{182}Os [2]. This will be discussed in more detail in Section 6.7.

6.5.3 Band 10

Band 10 is based on an intrinsic state with $I = 23$, discussed in Section 5.3.2 Due to the unhindered decay from this state into the $K^\pi = 22^+$ isomeric state it is assumed that the state has a K equal to that of the band-head spin, $K = 23$. Only one quasiparticle configuration was predicted by the BCS calculations to have the correct energy and K for Band 10. The $\nu\frac{7}{2}[514]$ $\frac{5}{2}[512]\frac{9}{2}[624]$ $\frac{7}{2}[633]$, $\pi\frac{7}{2}[404]$ $\frac{11}{2}[505]$ 6-quasiparticle configuration was calculated to have an excitation energy of $E^* = 5829$ keV in the $K^\pi = 23^-$ coupled state. This is comparable to the experimentally measured excitation energy for the state of $E^* = 6256$ keV. This configuration only differs by one proton to the configuration assigned to the isomeric state which may explain the strong feeding. The difference in K between this band and the isomer is $\Delta K = 1$ and as such transitions are not hindered. The mode of excitation for this band is ambiguous due to the lack of information on the multipolarity of the in-band transitions.

6.5.4 Bands 11a and 11b

Bands 11a and 11b are based on an intrinsic state at 7016-keV with an estimated spin and parity of $I^\pi = 24^+$. $K = 24$ is assigned to this state based on the unhindered $\Delta I = 1$ and $\Delta I = 2$ decays into bands 9a, 9b and 10. Since no isomeric lifetime is observed for the band-head state, ΔK must be small. A configuration of 6-quasiparticles is assumed for the band-head state since it is at an excitation energy only 1168-keV above the 6-quasiparticle isomer. From the BCS calculations it can be estimated that breaking another quasiparticle pair would require more energy. Two configurations with $K = 24$

were predicted by the BCS calculations, one with positive parity and one with negative parity: $\nu\frac{7}{2}[514]\ \frac{5}{2}[512]\frac{9}{2}[624]\ \frac{7}{2}[633]\ \pi\frac{9}{2}[514]\ \frac{11}{2}[505]$ and $\nu\frac{7}{2}[514]\ \frac{9}{2}[624]\ \frac{7}{2}[633]\ \frac{5}{2}[642]\ \pi\frac{9}{2}[514]\ \frac{11}{2}[505]$, respectively. The band was tentatively assigned to have positive parity based on the 1168-keV transition being assigned to have a multipolarity, $E2$, making the positive parity configuration the most probable for this intrinsic state.

This intrinsic state was also found to decay into the high-spin states of bands 1a, 1b and 2. A large K-forbideness would be expected for these decays, however, no hindrance was observed. A similar effect has been observed in the decay of a $K = 25$ isomer in ^{182}Os [81], where transitions to the *yrast* band have a hindrance factor per degree of K forbiddeness of only 2.2. This violation of the K-selection rule was explained by a level of γ softness allowing γ-deformation tunneling of the K barrier.

The minimum in the Potential Energy Surfaces for the isomer in ^{182}Os were calculated as $\beta_2 = 0.192$, $|\gamma| = 10$ and $\beta_4 = -0.019$ in Ref. [82]. A substantial degree of γ softness was also predicted. The $K = 25$ isomer in ^{182}Os is based on a 6-quasiparticle configuration ($\nu\frac{7}{2}[514]\ \frac{7}{2}[503]\frac{9}{2}[624]\ \frac{7}{2}[633]\ \pi\frac{9}{2}[514]\ \frac{11}{2}[505]$) differing by only one neutron to the positive parity configuration for this intrinsic state in ^{180}Os. As such it is reasonable to assume a similar degree of γ softness is present, allowing the transitions from this state to bands 1a, 1b and 3.

The alignments for bands 11a and 11b are shown in Fig. 6.11. As seen with bands 9a and 9b there is a significant increase in the aligned angular momentum with rotational frequency compared to that expected for a purely rotational band. The Routhians for the bands are shown in Fig. 6.8 and show significant signature splitting with the even signature partner reduced

in energy. This could be due to the mixing of states with an even signature band. A similar effect was observed in the bands built above the K^{π}=25^{+} 130 ns isomer in ^{182}Os [3] and may also signify a degree of triaxiality and γ softness. This will be discussed further in Section 6.7

6.6 7592-keV isomer

6.6.1 Decay of the 7592-keV isomer

The quasiparticle configuration for the 7592-keV isomer is ambiguous. The experimental $|\frac{g_k - g_R}{Q_0}|$ values were measured for the first levels of bands 13a and 13b with a weighted average of $|\frac{g_k - g_R}{Q_0}| = 0.013 \pm 0.002$. This value was not reproduced by any of the theoretical values for the quasiparticle configurations predicted by the BCS calculations. This may be explained by a variation in the value of Q_0 for multi-quasiparticle configurations. The theoretical $|\frac{g_k - g_R}{Q_0}|$ values were also found to vary from the experimental $|\frac{g_k - g_R}{Q_0}|$ values for bands 7a, 7b, 9a and 9b (see Sections 6.4.7 and 6.5.2, respectively).

The BCS calculations show several configurations where the excitation energies are close to that of the isomer. These configurations are all based on 4-neutrons and 4-protons. These configurations all include quasiparticles in the ν $\frac{7}{2}[514]\frac{5}{2}[512]\frac{9}{2}[624]\frac{7}{2}[633]$ and π $\frac{9}{2}[514]\frac{11}{2}[505]$ orbitals. This is the configuration of the intrinsic state at 7016-keV with $K^{\pi} = 24^{+}$ to which the isomer decays. The remaining protons lie in two of the following orbitals: $\frac{7}{2}[404]$, $\frac{3}{2}[532]$ $\frac{1}{2}[541]$ or$\frac{3}{2}[402]$ $\frac{3}{2}[651]$. The possible K^{π} values for the configurations are $K^{\pi} = 27^{-}$, 28^{+}, 28^{-}, 29^{+} and 29^{-}. However, this would require that the 577-keV transition to the $K = 24$ state at 7016 keV has a multipolarity $L > 3$. The Weisskopf estimates for the 577-keV transitions are listed

in Table 6.7. Multipolarities of $L > 3$ are predicted to have half-lives several orders of magnitude longer than the measured half-life of $T_{1/2} = 72 \pm 6$-ns. The K of the isomer can therefore be limited to $24 < K < 27$. The BCS calculations did not predict any states in this range.

Multipolarity	Weisskopf estimate (s)
$E1$	1.13×10^{-15}
$M1$	6.44×10^{-14}
$E2$	1.46×10^{-10}
$M2$	9.71×10^{-9}
$E3$	2.96×10^{-5}
$M3$	2.00×10^{-3}
$E4$	8.61
$M4$	6.70×10^{2}

Table 6.7: Weisskopf estimates for a 577-keV transition.

The half-life measured for the 7592-keV isomer, $T_{1/2} = 72 \pm 6$ ns, is relatively short compared to that of the 5848-keV isomer. $\Delta K = L$ for the decay of the isomer into the 7016-keV $K^{\pi} = 24^{+}$ state, therefore no K hinderance is predicted. Also, there is only one neutron difference between the initial and final quasiparticle configurations, therefore little shape or seniority isomerism is expected.

6.6.2 Bands 13a and 13b

The alignments for bands 13a and 13b are shown in Fig. 6.11 and show a similar trend to that observed for bands 9a, 9b, 11a and 11b. The Routhians for the bands are shown in Fig. 6.8 and show a substantial degree of signature splitting suggesting that there is a degree of mixing between the states. This could also be indicative of a γ-soft configuration of the nucleus as will be

discussed further in Section 6.7.

6.6.3 Level 12

The level observed at an excitation energy of $E^* = 9254$ keV decays into bands 13a and 13b at levels $\Delta I = 3$ and $\Delta I = 2$ above the isomeric state at 7592 keV. The significant gain in energy predicts that an additional pair of quasiparticles may be broken to produce Level 12 compared to the configuration of the 7592-keV isomer. This would result in a 10-quasiparticle configuration. The excitations energies predicted by the BCS calculations for 8-quasiparticle states are $E^* < 8100$ keV (see Table 6.2), supporting the conclusion that another pair of quasiparticles may be broken for the $E^* = 9254$ keV level. The decay of level 12 into bands 13a and 13b suggests that the 8-quasiparticles likely to be involved in the configuration of the 7592-keV isomer are also in the configuration for this level, since there is no additional lifetime or hinderance.

6.7 Mode of excitation above high-K isomers

The mode of excitation above the ($K^\pi = 22^+$) and $K > 24$ isomers, in bands 9, 11 and 13, cannot be adequately described by a rotational model alone. The alignments for the bands above these isomeric states are shown in Fig. 6.11 and display a large continual increase in alignment with rotational frequency. A similar trend was observed above the $K^\pi = 25^+$ isomer in ^{182}Os where multiphonon vibrations were determined to be driving the nuclear structure with some mixing of rotational states [2]. The alignments for the band above the $K^\pi = 25^+$ isomer are plotted alongside those of bands 9, 11

and 13 in Fig. 6.11. The large continual increase in alignment with rotational frequency above the isomers in ^{180}Os closely resembles that observed in the multiphonon band of ^{182}Os, suggesting a similar mode of excitation may be responsible.

To date, SCTAC calculations have been somewhat successful in predicting the multiphonon vibrations in ^{182}Os as well as the similar structures in ^{181}Os and ^{183}Os [83]. A significant increase in the γ-deformation parameter was predicted by the SCTAC calculations thoughout the bands and was interpreted as the addition of γ phonons. The resulting linear increase in excitation energy with spin was reproduced by the experimental data in each case. SCTAC calculations have also successfully reproduced the octupole vibrations observed in the actinides [84].

SCTAC calculations were carried out for theoretical bands in ^{180}Os with K^{π}=17^{-} and 21^{-} and are shown in Fig. 6.12. Although the K^{π} values used in these calculations do not entirely match those found in this work for the 5848-keV and 7592-keV isomers (as they were performed prior to this work), they do demonstrate the properties expected for a multiphonon-vibrational band and provide a useful comparison for the bands established in this work. In Fig. 6.12 the excitation energies of the levels in band 9, 11 and 13 are plotted against the spin of the level minus the K value for the band, $I - K$. The SCTAC calculations predict a linear increase in the excitation energy with $I - K$, consistent with the addition of vibrational phonons, as given by Eqn. 2.13. For a rotational band a quadratic increase in the excitation energy with $I - K$ is expected, as given by Eqn. 2.7. Although the experimental data for bands 9 and 11 increase slightly more rapidly than the SCTAC calculations predict, they do follow a linear increase in excitation energy

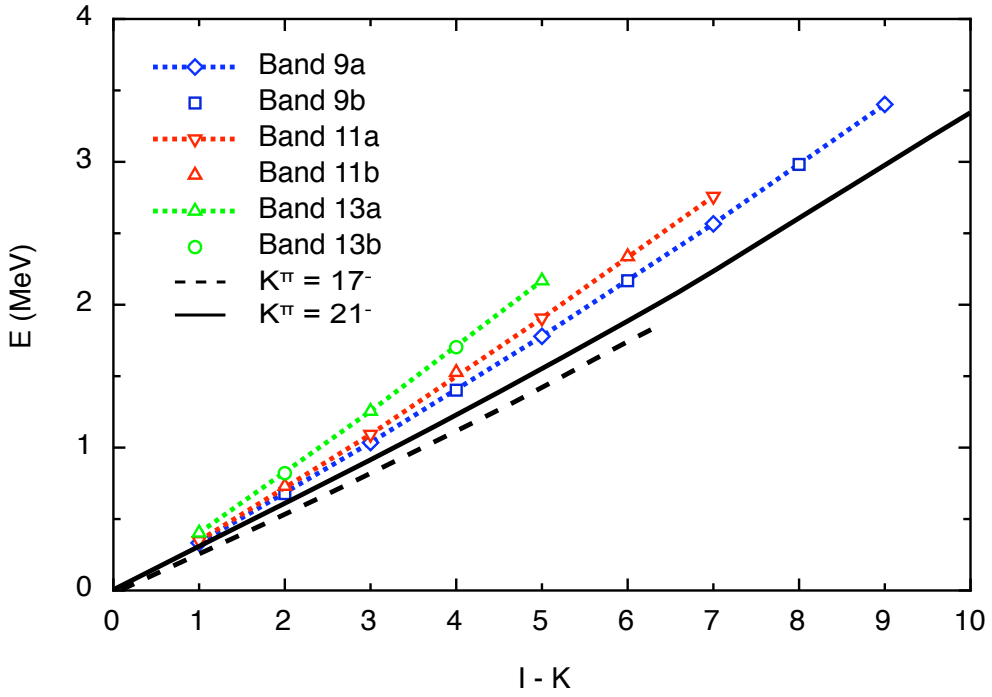

Figure 6.12: [Colour] SCTAC calculations for K^{π}= 17^{-} and 21^{-} bands in ^{180}Os. The experimental excitation energy minus the band-head energy is given against the spin of the state, I, for bands 9, 11 and 13.

with $I-K$, suggesting multiphonon vibrations are involved in the excitation of these bands. However, the excitation energy of levels in bands 13a and 13b seems to increase more significantly with $I-K$ suggesting a larger degree of rotation in the mode excitation of these bands.

Although comparison to the SCTAC calculations and the alignment of the multiphonon-vibrational band in ^{182}Os suggests that the levels bands 9, 11 and 13 may be due to multiphonon vibrations, rotational excitation can not be entirely ruled out for these bands. The strong $M1$ transitions, particularly in bands 11a and 11b, suggest rotational excitations are involved in the structure. For prolate nuclei the angular momentum vector for γ vibrations lies along the symmetry axis hindering $M1$ transitions, for which the

magnetic moment vector lies along the same axis. The observation of strong $M1$ transitions in the bands point to a mixing of rotational and vibrational excitations in the bands.

Bands 9, 11 and 13 show stronger rotational characteristics than were observed in the band above the $K^{\pi} = 25^{+}$ isomer in ^{182}Os. For example, a small but regular increase in γ-ray energy up the bands was observed in bands 9, 11 and 13 of ^{180}Os (see Fig 5.14) compared to a more irregular sequence of γ-ray energies in ^{182}Os (see Fig. 1.1). This may be explained by a strong mixing with high-spin rotational states in ^{180}Os. The large degree of signature splitting between bands 11a and 11b and between bands 13a and 13b suggests a degree of mixing is occurring for these bands and may account for the deviation from the SCTAC solutions and the observation of $M1$ transitions.

Signature splitting is also a characteristic of γ-soft nuclei. A degree of triaxiality and γ softness was used to explain the decay of the intrinsic state which is the band-head state for bands 11a and 11b in Section 6.5.4. In part, it is this γ softness that allows multiphonons to compete with rotation above high-K isomers in the osmium nuclei. The excitation energy of the γ band in ^{180}Os (see Section 5.1.8) is lower than the equivalent band in ^{182}Os [3]. As such, a larger susceptibility to γ vibrations is expected for ^{180}Os, which was not reproduced experimentally. However, the newly established bands in ^{180}Os and the $K^{\pi} = 25^{+}$ band in ^{182}Os are based on multi-quasiparticle configurations which may not follow the same trend. Future theoretical Potential Energy Surface calculations for the newly established high K states in ^{180}Os are needed to determine the degree of γ softness in the respective configurations.

Chapter 7

Summary and conclusions

The spectroscopic study of ^{180}Os described in this thesis has yielded several significant results. From prompt-coincidence analysis of both the thick- and thin-target data, several of the previously known prompt bands were extended to higher spin and a new prompt band was also established. However, it was the prompt-delayed coincidence analysis of the thick-target data that produced the most noteworthy results. The level scheme associated with the extensively studied $K^{\pi} = 7^{-}$ isomer was extended and the half-life was measured with a significantly reduced error. The placement of an isomer at 5848 keV was confirmed and an extensive prompt level scheme was established. An isomeric state was also identified in this work at 7592 keV and the corresponding prompt level scheme was deduced. The half-life of the isomers were measured from the time difference between the prompt and delayed γ rays.

Multi-quasiparticle configurations have been assigned to several of the prompt bands of ^{180}Os. Plots of the aligned angular momenta were interpreted in terms of the band crossings predicted by the CSM calculations. The

observation and blocking of band crossings at different rotational frequencies provided the basis for the assignment of configurations to each band. The excitation energy of the band-head states were also compared to those predicted by blocked BCS calculations for the corresponding configurations.

The half-life of the $K^{\pi} = 7^{-}$ isomeric state at 1929 keV was measured as $T_{1/2} = 19.0 \pm 0.3$ ns. The hinderance per degree of K forbideness was measured for the γ rays decaying from this isomer and were found to be in the range $1 < f_v < 9$, in agreement with those measured in previous studies and for similar mass Os isotopes. This value is lower than the value of f_v predicted for K isomers, and may be due to the mixing of the isomer with lower K states. The prompt level-scheme for the $K^{\pi} = 7^{-}$ isomer was extended, in particular, the signature partner bands 8a and 8b. The $|\frac{g_k - g_R}{Q_0}|$ values proved unreliable in the determination of the multi-quasiparticle configurations in this work and a 4-quasiparticle configuration was tentatively assigned to bands 8a and 8b, based on the interpretation of the aligned angular momentum plots. A possible cause of the inaccuracies in the $|\frac{g_k - g_R}{Q_0}|$ values was determined to be the estimate of the Q_0 value.

An isomeric state at 5848 keV was confirmed in this work and the corresponding decay sequence was extended. A value of $K^{\pi} = 22^{+}$ was tentatively assigned to the isomer and a possible 6-quasiparticle configuration was identified. An extensive prompt level scheme was established above this isomer via prompt-delayed coincidence analysis. Two signature partner bands were identified to be based directly on the 5848-keV isomer and a further two signature partner bands were identified above an intrinsic state with $K = 24$ at 7016 keV. An additional isomeric state was established at 7592 keV and was found to decay into the prompt structure above the 5848 keV isomer.

Although the spin and parity of the 7592-keV isomer could not be measured directly a limit of $24 < K < 27$ was assigned and possible 8-quasiparticle configurations were considered. Two signature partner bands were established above the isomeric state from prompt-delayed coincidence analysis.

The half-lives of the 5848-keV and 7592-keV isomeric states were measured as $T_{1/2} = 0.8 \pm 0.3$ μs and $T_{1/2} = 72 \pm 6$ ns, respectively. The hindrance per degree of K forbideness for the 5848-keV isomer was calculated as $f_v = 12.9$. Perhaps more significantly, the intrinsic state with $K = 24$ at 7016 keV was found to decay unhindered into low K bands, due to the tunneling of the K barrier due to a degree of γ softness.

TRS calculations predicted the deformation parameters of the fully paired state of ^{180}Os at $\hbar\omega = 0$ as $\beta_2 = 0.222$, $\gamma = 0.2$ and $\beta_4 = -0.028$. The calculations at higher rotational frequencies show a significant shallowness in the γ deformation parameter indicating a degree of γ softness in the nucleus. This γ softness proved a crucial factor in the interpretation of the mode of excitation for the newly established prompt structures above the 5848-keV and 7592-keV isomers. A rotational model alone can not describe the mode of excitation for the prompt bands and it was concluded that multiphonon vibrations were playing a part in the mode of excitation. A degree of γ softness in these configurations may result in nucleus more susceptible to γ vibrations allowing them to compete with rotation. The aligned angular momentum plots and comparison with the SCTAC calculations showed multiphonon vibrational traits, however, rotational excitation was determined to be a large contributing factor.

The larger rotational contribution observed in the bands above the high-K isomers in ^{180}Os compared to that observed above the $K^\pi = 25^+$ isomer

in ^{182}Os suggests that the multi-quasiparticle state of the $K^{\pi} = 25^{+}$ isomer in ^{182}Os exhibits a larger degree of γ softness. From the excitation energy of the γ bands it was predicted that the ^{180}Os would be more susceptible to γ vibrations. However, this was not reproduced experimentally and points to a change in the γ softness of the nucleus depending on the multi-quasiparticle configuration. Potential Energy Surface calculations could be used to further investigate the deformation and γ softness of the isomeric configurations. These calculations could be also be applied to the isomeric states in the $A \approx 180$ region of the nuclear chart to yield possible candidates for multiphonon vibrations.

The results of this thesis, focussing on the newly established isomers and their corresponding prompt structure are to be submitted for publication.

REFERENCES

[1] A. Bohr and B. R. Mottelson, *Nuclear Structure* (World Scientific, New York, 1999), Vol. 2: Nuclear Deformations.

[2] L. K. Pattison *et al.*, Physical Review Letters **91**, (2003).

[3] L. K. Pattison, PhD Thesis, (2006).

[4] D. M. Cullen *et al.*, Nuclear Physics A **728**, 287 (2003).

[5] R. Glover, MSc Thesis, 2004.

[6] J. Rainwater, Physical Review **79**, (1950).

[7] A. N. Deaken, PhD Thesis, 2006.

[8] S. M. Harris, Physical Review **138**, (1965).

[9] V. M. Strutinsky, Nuclear Physics A **95**, 420 (1967).

[10] W. Nazarewicz, R. Wyss, and A. Johnson, Nuclear Physics A **503**, 285 (1989).

[11] R. Bengtsson and S. Frauendorf, Nuclear Physics A **314**, 27 (1979).

[12] R. Bengtsson and S. Frauendorf, Nuclear Physics A **327**, 139 (1979).

[13] S. Frauendorf, Nuclear Physics A **557**, 259 (1993).

[14] S. Frauendorf, Nuclear Physics A **677**, 115 (2000).

[15] J. Bardeen, L. N. Cooper, and J. R. Schrieffer, Phys. Rev. **108**, 1175 (1957).

[16] A. Bohr, B. R. Mottelson, and D. Pines, Phys. Rev. **110**, 936 (1958).

[17] V. G. Soloviev, Soviet Physics-Doklady **5**, (1961).

[18] K. Jain *et al.*, Nuclear Physics A **591**, 61 (1995).

[19] C. J. Gallagher and S. A. Moszkowski, Physical Review **111**, (1958).

[20] J. M. Blatt and V. F. Weisskopf, *Theoretical Nuclear Physics* (Wiley and Sons, New York, 1952).

[21] P. Walker and G. Dracoulis, Nature **399**, 35 (1999).

[22] K. E. G. Lobner, Physics Letters B **26**, 369 (1968).

[23] R. Bass, Nuclear Physics A **231**, 45 (1974).

[24] J. M. Blatt and V. F. Weisskopf, *Theoretical Nuclear Physics* (Dover, ADDRESS, 1991).

[25] J. R. Beene, "EvapOR" computer code The Oak Ridge Analysis package (Oak Ridge National Laboratory, Tennesse, 1999), private communcation.

[26] L. M. Bollinger *et al.*, Nuclear Instruments and Methods in Physics Research Section A: Accelerators, Spectrometers, Detectors and Associated Equipment **328**, 221 (1993).

[27] P. K. den Hartog *et al.*, Nuclear Instruments and Methods in Physics Research Section A: Accelerators, Spectrometers, Detectors and Associated Equipment **287**, 235 (1990).

[28] K. R. Chapman, IEEE Transactions on Nuclear Science **NS 23**, 1109 (1976).

[29] E. Minehara *et al.*, Review of Scientific Instruments **57**, 742 (1986).

[30] R. Middleton, IEEE Transactions on Nuclear Science **NS 23**, 1098 (1976).

[31] P. J. Billquist and J. L. Yntema, Nuclear Instruments and Methods **178**, 9 (1980).

[32] J. L. Yntema, P. K. Den Hartog, W. Henning, and W. Kutschera, Nuclear Instruments and Methods **184**, 233 (1981).

[33] L. M. Bollinger, IEEE Transactions on Nuclear Science **NS-30**, 2065 (1983).

[34] K. W. Shepard, IEEE Transactions on Nuclear Science **NS-26**, 3659 (1979).

[35] P. J. Twin, Nuclear Physics A **557**, 3 (1993).

[36] P. J. Nolan, Endeavour **15**, 22 (1991).

[37] C. W. Beausang and J. Simpson, Journal of Physics G: Nuclear and Particle Physics **22**, 527 (1996).

[38] P. J. Nolan, F. A. Beck, and D. B. Fossan, Annual Review of Nuclear and Particle Science **44**, 561 (1994).

[39] A. M. Baxter *et al.*, Nuclear Instruments and Methods in Physics Research Section A: Accelerators, Spectrometers, Detectors and Associated Equipment **317**, 101 (1992).

[40] G. F. Knoll, *Radiation Detection and Measurement*, 3rd ed. (Wiley and Sons, New York, 1999).

[41] I.-Y. Lee, Nuclear Physics A **520**, c641 (1990).

[42] in *Overview of Detector and Signal Processing Signal*, edited by P. A. Moonier (IEEE, 345 E 47th st, New York, NY 10017, ADDRESS, 1995), No. 0-7803-3181-8.

[43] R. Firestone, *Table of Isotopes*, 8th ed. (John Wiley and Sons Inc., ADDRESS, 1999).

[44] D. M. Cullen, 'EFFIT', private communcation.

[45] W. T. Milner, "UPAK" The Oak Ridge Data Analysis Package, private communcation.

[46] D. C. Radford, Nuclear Instruments and Methods in Physics Research A **361**, 297 (1995).

[47] D. C. Radford, Nuclear Instruments and Methods in Physics Research A **361**, 306 (1995).

[48] C. Weldon, 'nanofit', Private communcation.

[49] T. Yamazaki, Nuclear Data Sheets. Section A **3**, 1 (1967).

[50] A. Krämer-Flecken *et al.*, Nuclear Instruments and Methods in Physics Research Section A: Accelerators, Spectrometers, Detectors and Associated Equipment **275**, 333 (1989).

[51] C. Bargholtz and P. E. Tegnér, Nuclear Instruments and Methods in Physics Research Section A: Accelerators, Spectrometers, Detectors and Associated Equipment **256**, 513 (1987).

[52] K. S. Krane, *Introductory Nuclear Physics*, 2nd ed. (John Wiley and Sons Inc., ADDRESS, 1987).

[53] P. H. Regan *et al.*, Physical Review C **51**, (1995).

[54] C. Wheldon *et al.*, Nuclear Physics A **699**, 415 (2002).

[55] P. M. Walker *et al.*, Nuclear Physics A **568**, 397 (1994).

[56] G. D. Dracoulis, C. Fahlander, and M. P. Fewell, Nuclear Physics A **383**, 119 (1982).

[57] G. D. Dracoulis *et al.*, Nuclear Physics A **509**, 605 (1990).

[58] A. Neskakis *et al.*, Zeitschrift fur Physik A **304**, 277 (1982).

[59] T. Kibédi, G. D. Dracoulis, A. P. Byrne, and P. M. Davidson, Nuclear Physics A **567**, 183 (1994).

[60] A. Neskakis, R. M. Lieder, G. Sletten, and J. D. Garrett, Physics Letters B **118**, 49 (1982).

[61] G. Dracoulis, C. Fahlander, and M. P. Fewell, Physical Review Letters **45**, (1980).

[62] R. Lieder, A. Neskaski, and J. skalski, Nuclear Physics A **476**, 545 (1988).

[63] R. Lieder *et al.*, Nuclear Physics A **645**, 45 (1999).

[64] T. Venkova *et al.*, Zeitschrift fur Physik A (1993).

[65] O. Möller *et al.*, Physical Review C **72**, (2005).

[66] J. Pedersen *et al.*, High-spin isomers in W and Os nuclei; Competition betweenK-quantization and triaxiality, 1985.

[67] J. F. Smith, private communcation.

[68] L. L. Riedinger *et al.*, Physical Review Letters **44**, (1980).

[69] P. Walker, BCS calculations, Private communcation.

[70] P. Moller, J. R. Nix, W. D. Myers, and W. J. Swiatecki, Atomic Data and Nuclear Data Tables **59**, 185 (1995).

[71] T. Kutsarova *et al.*, Nuclear Physics A **587**, 111 (1995).

[72] T. Venkova *et al.*, Zeitschrift fur Physik A Hadrons and Nuclei **334**, 385 (1989).

[73] G. D. Dracoulis *et al.*, Nuclear Physics A **554**, 439 (1993).

[74] D. M. Cullen *et al.*, Nuclear Physics A **728**, 287 (2003).

[75] D. L. Balabanski *et al.*, Nuclear Physics A **563**, 129 (1993).

[76] R. M. Lieder, G. Sletten, J. Borggreen, and J. Pedersen, Nuclear Physics, Section A **375**, 291 (1982).

[77] T. Kutsarova *et al.*, Nuclear Physics A **587**, 111 (1995).

[78] P. Vogel, Physics Letters B **60**, 431 (1976), cited By (since 1996) 22.

[79] C. S. Purry *et al.*, Nuclear Physics A **632**, 229 (1998).

[80] K. E. G. Lobner, *The electromagnetic interaction in nuclear spectroscopy.* (Hamilton, W.D., ADDRESS, 1975).

[81] P. Chowdhury *et al.*, Nuclear Physics A **485**, 136 (1988).

[82] F. R. Xu, P. M. Walker, J. A. Sheikh, and R. Wyss, Physics Letters B **435**, 257 (1998).

[83] D. M. C. et al, Journal of Physics G: Nuclear and Particle Physics **31**, (2005).

[84] W. Reviol *et al.*, Physical Review C (Nuclear Physics) **74**, 044305 (2006).